

Spring 3-23-2017

A Study of Iron-Nitrogen-Carbon Fuel Cell Catalysts: Chemistry – Nanostructure – Performance

Michael J. Workman
University of New Mexico

Follow this and additional works at: https://digitalrepository.unm.edu/nsms_etds

 Part of the [Catalysis and Reaction Engineering Commons](#), [Materials Science and Engineering Commons](#), and the [Nanoscience and Nanotechnology Commons](#)

Recommended Citation

Workman, Michael J.. "A Study of Iron-Nitrogen-Carbon Fuel Cell Catalysts: Chemistry – Nanostructure – Performance." (2017).
https://digitalrepository.unm.edu/nsms_etds/36

This Dissertation is brought to you for free and open access by the Engineering ETDs at UNM Digital Repository. It has been accepted for inclusion in Nanoscience and Microsystems ETDs by an authorized administrator of UNM Digital Repository. For more information, please contact disc@unm.edu.

Michael J. Workman Jr.

Candidate

Nanoscience and Microsystems

Department

This dissertation is approved, and it is acceptable in quality and form for publication:

Approved by the Dissertation Committee:

Dr. Plamen Atanassov, Chairperson

Dr. Kateryna Artyushkova

Dr. Fernando Garzon

Dr. Scott Calabrese-Barton

Dr. Iryna Zenyuk

**A STUDY OF IRON-NITROGEN-CARBON
FUEL CELL CATALYSTS:
CHEMISTRY – NANOSTRUCTURE – PERFORMANCE**

by

MICHAEL J. WORKMAN JR.

B.S., Chemistry,
Southern Oregon University, 2012
B.S., Physics,
Southern Oregon University, 2012
M.S., Nanoscience and Microsystems Engineering,
University of New Mexico, 2014
Ph.D., Nanoscience and Microsystems Engineering,
University of New Mexico, 2017

DISSERTATION

Submitted in Partial Fulfillment of the
Requirements for the Degree of
Doctor of Philosophy
Nanoscience and Microsystems Engineering

The University of New Mexico
Albuquerque, New Mexico

May, 2017

© Copyright 2017 by Michael J. Workman Jr.

Dedication

For those who never found their way out of the darkness, who sank so far they could not find the light.

When belief is impossible, hope and willingness will suffice until you can see the light for yourself.

It's never too late to come looking.

The light is still here.

Acknowledgements

I would like to sincerely thank my advisors, Plamen Atanassov and Kateryna Artyushkova. From the day I expressed interest in working with you, you have both been straight-forward, honest, and supportive of me on both a professional and personal level. Your guidance and clarity in helping me understand the big-picture and minute details have been invaluable. I would also like to thank Alexey Serov for his direction in synthesis and testing. Without your materials, my work would be far less meaningful.

I would like to thank my collaborators including: Pajarito Powder, LLC, particularly Barr Halevi, who has allowed the use of their facilities, and Sam McKinney for his hands-on work testing my materials; Svitlana Pylypenko and her research group, including Michael Dzara and Chilan Ngo, for excellent TEM analysis and insights; and Scott Calabrese-Barton, and his group members Nate Leonard and Alex Mirabal, for indispensable materials analysis and modeling insights.

I am grateful to my dissertation committee: Drs. Plamen Atanassov, Kateryna Artyushkova, Fernando Garzon, Scott Calabrese-Barton, and Iryna Zenyuk for their time and effort in evaluating and providing feedback on this work.

My research has been funded by the NSF Graduate Research Fellowship Program #1418062, the DOE-EERE Fuel Cell Technology Program "Development of Novel Non Pt Group Metal Electrocatalysts for PEMFC," and the UNM Center for Micro-Engineered Materials.

There are several people who have personally made the completion (and beginning) of my Ph.D. possible. Among them, I would like to thank my father, who stressed the importance of rational thought and examination of all things, laying the foundation for my interest in science; and my mother, who continues to encourage me to pursue that which makes me happy, making it possible for me to take the risk to go back to school. Dana was there when things were at their darkest for me. I wouldn't be here at all without your help and support. My daughters, Betty and Karen, have been understanding and patient as I've been a student for more than half of their lives. Brooke has been a tremendously valuable source of support and encouragement (and editing) as I worked through the last years of grad school. And finally, none of this would have been possible without my friends, who have taught me that if I 'suit-up and show-up,' and attempt to do the 'next right thing,' then great things will come to pass.

A Study of Iron-Nitrogen-Carbon Fuel Cell Catalysts: Chemistry – Nanostructure – Performance

by

Michael J. Workman Jr.

B.S., Chemistry,

Southern Oregon University, 2012

B.S., Physics,

Southern Oregon University, 2012

M.S., Nanoscience and Microsystems Engineering,

University of New Mexico, 2014

Ph.D., Nanoscience and Microsystems Engineering,

University of New Mexico, 2017

Abstract

Fuel cells have the potential to be a pollution-free, low-cost, and energy efficient alternative to the internal combustion engine for transportation and small-scale stationary power applications. The current state of fuel cell technology has already achieved two of these three lofty goals. The remaining barrier to wide-scale deployment is the high cost, which is primarily caused by dependence on large amounts of platinum to catalyze the energy conversion reactions. To overcome this barrier and facilitate the integration of fuel cells into mainstream applications, research into a new class of catalyst materials that do not require platinum is needed.

There has been a significant amount of research effort directed toward the development of platinum-group metal free (PGM-free) catalysts, yet there is a lack of consensus on both the engineering parameters necessary to improve the technology and the fundamental science that would facilitate rational design. I have engaged in research on PGM-free catalysts based on inexpensive and abundant reagents, specifically: nicarbazin and iron. Catalysts made from these precursors have previously proven to be among the best PGM-free catalysts, but their continued advancement suffered from the same lack of understanding that besets all catalysts in this class. The work I have performed address both engineering concerns and fundamental underlying principles. I present results demonstrating correlations between physical structure, chemical speciation, and synthesis parameters, as well as addressing active site chemistry and likely locations.

My research presented herein introduces new morphology analysis techniques and elucidates several key structure-to-property characteristics of catalysts derived from iron and nicarbazin. I discuss the development and application of a new length-scale specific surface analysis technique that allows for analysis of well-defined size ranges from a few nm to several microns. The existing technique of focused ion beam tomography is modified and optimized for platinum-group metal free catalyst layers, facilitating direct observation of catalyst integration into catalyst layers. I present evidence supporting the hypothesis that atomically dispersed iron coordinated with nitrogen are the dominant active sites in these catalysts. Further, that the concentration of surface oxides in the carbon structure, which can be directly

influenced by synthesis parameters, correlates with both the concentration of active sites in the material and with fuel cell performance. Catalyst performance is hindered by the addition of carbon nanotubes and by the presence of metallic iron. Evidence consistent with the catalytic active sites residing in the graphitic plane is also presented.

Table of Contents

Dedication	iii
Acknowledgements	iv
Abstract	vi
List of abbreviations used in this text	xi
Chapter 1 – Introduction.....	1
1.1 – Motivation.....	1
1.2 – Introduction to fuel cells	2
1.3 – Need for research	5
Chapter 2 – Background and Previous Work	7
2.1 – Performance analysis.....	7
2.2 – Morphology analysis	11
2.3 – Chemical analysis	16
Chapter 3 – Research Objectives.....	21
3.1 – Discussion of research need	21
3.2 – Research goals	25
Chapter 4 –DWT Analysis Theory and Application	30
4.1 – Abstract	30
4.2 – Introduction	31
4.3 – Materials and Methods	36
4.4 – Results and Discussion.....	40
4.5 – Conclusion	54
4.6 – Acknowledgements	56
Chapter 5 – FIB/SEM Tomography Method.....	57
5.1 – Introduction	57
5.2 – Background.....	57
5.3 – Materials	59
5.4 – Experimental method	59
Chapter 6 – Synthesis to Chemistry and Performance Relationships.....	65
6.1 – Abstract	65
6.1 – Introduction/Background.....	66
6.2 – Experimental	70
6.3 – Results	74
6.4 – Analysis and Discussion	83
6.5 – Conclusion	87
6.6 – Acknowledgements	88

Chapter 7 – Morphology, Chemistry, and Performance.....	89
7.1 – Introduction	89
7.2 – Experimental	89
7.3 – Results and discussion	92
7.4 – Conclusion	111
Chapter 8 – Application of Structure to Property Predictions	112
8.1 – Introduction	112
8.2 – Experimental	112
8.3 – Results and discussion	113
8.4 – Conclusion	121
Chapter 9 – Conclusion and Significance	122
10 – Publications in Peer-Reviewed Journals	125
11 – Presentations Published as Abstracts.....	126
Appendix A – SI for DWT Manuscript.....	128
Appendix B – FIB tomography procedure.....	134
References	136

List of abbreviations used in this text

AFM	Atomic force microscopy
A.U.	Arbitrary units
BET	Brunauer–Emmett–Teller
BJH	Barrett–Joyner–Halenda
CNT	Carbon nanotube
CV	Cyclic voltammogram
DFT	Density functional theory
DIP	Digital image processing
DWT	Discrete wavelet transform
EDS	Energy dispersive spectroscopy
EXAFS	Extended x-ray absorption fine structure
Fe-NCB	Iron-nicarbazin derived catalyst
FIB	Focused ion beam
GDE	Gas diffusion electrode
GDL	Gas diffusion layer
HAADF	High-angle annular dark field
HT	Heat treatment (pyrolysis)
MEA	Membrane electrode assembly
MNC	Metal-nitrogen-carbon catalyst
Nano-CT	Nanoscale computerized x-ray tomography
non-PGM	Non-platinum group metal
OCV	Open circuit voltage
ORR	Oxygen reduction reaction
PEM	Proton exchange membrane
PGM-free	Platinum group metal free
PSD	Pore size distribution
RDE	Rotating disk electrode
RMS	Root mean square
R_q	RMS roughness
RRDE	Rotating ring disk electrode
R_{sk}	Skewness
SEM	Scanning electron microscopy
SSM	Sacrificial support method
STEM	Scanning transmission electron microscopy
TEM	Transmission electron microscopy
XANES	X-ray absorption near edge structure
XAS	X-ray absorption spectroscopy
XPS	X-ray photoelectron spectroscopy
XRD	X-ray diffraction

Chapter 1 – Introduction

1.1 – Motivation

The need for research into new energy sources and storage technologies is driven by environmental, political, and economic concerns. In the U.S., and worldwide, the energy landscape is dominated by fossil fuels.¹ The use of fossil fuels has several drawbacks that make the search for alternative energy solutions critical. Geopolitical tensions are created or exacerbated by the increasing need for petroleum. The environmental impact caused by burning of fossil fuels is clearly evident and, in spite of current efforts, damage is still being caused at an accelerating rate.^{2, 3} Further, as our need for new fossil fuel sources increases, the environmental impact of their extraction is becoming a more apparent threat.^{4, 5} Addressing these issues requires development of energy technologies that facilitate either extraction of additional useful work from fossil fuels through increased efficiency, or energy sources that function entirely without fossil fuels.

The major components of energy use are industrial, transportation, and residential needs.⁶ Herein, I focus on small to medium scale energy technologies that primarily encompass transportation, with some overlap with residential and small industry. The vast majority of our transportation is powered by fossil fuels.⁶ Similarly, the primary source of emergency power generation for critical industrial applications (hospitals, data centers, government operations, etc.) are fossil fuel driven generators. Alternatives to fossil fuels for transportation include combustion of non-petroleum products, such as hydrogen, and electric vehicles. In electric

vehicles, the two primary technologies for energy storage in the vehicle are batteries, which store energy generated at a central power station supplied through the grid, and fuel cells, which carry energy in the form of fuel and convert the chemical energy directly to electrical power directly onboard the vehicle. Batteries are a highly efficient energy storage mechanism. They produce no emissions and their charge/discharge cycle has a high energy efficiency. However, batteries are expensive, recharging times are on the order of hours, and they have relatively low energy densities thereby limiting their range. Fuel cells are also expensive, but refueling times are on the order of minutes (similar to refueling a gasoline vehicle), and they have a much higher energy density than batteries allowing greater range on a single refueling. Though batteries currently cost less than fuel cell technology, and battery costs will continue to decrease with ongoing research, batteries are not projected to approach fuel cells in the areas of recharging/refueling times or energy densities. These concerns make fuel cells an attractive option as a final solution for transportation power sources.⁷⁻⁹ The rest of this text focuses on fuel cells and how these challenges may be overcome.

1.2 – Introduction to fuel cells

A fuel cell is similar to a battery in many ways. They both convert chemical energy directly to electrical energy without the need for a mechanical intermediate. The fundamental difference is that a battery is a closed system while a fuel cell is an open system. Batteries carry substances that are reversibly changeable from fuel when charged, to products when

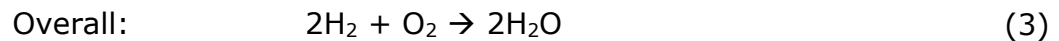
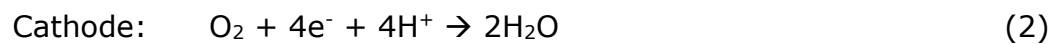
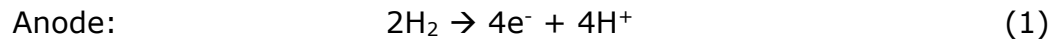
discharged. When the fuel is exhausted the products can be converted back into fuel by charging with an external electrical power source. In the case of a disposable battery, once the fuel is used up, the battery must be recycled to recover the materials for future use. In either case, fuel cannot be added and products do not leave the battery. Adding energy requires recharging, which is a slow process. A fuel cell is fed fuel from an outside reservoir, converts the fuel to electrical power, and discharges products. Fuel cells can operate continuously as long as there is fuel available, so their run time is limited by the amount of fuel able to be carried in the external tank. Adding energy is accomplished by refilling the fuel tank, which is a faster process.

There are multiple types of fuel cells that consume different fuels and operate at different temperatures, each with their own advantages and disadvantages. High temperature fuel cells operate between 200-1000 °C. They are generally the most efficient and are suited for continuous operation. Long startup times and the fact that they operate at high temperatures make this class of fuel cell unsuitable for use in transportation applications. Low temperature fuel cells operate under 100 °C and have short startup times. They include proton exchange membrane (PEM) fuel cells, anion exchange fuel cells, and direct methanol fuel cells. Methanol fuel cells are attractive because they use liquid fuel for which distribution infrastructure exists. However, as methanol is a hydrocarbon, they release CO₂ as a product. Anion exchange and PEM fuel cells use hydrogen as a fuel and exhaust only water. Anion exchange fuel cells perform extremely well at the cathode but have slow reactions at the anode. Further, they are a newer technology and

the ion conducting materials are not well developed. PEM fuel cells perform extremely well at the anode but have slow reactions at the cathode.

Research into ionomers for proton conduction have been under development for several decades and are well understood and inexpensive.

Figure 1-1 shows a diagram of a fuel cell and Equations 1-3 show the reactions that take place inside a PEM fuel cell.¹⁰



At the anode H_2 is oxidized to form protons and electrons. The protons travel through the ionomer in the catalyst layer and membrane to the cathode. The electrons cannot pass through the ionomer. They are conducted through an

external circuit where they produce usable electric power. At the cathode, the protons and electrons come together with O_2 to form water. The reactions at both the anode and cathode require catalysts to progress. The better the catalyst, the faster the reactions, and the more power the

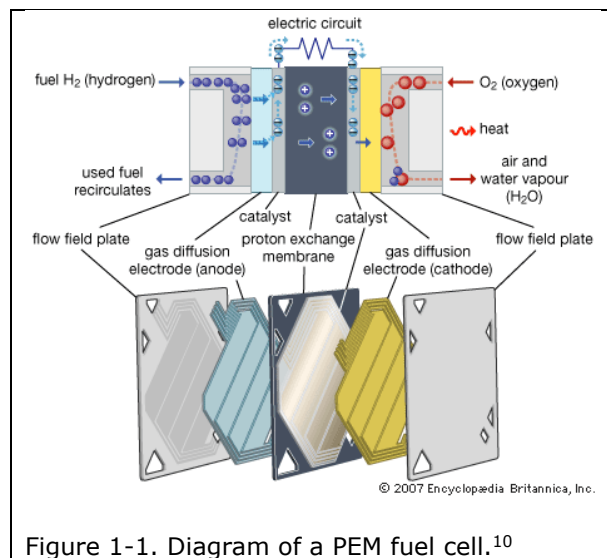


Figure 1-1. Diagram of a PEM fuel cell.¹⁰

fuel cell can generate.

1.3 – Need for research

Fuel cells are an attractive power source for transportation and small stationary applications. It is currently possible to construct fuel cells that provide the necessary power and longevity to replace the internal combustion engine in transportation applications. The reason this is not currently done is that fuel cells require large amounts of Pt to function. There are two issues with the use of high levels of Pt that make current fuel cell technology undeployable on a large scale. The cost of Pt is high and has been unstable. At current prices, about 40% of the total cost of a mass produced fuel cell would be due to Pt, making them too expensive to compete with existing technologies.¹¹ There is also a geopolitical issue in that approximately 80% of the known Pt deposits exist in one geographic region – South Africa.¹² Heavy international reliance on a natural resource that exists in one location has historically been problematic and is desirable to avoid.

To address these issues with fuel cells, there are two paths forward. One is ultra-low Pt loading fuel cells. These fuel cells would use a fraction of the Pt that current fuel cell technologies use. There is considerable research in this direction and, though progress has been made, the best Pt fuel cells are either far away from the desired loading, or far away from the desired performance.^{7, 8} The other path is development of a new class of catalyst that does not rely on precious metals to function. Such a class of catalysts was initially discovered in 1964 in phthalocyanines and has since been developed into engineered catalysts of a carbon-nitrogen matrix with embedded transition metals.^{7, 9, 13-16} This new class of catalysts is referred to by several

names: metal-nitrogen-carbon (MNC), non-precious metal, non-platinum group metal (non-PGM), or platinum-group metal free (PGM-free) catalysts.

In the last few years, there have been several reviews on the state of PGM-free catalysts. Reviews from the last five years alone have surveyed nearly 1000 publications on the subject.^{9, 13, 14, 16-21} The conclusions from these reviews can be summed up in short order.

- While considerable progress has been made in performance of PGM-free catalysts, they are still not competitive with catalysts based on precious metals such as Pt.
- Though much research has been devoted to understanding the fundamental structure of the active site(s) in these catalysts, there is no consensus.
- Though there are multiple variations on synthetic routes and precursors used for these catalysts, at their core, the vast majority of the syntheses are quite similar. Carbon and nitrogen precursors are pyrolyzed, usually in the presence of a transition metal such as iron or cobalt, to form carbon-nitrogen heterostructures with incorporated transition metals.

In the following section I review the literature that defines the state-of-the-art for PGM-free catalysts and illustrates these issues in detail.

Chapter 2 – Background and Previous Work

There has been a significant amount of effort directed toward the development of better PGM-free catalysts and understanding of their structure and fundamental properties.^{7-9, 13, 16-24} At present, the research mechanism has largely been a trial-and-error search for synthesis methods that produce better catalysts followed by multiple characterization methods to try and understand the new material. Though these characterizations have yielded some consistent information, the results are often ambiguous or not easily reconciled with each other. In this section, I will address the results of some of these analyses and give a brief description of techniques. The three primary foci are catalyst performance, material morphology, and chemical structure (including potential active site chemistries).

2.1 – Performance analysis

Primary measures of catalyst performance are catalytic performance, generally measured by rotating disk electrode (RDE) or rotating ring disk electrode (RRDE), and fuel cell performance as measured in a membrane electrode assembly (MEA). RDE analysis is a quick screen method that can be easily used to assess the activity of many catalysts in a shorter period of time, but it is not always a good indicator of fuel cell performance. RRDE adds the ability to measure H_2O_2 generation, which gives insight into the reaction pathway. Further, H_2O_2 quickly degrades fuel cell components, so it is an important product to monitor. It is possible to have a catalyst with excellent performance in RDE testing that exhibits very poor performance in

an actual fuel cell. However, since RDE measures catalytic activity, it is not the case that a material with very poor RDE performance could have good fuel cell performance.

In RDE analysis, a catalyst is coated onto a glassy carbon electrode, immersed in electrolyte with reactants, and rotated to force the electrolyte across the catalyst surface.²⁶ This rotation ensures that there is fresh electrolyte with reactants at the electrode surface, thereby eliminating bulk diffusion limitations for the reaction. A diagram of an RRDE is shown in

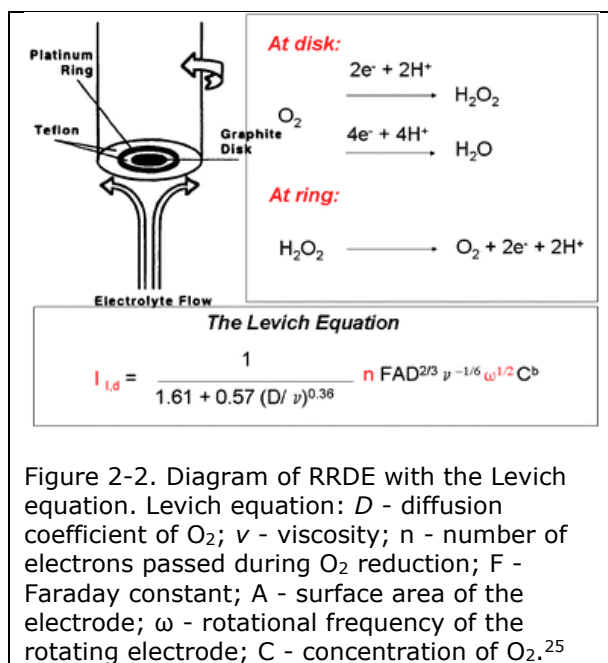
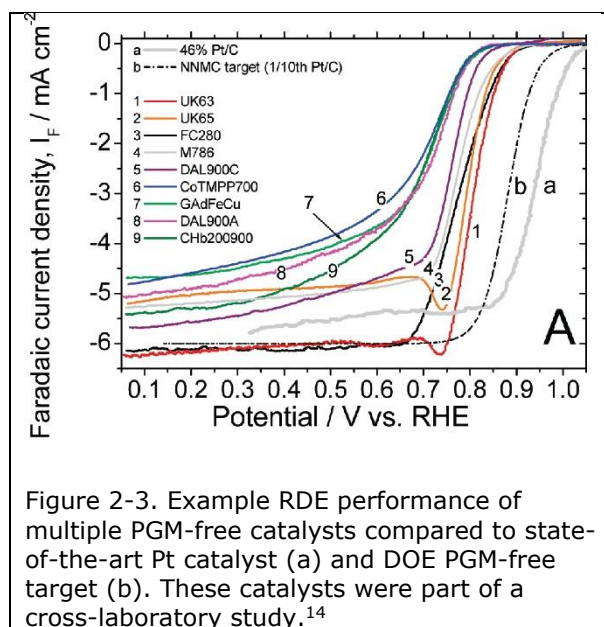


Figure 2-2 with the Levich equation which predicts the current generated at the disk. As the electrode is rotated, the potential is varied and the current between the electrode and a counter electrode is measured.

This produces a cyclic voltammogram (CV) that gives varying information depending on the reactants present in the

electrolyte, speed at which the potential is varied, rotation speed, and potentials used. For oxygen reduction reaction (ORR) performance measurements, the electrolyte is saturated with oxygen that is reduced to water or hydrogen peroxide at the catalyst surface. The current generated by these reactions, and the potential at which they occur, are indicators of

catalyst performance. The diffusion term in the Levich equation represents the diffusivity of O_2 in electrolyte. This equation assumes a perfectly smooth surface. As PGM-free catalysts are typically deposited to a high catalyst loading to ensure good coverage, the assumption of a smooth surface is not accurate. Because there is no way to account for diffusion within the catalyst layer, and peroxide can be both created and consumed within the catalyst layer,

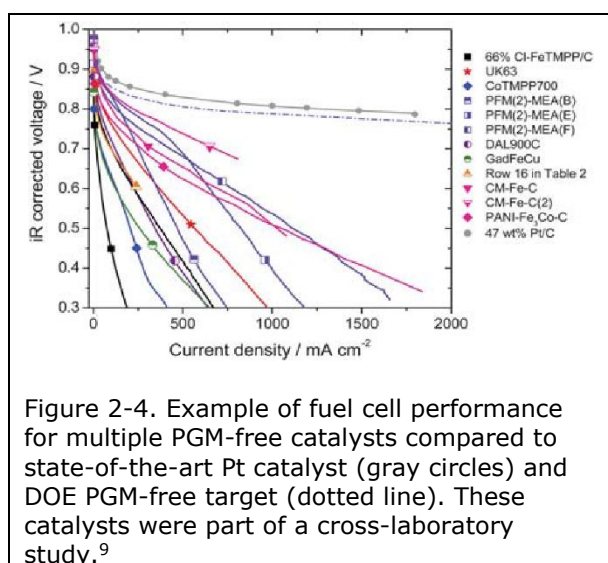


application of the Levich equation to PGM-free catalysts requires careful consideration as to its applicability.

The cathodic sweep of several catalysts is shown in Figure 2-3.¹⁴ The best performing catalyst on this plot is the Pt catalyst, found furthest to the right. It is the best performing because it begins generating current at the highest potential, the magnitude of the current increases very quickly as the potential drops, and it reaches its maximum current quickly. This performance curve is the goal everyone working on PGM-free catalysts is trying to approach. The PGM-free catalysts shown on this plot are state of the art catalysts from multiple laboratories. These RDE studies highlight the first hurdle PGM-free catalysts need to overcome: they are not nearly as active as Pt. While one strategy to compensate for a lack of activity is to use

more of the catalyst, this creates other performance issues when they are operated in a fuel cell.

The most representative measure of catalyst performance is by integrating it into a functioning fuel cell. As these catalysts are being developed for use in the cathode of fuel cells, the anode is typically constructed using Pt as the catalyst. A representative fuel cell performance



curve is shown in Figure 2-4.⁹ In these plots, a better catalyst has a higher current at low voltage (starts higher on the left side of the plot), and has the most horizontal possible tail yielding the highest current at low voltages. Each region of the performance curve is influenced by different

physical characteristics of the fuel cell. The low current region is greatly influenced by the chemical kinetics of the catalyst. It represents the catalytic activity without regard to mass or charge transport limitations in the fuel cell. The region of intermediate current, in this plot from about 200-600 mA cm⁻², is the ohmic region. This portion of performance is dominated by electronic resistance losses from both electron and proton transport limitations. The region of high current is dominated by mass transport limitations. PGM-free catalysts are at a disadvantage in all three regions. As noted above, PGM-free catalysts are not as active as Pt catalysts, so their kinetics are slower,

resulting in a lower starting potential. To compensate for this lower activity, PGM-free catalyst layers are much thicker than layers with Pt. This thickness causes additional performance losses in both the ohmic and transport regimes.

I have referenced the performance difference between Pt and PGM-free catalysts above, but have not yet quantified this difference. For current commercially available Pt/C catalysts, current at 0.8 V is about 1500 mA cm⁻², as seen in Figure 2-4. At the same voltage, PGM-free catalysts produce 50-300 mA cm⁻².¹⁴ Because PGM-free catalysts have less activity, they cannot be operated at the same voltage as a Pt based fuel cell. PGM-free catalyst performance is frequently measured at 0.5 or 0.6 V and still produce less than 1000 mA cm⁻².^{7, 9} It should be noted that these values were obtained using oxygen at the cathode where in real-world applications, they would be using air, which lowers the performance significantly more for PGM-free than it does for Pt.

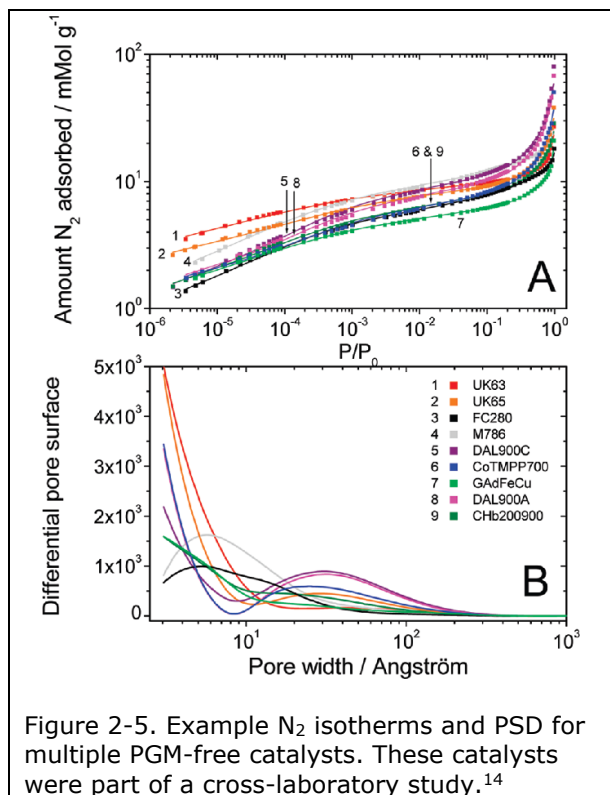
Mechanisms to improve performance of PGM-free catalysts are to increase the activity and improve transport characteristics. Improvement of transport characteristics requires understanding and control of catalyst morphology. Increasing catalyst activity requires either increasing the number of active sites, or improving the quality of the active sites.

2.2 – Morphology analysis

Measurement of catalyst morphology includes understanding of the internal and external physical structure of the individual catalyst particles as

well as how they interact with each other and the ionomer in a fuel cell catalyst layer. Existing methods to analyze the internal structure of catalysts are well developed. Analysis of nitrogen isotherms are commonly used to determine the total internal surface area and distribution of pore sizes within the material.^{7, 14, 27} Analysis of the total surface area is commonly performed using theory first presented in 1939 by Brunauer, Emmett, and Teller, commonly referred to as BET theory.²⁸ Pore size distributions (PSD) are estimated either by a classical theory developed by Barrett, Joyner, and Halenda, commonly called BJH, or by density functional theory (DFT) that was optimized for activated carbons by Ustinov.^{29, 30} The primary advantage of using BET is that surface areas can be quickly measured, generally in under an hour, and the instrument is simple to use. But BET does not give any information on the sizes of pores. Further, with standard degassing techniques used for BET, the micropores may not be completely emptied, so the measured surface area can miss area contained in micropores. BJH theory is well suited to measuring pore sizes greater than ~ 2 nm, and is based on the assumption that the surface area of a pore increases as the square of its diameter. This is a valid assumption with pores that are spherical or nearly any polyhedral shape, but is fundamentally inaccurate for pores that exist as the space between two planes. BJH also fails to properly address micropores because it does not take into account intermolecular forces that occur in the adsorptive as the size of the pore approaches the size of the adsorptive molecules.³¹ This technique is well suited for many classes of materials, and can be performed in about 24 hours, but is not well suited

to pore size analysis of high surface area carbons. DFT, while the best suited for accurate analysis of carbon based carbon materials, takes about three days to measure one sample. This increased analysis time results from the necessity to achieve extremely low pressures, about 10^{-6} P/P₀ (where P is the measurement pressure and P₀ saturation pressure of nitrogen). As developed



by Ustinov, DFT models micropores as slits between carbon sheets. It also takes into account the physical dimension of the nitrogen molecules, their intermolecular forces in a small pore, and their interactions with the opposite wall in very narrow pores. It yields the most accurate total surface area and pore sizes for PGM-free catalysts. This is especially important since

micropores compose a high percent of the total surface area of the most active catalysts, and there is evidence that the active sites are most abundant in micropores.^{7, 14, 27, 32} Figure 2-5 shows isotherms of several catalysts and the pore size distributions calculated using DFT.¹⁴ Figure 2-6 gives a comparison of catalyst RDE performance with micropore surface area. In the materials tested, there is a clear correlation between micropore total surface area and catalyst performance. Similar observations have been made

in other papers and correspond to results from ab initio quantum calculations.^{27, 32}

Analysis techniques for surface morphology are not as well developed as those for pore sizes. Imaging of catalyst surfaces is frequently done using scanning electron microscopy (SEM). However, the quantitative information contained in SEM images is largely underutilized.

The dominant approach to SEM

images is qualitative analysis by means of visual inspection.³³⁻³⁷ Digital

Image Processing (DIP) is used on SEM images to find objective

representations of the intensity distribution in an image to convert these 2-D

images into 1-D image descriptors (values) that can be utilized for

quantitative morphology representation and description.^{38, 39} However,

relevant length scales for different transport and packing phenomena occur

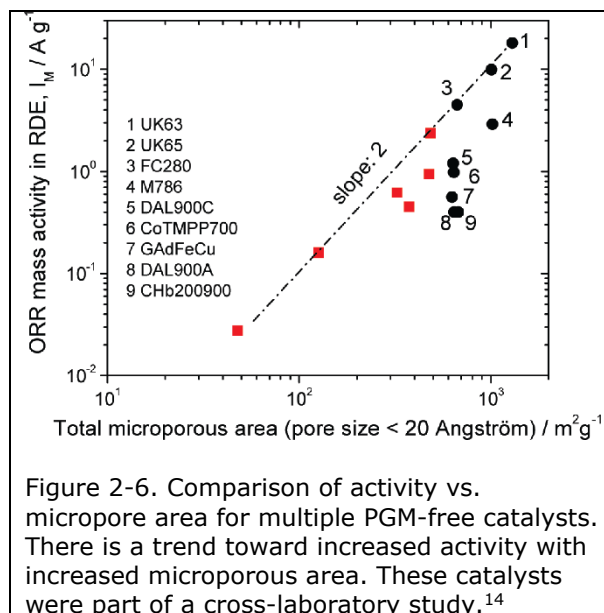
from a few to a few hundred nanometers. Useful analysis of catalyst surfaces

requires the ability to quantitatively distinguish surface features at different

length scales, much the same way that pore size distributions distinguish

between different size pores.

Traditionally, surface morphology has been separated into two length-scales called roughness for short scales and waviness for long scales.⁴⁰ There



is not a precise definition for what constitutes long and short scales within a surface or image. The use of Gaussian low-high-filtering for separating different scales of roughness is the conventional routine established for surface profilometry for all length-scales.⁴⁰ Prior work has successfully extended this methodology to SEM images, in which high-pass and low-pass filters were employed to separate images into roughness and waviness image components, respectively.^{38, 39, 41} This approach allows the separation of morphological information into two different scales for analysis. However, the high-low filtering approach only provides differentiation between ill-defined “large” and “small” features for a particular image scale. Further, correlation of these categories to specific physical sizes has been imprecise. Useful analysis of catalyst surfaces requires new techniques to accurately separate length-scales of surface features.

X-ray diffraction (XRD) is a technique frequently used for analysis of metal-rich catalysts, but the XRD features generated by carbon are either qualitatively addressed or overlooked as background around the metal pattern of interest. There exists a, now rarely used, curve fitting algorithm capable of extracting information on the carbon crystalline structure including crystallite size and number of graphitic layers.⁴² From both engineering and fundamental science perspectives, understanding the locations of active sites within the graphitic structure is of central importance. From an engineering standpoint, this knowledge would provide concrete materials engineering targets. From a fundamental science perspective, it provides much needed

modeling input allowing for calculation of potential active site structures and reaction pathways.

2.3 – Chemical analysis

There are many chemical characterization techniques that have the potential to be used on PGM-free catalysts, but the most common are x-ray absorption spectroscopy (XAS) and x-ray photoelectron spectroscopy (XPS). Less commonly used but frequently cited because it provides information otherwise unavailable is a gamma radiation technique called Mössbauer spectroscopy. Additionally, for this work I will use transmission electron microscope energy dispersive spectroscopy (TEM/EDS). Related to, but separate from these analysis techniques, are modeling techniques using *ab initio* quantum calculations (also called DFT, but distinct from analysis of pore sizes). These chemical simulations are not analyses of existing materials, but the models take into account data from chemical measurements and attempt to predict structures and reaction pathways.

The two x-ray analysis methods give complementary information. XAS is a bulk technique that particularly well suited to yield information on metal in the catalyst. Catalysts containing fractions of a percent of Fe are well within the detection capability of XAS. Also, since XAS is a transmissive technique, it is possible to analyze these catalysts *in operando*, allowing for examination of transitions in the Fe spectrum with changes in potential. There are two analysis techniques for XAS data. X-ray absorption near edge structure (XANES) gives information on the oxidation state and coordination

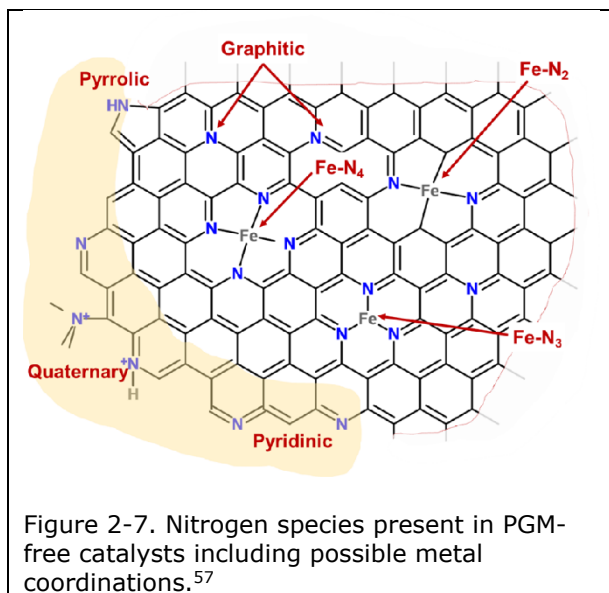
of Fe. Extended x-ray absorption fine structure (EXAFS) gives information on the nearest neighbors and bond distances for atoms in the vicinity of Fe atoms. The combination of these techniques allows for analysis of Fe in PGM-free catalysts and its immediate environment. The majority of XAS experiments indicate that the most active catalysts have Fe coordinated to N and little or no Fe coordinated with Fe.^{21, 43, 44} Though, there are publications that report good performance with little or no Fe-N coordination.⁴⁵

XPS is a surface analysis technique giving information on the top few nm of a sample. Many of the catalysts have iron concentrations of less than 1%. XPS with detection limits on the order of parts per thousand is not well suited to give detailed information on iron content. But XPS is particularly well suited to give detailed information on the concentration and chemical environment of carbon, oxygen, and nitrogen in these materials. From XPS analysis, it is seen that though the catalysts are typically 80-95% carbon, increases in specific nitrogen species correlates with better performance. It is observed that pyridinic nitrogen and nitrogen bound to iron are present in higher concentrations in catalysts with the best performance while pyrrolic nitrogen is more prevalent in catalysts with poor performance.^{11, 14, 20-22, 27, 44-55} Relevant N species are shown in Figure 2-7.

Fundamentally different from x-ray analyses that examine the electron shells of materials, Mössbauer spectroscopy probes the nucleus of the element of interest, in this case Fe. It gives information on the energy state of the nucleus which is affected by the coordination and bonding of Fe.⁵⁶ In Fe containing catalysts, data from Mössbauer spectroscopy is consistent with

observations from XAS. Catalysts with the greatest activity exhibit Fe coordinated with nitrogen.^{7, 14, 24, 43, 56}

TEM/EDS analysis uses x-rays emitted during TEM analysis to measure elemental composition at the sub-nanometer scale. The overlay of images of C, N, and Fe concentrations has the potential to yield important insight into the N and Fe distribution of samples to understand how position-dependent elemental distribution and length-scale specific heterogeneity affect catalyst performance.



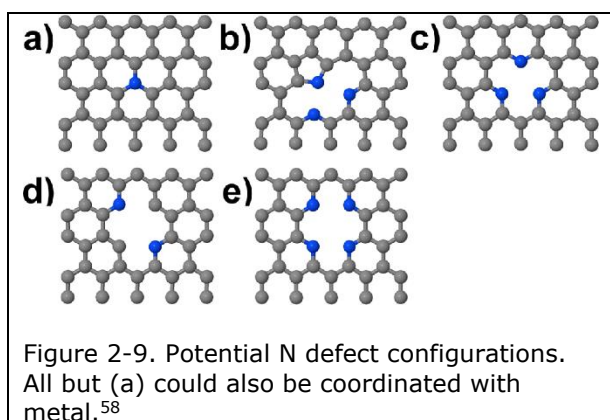
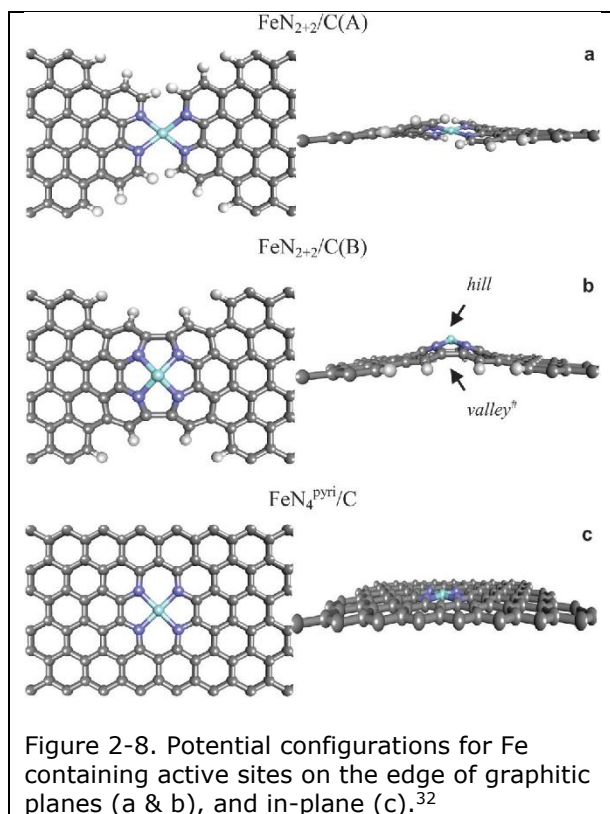
Combining results from all of these analyses methods gives insight into possible structures for the active site(s) responsible for the ORR in these catalysts. The primary schools of thought are that the metal is coordinated with nitrogen atoms incorporated in the carbon matrix, that the metal is not part of the active site but may help promote development of the N-C active sites, or that Fe-rich phases (metallic Fe, carbide, or oxide) modify graphitic structures in the vicinity making the graphite itself active. These insights allow modelers to calculate possible structures and examine their activity using *ab initio* calculations. These calculations indicate several possible structures, shown in Figures 2-8 & 2-9.^{32, 58} They are iron coordinated with 2, 3, or 4 nitrogen atoms Fe-N₂, Fe-N₃, and Fe-N₄, respectively. Another

configuration is an iron atom coordinated with nitrogen atoms on different graphitic sheets, Fe-N₂₊₂. Each of the potential active sites could also function without the iron atom, which would be the case in a metal-free catalyst.

While there are still papers being published claiming high activity from metal free catalysts, their viability has been addressed and, I believe, successfully

refuted.^{7, 59} There are truly metal-free catalysts that have been carefully synthesized with no metal anywhere in the synthesis procedure. All of these catalysts have had low activity and primarily generated peroxide as

opposed to completing the reaction to water. The majority of claimed metal-free catalysts, and all that have reported favorable activity, were prepared with metal containing precursors, then leached in an effort to remove all of the metal. These materials are then characterized with XPS which does not detect any iron (or other transition metal), so they are claimed to be metal



free. XPS has a detection limit of parts per thousand, while metals present at the ppm level have been shown to significantly improve catalyst performance. Further, it has been shown that no amount of leaching with acid can remove all metal from this type of material. As such, I believe that metal-free catalysts are not viable materials for the ORR in fuel cells and I will not include them in further discussion or analysis in this work.

The question then is which iron-containing active site(s) is responsible for the activity in well performing catalysts, and what structures are associated with their presence. Fundamental to this question is whether these active sites are present in the graphitic plane or at the edges of planes. Answering this question will provide insight into both the fundamental question of the actual structure of the active site, as well as the engineering concern of how to design materials that maximize the number of active sites present in a catalyst.

Chapter 3 – Research Objectives

3.1 – Discussion of research need

In the previous section, I addressed the research methods and results that comprise the state-of-the-art for PGM-free catalysts. Here I present a summary of the underlying challenges, highlighting the need for this research and how my work has advanced knowledge and capability in the field.

While considerable progress has been made in PGM-free catalyst performance, they are still not competitive with catalysts based on precious metals such as Pt. In the broadest sense, performance is defined as the ability of these catalysts to be incorporated into a fuel cell stack and supply a vehicle (or other application) with adequate power for a reasonable lifespan. As compared to Pt, PGM-free catalysts fall far short on both measures. These shortcomings can be traced to two known causes: activity and durability. The activity of a catalyst is a measure of how quickly it allows the desired reaction to progress. In this case, this is the oxygen reduction reaction. Pt is much more effective at catalyzing the ORR reaction than PGM-free catalysts. To compensate for this lack of activity, PGM-free catalyst layers in fuel cells are 10-20 times thicker than Pt based layers.⁷ This increased catalyst layer thickness causes transport limitations that further hinder the performance of the fuel cell. Durability is simply how long a catalyst layer maintains a minimum acceptable performance. Though both Pt and PGM-free catalysts suffer from performance loss over time, the performance drop-off is steeper for PGM-free catalysts. Since PGM-free catalysts are starting from a performance deficit, addressing the durability issue is doubly critical to make

them a viable alternative.^{7, 8} Attempts have been made to address both of these issues, but there has been an interesting trend. The most active PGM-free catalysts lose much of their activity in a matter of minutes or hours. Catalysts that exhibit stability over dozens or hundreds of hours have more modest initial performance than the catalysts with highly publicized initial performance.⁷ In fact, catalysts that have the highest initial performance degrade so quickly that their performance falls below that of more durable catalysts in only a few hours.

Activity can be measured on a per-mass or per-area basis. Regardless of the normalization being used, activity is simply the product of how quickly a single reaction site can catalyze a reaction (turn-over frequency) and the number of reaction sites (site density). These phenomena are well understood for Pt catalysts. For PGM-free catalysts, where the nature of the active site is still a matter of debate and no reliable method to measure active site density exists, this is a much more nebulous concept. In principle, the ways to increase activity are to increase the number of these elusive active sites, or to increase the activity of the active sites themselves. Adding to the complexity is the fact that there are likely multiple active sites participating in the ORR reaction, both singly and in concert.⁵⁷ Ultimately, the goal is to increase both the active site density and turnover rate, which requires understanding the chemistries and morphologies that promote the formation of the most efficient active sites, and the synthesis parameters that yield these structures and chemistries.

The durability question is also more complex for PGM-free catalysts than for Pt. Again, the degradation mechanisms in Pt catalysts are well understood but largely don't apply to PGM-free catalysts. Pt nanoparticles undergo particle detachment, agglomeration, and growth.^{7, 8} Since there are no similar catalyst particles in PGM-free catalysts, these concepts do not transfer. However, catalyst flooding and carbon corrosion are processes that degrade performance in both classes of catalysts. Carbon corrosion that occurs as an electrochemical process appears to have similar mechanisms in both catalysts and can be largely mitigated by preventing potential excursions above 1.2 volts.^{7, 18} Though care needs to be taken in catalyst design to not exacerbate the problem, this is more of a system engineering concern than a material science issue. The other common failure mechanism is flooding. Though it is the same basic issue in both Pt and PGM-free catalysts, addressing flooding has different challenges for these classes of materials. Since PGM-free catalyst layers are an order of magnitude thicker, flooding is inherently more likely as there is more volume in which water can become trapped and a longer distance for it to flow out. Further, the carbon supports that are used for Pt can be tuned to address their hydrophobic properties. This is not an easily accessible knob for PGM-free catalysts. The synthesis techniques for PGM-free catalysts necessarily include introduction of hydrophilic groups into the carbon structure. Even though there is no consensus on the exact structure of the active site(s), nearly every proposed active site structure is hydrophilic.^{7, 13, 14, 24, 52, 55-57, 59, 60} Add to this the facts that active sites may be present inside micropores and that hydrophilic

micropores are the easiest structures to fill with water, and the complexity of the PGM-free flooding issue increases.^{27, 29, 30, 32} Addressing this challenge requires understanding of the active site locations, control of the transport properties of the catalyst structure, and understanding of chemical species present to facilitate work on modulation of catalyst hydrophilicity and durability.

Though much research has been devoted to understanding the fundamental structure of the active site(s) in PGM-free catalysts, there is no consensus. There are two primary schools of thought on the nature of the active sites. One believes that transition metal coordinated with nitrogen in the carbon matrix is the primary active site for the ORR. The other believes that iron-rich phases such as metallic iron, iron oxides, or iron carbides, are either the active species, or that these phases modify the carbon structure in their vicinity such that the modified graphitic structure becomes active toward the ORR.^{45, 61} Within the group that believes that transition metal coordinated with nitrogen is the primary active site, there is no consensus on the specific structure of that site. Though these sites are generally believed to be part of the graphitic structure, the location of these sites, i.e. in the graphitic plane or at the graphitic edge, is unknown.^{27, 29, 30, 32, 45, 62} Knowledge of the location of the most active of these sites is necessary for both understanding of their structure and the rational design of catalysts with improved performance.

Though there are multiple variations on synthetic routes and precursors used for these catalysts, at their core, the vast majority of the

syntheses are quite similar. Carbon and nitrogen precursors are pyrolyzed, usually in the presence of a transition metal such as iron or cobalt, to form carbon-nitrogen heterostructures with incorporated transition metals. The precursors include macrocycles such as phthalocyanines and porphyrins, polymers such as polyaniline poly-ethyleneimine, small carbon molecules such as aminoantipyrine, and metal-organic frameworks.^{15, 47, 48, 51, 63}

Depending on the carbon precursor, a separate nitrogen-containing precursor may be added. In most cases, a metal salt is also added. With tuning of the pyrolysis procedure for each individual recipe, not only can active catalysts be made from all of these precursors, but the final chemistries are very similar. So, while the choice of precursors is an important factor in the final product, the processing is at least as influential as the starting material. Further, since the final products are very similar in chemical composition and structure at the nanoscale, detailed analysis of chemistry and morphology variations brought on by differing synthesis procedures on a single precursor yields insight into fundamental aspects of the final catalysts that apply to syntheses utilizing differing precursors.

3.2 – Research goals

My work has focused on correlations between performance, morphology, and synthesis parameters in PGM-free catalysts for the ORR in PEM fuel cells. All of the catalysts I have studied were synthesized using the sacrificial support method (SSM), and my focus has been on catalysts synthesized with iron salts and nicarbazin precursor (Fe-NCB). **My**

overarching goal was to understand: *the surface and internal morphologies across multiple length scales that promote improved fuel cell performance, the chemistries correlated with electrochemical performance, the active site type and location, and the synthesis parameters that affect these properties in Fe-NCB catalysts.* I have achieved these goals by:

- 1)** Development of new techniques for length-scale specific analysis of catalyst surface and electrode morphology.
 - a) The catalyst surface analysis is based on analysis of SEM and AFM micrographs using the discrete wavelet transform (DWT). This novel technique allows for separation of surface features into well-defined length scales so that the morphology responsible for different phenomena (bulk transport, Knudsen diffusion, active site promoting structures) can be objectively quantified.
 - b) The electrode analysis technique employs tomographic reconstruction from image stacks acquired on a dual-beam focused ion beam/scanning electron microscope (FIB/SEM) instrument. This technique has been modified from existing methodology for Pt catalyst layers and optimized for PGM-free catalyst layer analysis. This technique allows for direct observation of catalyst integration into the fuel cell electrode assembly.
- 2)** Synthesis of Fe-NCB catalysts with varied synthesis parameters, chemical analysis at the micro-, meso-, and macroscale, electrochemical characterization, and performance testing.

- a) Varied synthesis parameters include silica templating agents, carbon nanotubes (CNT) additives, etching procedures, and pyrolysis parameters.
 - b) Electrochemical characterization was performed by RDE, providing information on catalytic activity.
 - c) Performance testing carried out in an operational fuel cell providing information on activity, transport phenomena, and potential real-world performance.
 - d) Chemical analysis by XPS yielding information on the surface chemistry of these catalysts, giving insight into the moieties that promote catalytic activity. Correlations with morphology and performance data provide new understanding of relationships between structure, chemistry, and performance.
 - e) TEM/EDS analysis shows nanoscale distributions of composition and complements XPS data to give a more complete picture of catalyst chemistry and length-scale specific heterogeneity.
- 3) Morphological analysis of catalysts and correlation of performance to structure.**
- a) The DWT and FIB/SEM analyses have been applied to the catalyst set synthesized with varying parameters to characterize the length-scale specific surface morphology of these catalysts and evaluate how they integrate into fuel cell electrode layers.

- b) Pore size distribution analysis by nitrogen isotherm analysis using BJH and DFT provides insight on internal catalyst morphology at the nanoscale.
- c) Carbon crystalline structure by XRD gives information on the graphitic structures (size, stacking, and disorder) in the catalyst materials. This analysis has provided insight into potential locations of active sites within the graphitic framework.
- d) Correlation of the surface and internal morphologies with chemistry and performance to develop a thorough picture of catalyst structure – chemistry – performance relationships.

The following chapters present the details and results of my research. Chapter 4 addresses the first research goal, detailing development and application of the DWT for length-scale specific surface analysis. This work was published in *Langmuir* in 2015,⁶⁴ and supported the publication of another manuscript in 2017.⁶⁵ Chapter 5 addresses the first and third research goals. It presents the detailed method for application of FIB/SEM tomography to PGM-free catalyst layers. This has not been published as a stand-alone manuscript, but the results of these analyses have provided supporting work for two publications in 2016.^{66, 67} Chapter 6 details work for the second research goal, addressing catalyst synthesis, chemical analysis by XPS and TEM/EDS, and correlations between synthesis parameters, chemical moieties, and performance. This work has been published in the *Journal of Power Sources* in 2017.⁶⁸ Chapter 7 addresses the rest of the second and

third goals, extending the work in Chapter 6 to include morphology characterization with XRD, isotherm analysis, and application of the DWT to the Fe-NCB catalyst set. Utilizing the information gained from pursuing these research goals, I have synthesized new catalysts that show significantly improved performance. Chapter 8 discusses the rationale for the synthesis parameters, chemical characterization, and performance characteristics of these materials.

Chapter 4 –DWT Analysis Theory and Application

The following chapter is presented as it was originally published in *Langmuir* in 2015.⁶⁴ The SI is in Appendix A. I gratefully acknowledge the work of my co-authors: Alexey Serov, Barr Halevi, Plamen Atanassov, and Kateryna Artyushkova. My contribution to this work included: Acquisition and analysis of SEM images, acquisition and analysis of AFM images, development of SEM imaging parameters, application of DWT theory, catalyst synthesis, data processing, correlation analysis, and interpretation of results.

Workman, M. J.; Serov, A.; Halevi, B.; Atanassov, P.; Artyushkova, K.

“Application of the Discrete Wavelet Transform to SEM and AFM Micrographs for Quantitative Analysis of Complex Surfaces.” *Langmuir* 2015, 31, 4924-33.

4.1 – Abstract

The discrete wavelet transform (DWT) has found significant utility in process monitoring, filtering, and feature isolation of SEM, AFM, and optical images. Current use of the DWT for surface analysis assumes initial knowledge of the sizes of the features of interest in order to effectively isolate and analyze surface components. Current methods do not adequately address complex, heterogeneous surfaces in which features across multiple size ranges are of interest. Further, in situations where structure-to-property relationships are desired, the identification of features relevant for the function of the material is necessary.

In this work, the DWT is examined as a tool for quantitative, length-scale specific surface metrology without prior knowledge of relevant features or length-scales. A new method is explored for determination of the best wavelet basis to minimize variation in roughness and skewness measurements with respect to change in position and orientation of surface features. It is discovered that the size of the wavelet does not directly correlate with the size of features on the surface, and a method to measure the true length-scale specific roughness of the surface is presented. This method is applied to SEM and AFM images of non-precious metal catalysts, yielding new length-scale specific structure-to-property relationships for chemical speciation and fuel cell performance. The relationship between SEM and AFM length-scale specific roughness is also explored. Evidence is presented that roughness distributions of SEM images, as measured by the DWT, is representative of the true surface roughness distribution obtained from AFM.

4.2 – Introduction

Surface morphology is a critical factor affecting functional performance of many materials. In this study, the surfaces of non-platinum group metal (non-PGM) catalysts were examined. The length-scales of features in these materials is of particular importance for several reasons. Transport behavior of fluids within the catalyst layer, accessibility of reactants to the active sites, and conductivity are affected by the morphology of the catalyst and support.⁶⁹ Roughness affects the mass transport behavior of reactants and

products in the catalyst layer.⁷⁰ Penetration of gases and ions into the pores is closely related to feature size and feature shape distributions.^{8, 71} In addition to standard size-dependent transport limitations, flooding of the catalyst layer is an issue that is strongly dependent on both internal and surface morphology.^{8, 72} Further, non-PGM catalysts are not well understood at a fundamental level, so development of length-scale specific structure-to-property relationships will make targeted design of better catalysts possible. The interplay between chemistry and morphology, manifested as macroscopic surface area captured by BET and microscopic porosity, has been shown to be a critical factor for both activity and stability of non-PGM electrocatalysts.^{46, 47, 49, 73} The relevant length-scales for these phenomena are from a few to a few hundred nanometers.

4.2.1 – Digital image processing as an analytical tool

Scanning electron microscopy (SEM) is suitable to access the above-stated lateral dimensions and to provide sets of images representative of morphology for statistically relevant structure-to-property correlations.³⁸ Though SEM is used extensively for characterization of surfaces, including electrocatalysts, the quantitative information contained in SEM images is being largely underutilized; currently, qualitative analysis by means of visual inspection of images is the dominant approach.³³⁻³⁷ The goal of Digital Image Processing (DIP) is to find an *objective* representation of the intensity distribution in images and to convert these 2-D images into 1-D image descriptors (values) that can be utilized for quantitative morphology

representation and description.^{38, 39} Ultimately, these values should correlate to macroscopic properties of interest. Common descriptors used both in DIP and traditional profilometry are roughness and skewness.^{38, 40} The root mean square (RMS) roughness (R_q) is the RMS deviation of the surface from the mean surface height or, in the case of a digital micrograph, departure of the intensity from the mean grayscale value. Skewness (R_{sk}) is a measure of how strongly a profile is biased above or below the mean value. The formal definitions are given in Equations 1 and 2, where y_i is the deviation from the mean of the i^{th} point in the micrograph or profile measurement containing n points.

$$R_q = \sqrt{\frac{1}{n} \sum_{i=1}^n y_i^2} \quad , \quad R_{sk} = \frac{1}{nR_q^3} \sum_{i=1}^n y_i^3 \quad (1, 2)$$

A higher value of roughness indicates a surface with more deviation from the norm, which is an intuitive interpretation. A positive value of skewness indicates the tail on the right side of the histogram of height measurements is longer or fatter than the tail on the left. This represents a higher concentration of surface features above the average than below. Similarly, a negative skewness represents a larger concentration of valleys/pores in the surface.

Morphological data from surface measurements contain information on a wide range of scales, from the smallest detectable by the instrument used to the largest features that fit in the measurement field of view. A major challenge in surface analysis of complex structures lies in quantifying features at different length-scales to understand scale-dependent effects

such as transport, packing, and interaction of the surface with other materials. This difficulty is exacerbated when the size and shape of the features that contribute to these phenomena are not known in advance.

Traditionally, surface morphology has been separated into two length-scales called roughness for short scales and waviness for long scales.⁴⁰ There is not a precise definition for what constitutes long and short scales within a surface or image. The use of Gaussian low-high-filtering for separating different scales of roughness is the conventional routine established for surface profilometry for all length-scales.⁴⁰ Prior work has successfully extended this methodology to SEM images, in which high-pass and low-pass filters were employed to separate images into roughness and waviness image components, respectively.^{38, 39, 41} This approach allowed the separation of morphological information into two different scales for analysis. This technique has yielded insight into chemical and performance correlations with size-dependent morphology. However, the high-low filtering approach only allows for differentiation between ill-defined “large” and “small” features for a particular image scale. Further, correlation of these categories to specific physical sizes has been imprecise.

4.2.2 – Previous work with wavelets

Wavelet analysis is a mathematical technique similar to Fourier analysis. Unlike the Fourier transform, which is based on an infinite periodic structure, wavelets are discrete. Where Fourier analysis gives detailed information about the *spacing* of discrete features, wavelet analysis gives

information about the *size* of discrete features. Wavelets have been previously applied in various ways for surface analysis. In process monitoring, the discrete wavelet transform (DWT) is used to find discontinuities, edges, and manufacturing flaws in topographic and optical images.^{37, 74, 75} For these process monitoring applications, the wavelet coefficients or reconstructions are inspected for a good process vs. a bad process, and the approximation or detail level of interest is determined. The DWT has also been used on microscope images for surface analysis of a variety of features including thin films, micelles, and edge detection.^{36, 76, 77} In these cases, the DWT was used for filtering or analysis of a known feature of interest. All of this previous work assumes that the feature of interest is known *a priori*, and the DWT is used to isolate and analyze that feature. These prior works also determine the best wavelet basis for a particular image based on its ability to isolate the known feature.

In this work, the use of detail reconstructions of the DWT for surface analysis is empirically examined. Methods are developed to measure surface roughness quantitatively at well-defined lateral length scales without initial knowledge of the sizes of feature(s) of interest. A new method is explored to identify the best wavelet for analysis of a variety of images and feature sizes. These techniques allow for analysis of complex, heterogeneous surfaces to quantitatively measure their length-specific morphology. Employing these methods, the DWT is applied to SEM images in order to analyze surface morphology and extract statistical information for well-defined length scales without initial knowledge of the features of interest. This allows for length-

scale specific structure-to-property analysis of these materials. The relationship between length-scale specific roughness of SEM and AFM images is also explored.

4.3 – Materials and Methods

4.3.1 – Materials

SEM imaging was performed on two instruments. The primary SEM was the Hitachi S-5200 UHR FE-SEM at 2 kV in SE mode. It has a reported resolution of 0.5 nm at 30 kV and 1.8 nm at 1kV.⁷⁸ For the Pajarito Powder catalyst set, the SEM used was a Quanta 3D FEG at 2 kV in SE mode. It has a reported resolution of 1.2 nm at 30 kV and 2.9 nm at 1 kV.⁷⁹ AFM profilometry was done on two instruments: an Asylum MFP-3D-BIO AFM and a WITec alpha 300R with AFM attachment. Both instruments were operated in intermittent contact mode with a super-sharp Si tip with a nominal radius of 5 nm. Surface chemical speciation was analyzed using XPS. Spectra were acquired on a Kratos Axis Ultra X-ray photoelectron spectrometer using a monochromatic Al Ka source operating at 300 W, and data analysis and quantification were performed using CasaXPS software. Fuel cell performance was measured in 5 cm² gas diffusion electrode based membrane electrode assemblies, in H₂/air at 100% relative humidity. Catalyst inks were made of 45 wt% Nafion mixed with a catalyst. The MEA was constructed using a Sigract 25BC GDL, and pressed with 211 Nafion Membrane. Wavelet decompositions and analysis calculations were performed using Matlab with the Image Processing toolbox, Wavelet toolbox, Optimization toolbox, and

routines written in-house.¹ Size correlation imaging was performed using NIST Au nanoparticles certified to be 54.9 ± 0.4 nm as measured by SEM.⁸⁰ Catalysts analyzed are all of the Fe-N-C type or their metal-less analogues, synthesized using the Sacrificial Support Method (SSM) developed in our group.^{46, 47, 73}

4.3.2 – Theory and Method

One fundamental issue with statistical analysis of size-separated surface features is that, typically, features of larger lateral size have higher amplitudes and dominate the parameter. Unless synthesis techniques are used to intentionally create high aspect ratio structures, the vertical dimension of the feature will be of a similar scale to its lateral dimensions. This is the case with the catalysts and catalyst supports of pyrolyzed carbon. So, if the roughness of features ranging from 10 to 200 nm is analyzed, the roughness of features near 200 nm will dominate the output. If there are any phenomena that correlate with roughness smaller than 50 nm, they will be overlooked using this method. For functional characterization and analysis of structure-to-property relationships, it is of vital importance that the method of length-scale separation and analysis to be is able to discern as many multi-scalar topographical features over the surface as possible. It is also necessary that the true lateral sizes represented by the length-scale separation be known. The DWT is a powerful tool for the analysis of multi-

¹ Code available online: <http://goo.gl/iH4dRc>

scale features of surfaces due to its properties of good length-scale approximation.⁸¹

Excellent descriptions of the continuous and discrete wavelet transforms can be found in Reference 77 and the Matlab Wavelet Toolbox user guide.⁸² Here, a brief qualitative introduction to wavelets and their application to surface morphology is presented. A more detailed description of the mathematical structure of the discrete wavelet transform is available in the Supporting Information. The wavelets used in this study are the 54 orthogonal, compactly supported wavelets in the Matlab Toolbox, and this description is limited to this class of orthonormal wavelet basis sets. The complete formalism of this and other classes of wavelets is thoroughly addressed in Reference 81.

Wavelet analysis divides the overall signal into different wavelength components and represents each component at a resolution that matches this scale. Similar to how a Fourier transform represents a signal as a sum of frequencies (commonly thought of as time to frequency conversion), a wavelet transform represents a signal as a sum of spatial wavelength sub-bands (time to scale conversion).⁸¹ When the wavelet transform is applied to topographic data, two new sets of data are created – a smoother version of original data called the first level *approximation* (A_1) and a data set that represents the residual between the original and the smoother data called the first level *details* (D_1). The wavelet transform is then applied to A_1 , and two new data sets are created, A_2 and D_2 . This process is repeated as many times as desired. The first two levels of decomposition are shown in

Figure 4-1. This process creates multiple detail levels, each representing a different length-scale. The sum of all smaller detail levels with an approximation returns the original signal without loss.

Each row and column in an image can be subjected to this decomposition. Then each of the details can then be reconstructed to give an image of features at that size scale. An example of an 8 level reconstruction is shown in Figure S1. The individual detail images can then be analyzed to characterize texture on the corresponding length-scales.⁸³ In this work, detail reconstructions were used instead of the wavelet coefficients. This allows for the calculation of skewness of the surface at various length-scales by summing detail reconstructions at multiple levels.

Skewness is zero for an individual detail reconstruction. It is also worth noting that the reconstructed images used were averages of the horizontal and vertical 1-D reconstructions and not

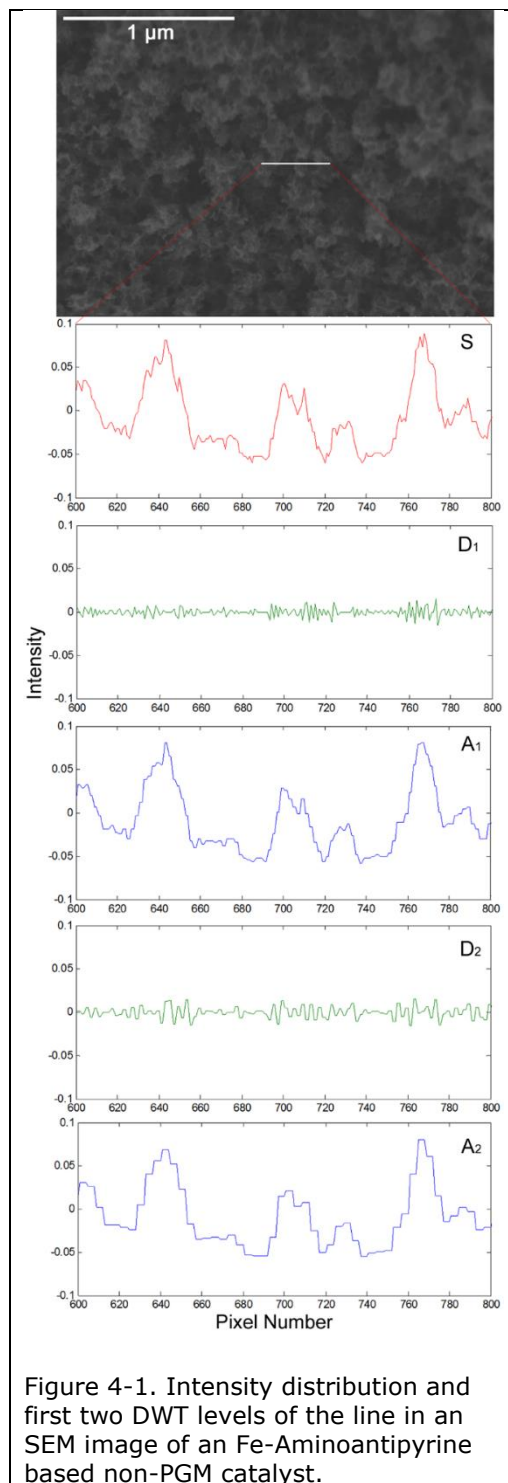


Figure 4-1. Intensity distribution and first two DWT levels of the line in an SEM image of an Fe-Aminoantipyrine based non-PGM catalyst.

from the 2-D reconstruction. These 1-D decompositions allowed for direct calculation of the wavelet size at each detail level for comparison to the physical features they were modeling. Because the materials being measured have no preferential orientation, averaging of 1-D decompositions is representative of the surface. As such, this technique applies best to surfaces with isotropic features or a large number of randomly oriented features.

4.3.3 – Analysis method

Prior to analysis, the mean intensity value was subtracted from each image. Then, the ten level DWT was performed using the Haar wavelet (choice of wavelet discussed below). All statistical image calculations were performed on images and detail reconstructions with a mean value of zero. Image reconstructions presented for viewing have had the original image mean intensity added back in after all processing. The SEM images used have an intensity range of 0 for black to 1 for white, so roughness values are based on this scale. For AFM images, calculations were done using values in nm, which were then converted to grayscale images.

4.4 – Results and Discussion

The first consideration in performing wavelet analysis is the choice of wavelet shape. There are 54 wavelet shapes defined in the Matlab wavelet toolbox (4 are identical, so 51 unique bases), and it is possible to design custom shape wavelets. For this study, the 54 existing wavelets in Matlab were examined. The most common method for selection of a wavelet shape

is to measure the entropy of wavelets when applied to the signal to be analyzed. Using this method, the entropy of each basis set is measured at each approximation and detail level. This technique is effective for determining the best wavelet basis set to analyze a single feature type or a single size of interest. However, to analyze the roughness of each detail level of the image, or where there are multiple size-ranges of interest, entropy of the wavelets does not provide a useful metric. For disordered systems with multiple length-scales to be analyzed, a different method of basis selection must be employed. For quantitative analysis of detail reconstructions, the goal is that samples with similar length-scale specific roughness and skewness yield similar values for roughness skewness at each detail level, independent of feature position or orientation.

Here, a different method was developed to determine the best wavelet for analysis of detail reconstructions of these images. Four images, shown in Figure S2, were each analyzed 100 times with different sections cropped off. This was accomplished by cropping 99 columns off of the original 1280 column images such that, for n being the sub-image number from 1 to 100, $n-1$ columns were cropped from the left side of the original image and $100-n$ columns were cropped from the right side of the original image. The variance of the roughness and skewness at each detail level for each sub-image across the 100 decompositions was measured. The wavelet with the minimum variance was found to be the Haar wavelet. Another advantage of the Haar wavelet is its simple shape and well defined size. This allows for direct calculation of how many pixels each detail level should model and

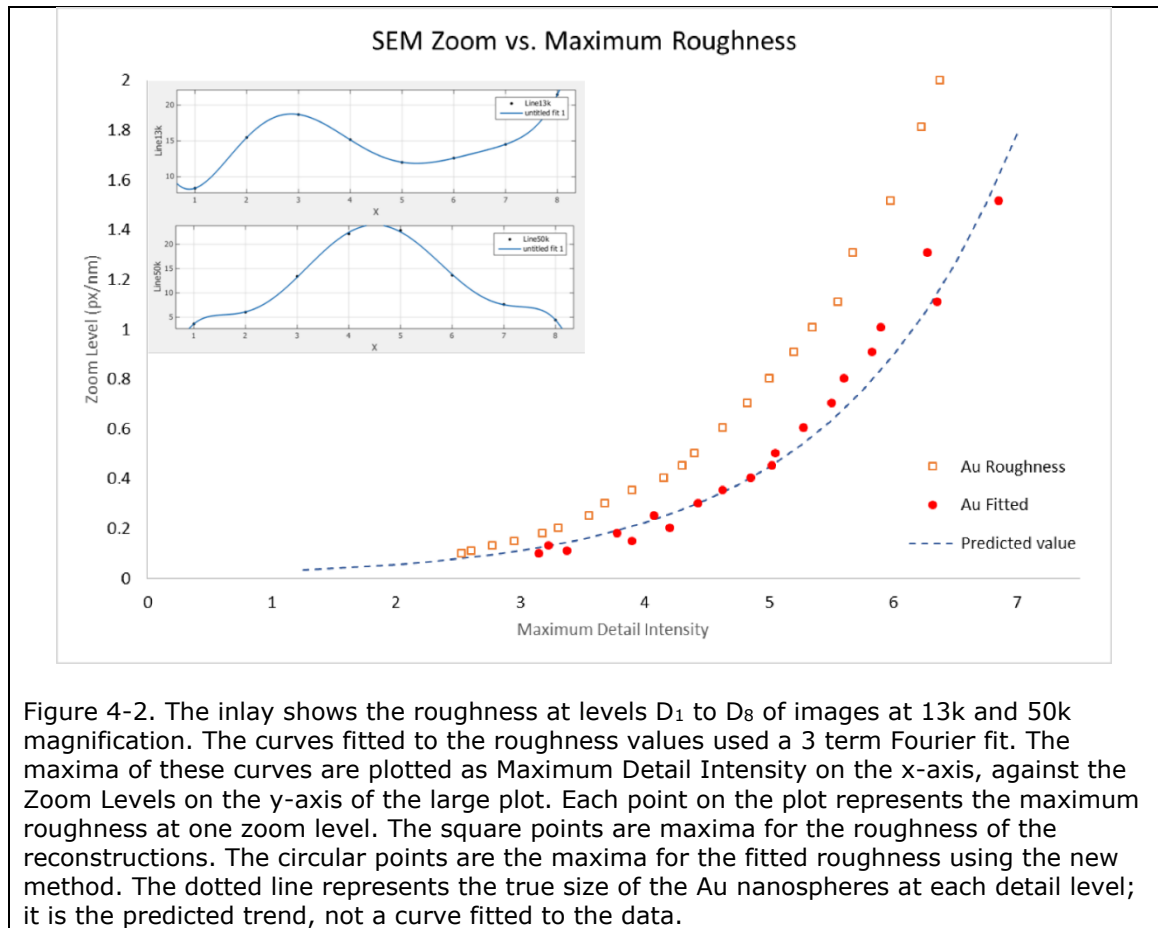
comparison of this theoretical value to measured values in real images. For structure-to-property relationships where the relevant feature size is not known in advance, this knowledge of the physical size of each level of reconstruction is critical.

Another consideration is the number of levels to be decomposed. Since each level of decomposition downsamples the original data by a factor of 2, the theoretical maximum number of levels is $\log_2(n)$, where n is the number of pixels in a line of the image.⁸¹ In practice, decompositions near this theoretical maximum are not useful. The images analyzed in this study were 890x1280 pixels and decompositions were performed with 10 levels. Size correlations, discussed below, were found to break down above detail level 7.

Wavelet sizes were correlated with physical size by imaging of a material with well-characterized physical size. Monodisperse gold nanoparticles from NIST were imaged in the Hitachi SEM at zoom levels ranging from 10k to 200k, which correspond to 0.1 pixels/nm to 2.0 pixels/nm, respectively. The DWT operates on pixels in an image. Varying zoom levels caused the nanospheres to occupy a different number of pixels, thus appearing larger at higher zoom levels. Each image was decomposed using the DWT, then images were produced from the averages of horizontal and vertical detail reconstructions. The roughness of each reconstructed image was plotted as in the inset in Figure 4-2. A smooth curve was fitted to these roughness plots so the effective detail level with the maximum roughness could be found. This imaging and analysis process was repeated on four image sets from different locations of the Au sample to eliminate

effects of local variation in nanosphere size and dispersion. Brightness and contrast were also varied between the image sets and were found to have no effect on the lateral size correlations.

The parameter used to determine the intensity of the details was the RMS roughness (R_q). The assumption used is that the maximum roughness corresponds to the average lateral size of the nanospheres in the image. The nanospheres are 54.9 nm in diameter, so the average lateral size is $\frac{\pi}{4} * d = 43.1 \text{ nm}$. The zoom levels of the images were plotted against these roughness



maxima, yielding an exponential trend (square points in Figure 4-2), as would be expected. As the zoom level was measured in pixels per nanometer, multiplying by the size of the nanospheres yields a relationship

between the wavelet detail level and the pixel size of the object being imaged. Because the Haar wavelet has a well-defined size, the theoretical curve can be similarly calculated (dashed line in Figure 4-2). It was observed that, though the measured roughness maxima trend with the right shape, they do not correspond to the theoretical values.

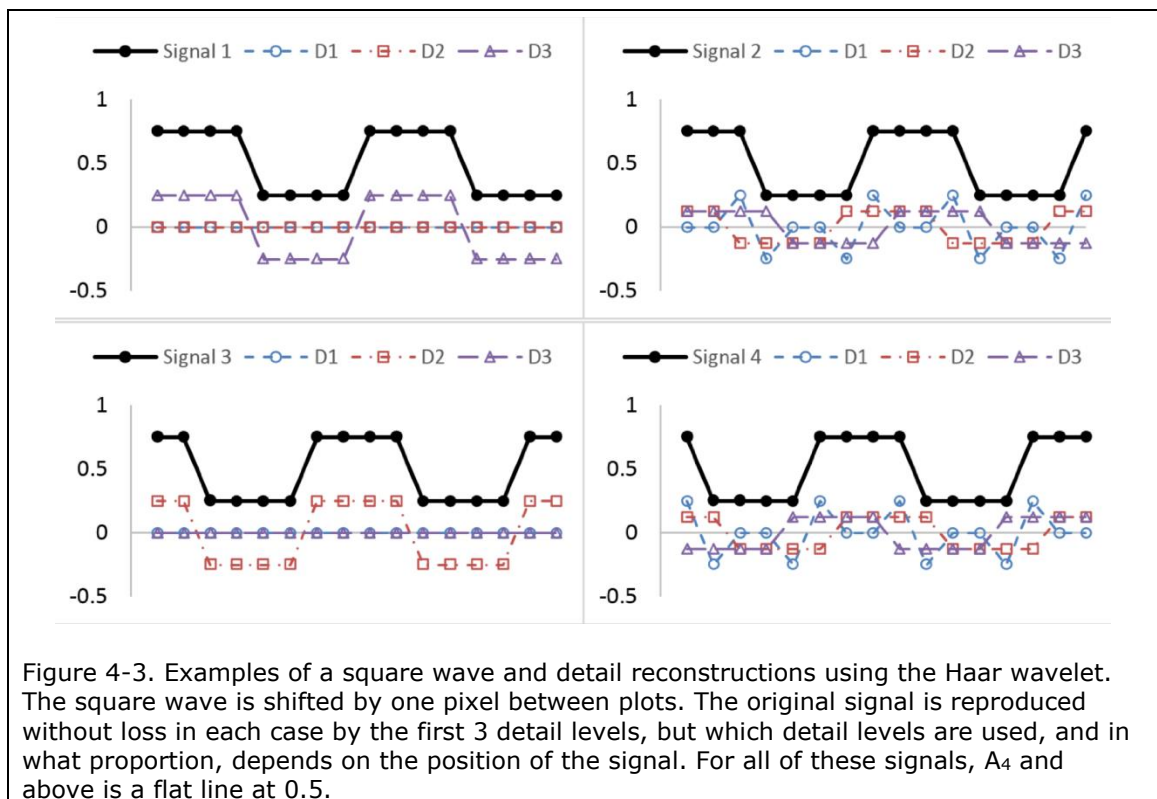
4.4.1 – Examination of roughness distribution

To understand this discrepancy, closer examination of the DWT is required. As stated earlier, the wavelet transform measures feature size as opposed to spacing. Though feature spacing is not considered, feature position is preserved. This is an advantage in many signal processing applications but is an artifact when using wavelets to measure surface roughness, where the total roughness is the metric of interest. In applications where the feature of interest is known, a mismatch between the wavelet size and the feature size is not an issue. However, when the roughness at each detail level is the metric of interest, and structure-to-property relationships are to be based on of the roughness and feature size, these lateral size correlations must be known *a priori*.

The DWT measures the fit of the wavelet with the signal at each of the detail levels. As the detail level increases, the scaling factor of the wavelet increases. As stated in the theory section above, the fit is only measured at positions corresponding to the scaling factor at each detail level, i.e. detail level 1 is examined at every pixel, detail level two is every 2nd pixel, detail level three is every 4th pixel, etc. As seen in Figure 4-3, the position of a

feature affects which detail levels model it. The example in Figure 4-3 is the simplest possible case in which the signal is a square wave, the wavelet basis used is a square wave, and the feature in the signal is the same size as the Haar D_3 wavelet. As with a change in position, a small change in size of a feature significantly changes the distribution of details that model it. The result of this is that even the simplest signal or image, containing features of only one size, will exhibit the roughness across multiple detail levels.

To examine the distribution of roughness, images were generated in Matlab using sine waves, square waves, sawtooth waves, and triangle waves of various sizes and orientations. In regards to distribution of roughness across detail levels, it was observed that the continuous signals (sine and triangle waves) behaved nearly identically and were distinct from the signals



with discontinuities (square and sawtooth). Because the images being examined are SEM and AFM micrographs, which do not contain significant discontinuities, the continuous signals were used for roughness distribution modeling.

One-dimensional signals with continuously varying sizes were analyzed and compared to the average of multiple signals with one size each. The distribution of roughness was found to be the same whether the feature sizes varied within a single line or were averaged between multiple lines. For further calculations, lines of a single size were used, then averaged to get distributions of roughness over multiple sizes.

Two-dimensional images of these signals were created for integer sizes of 1-5 pixels, then in sizes of $2^{2.5}$ to $2^{8.4}$ pixels in increments of $2^{0.1}$ pixels. Each line in the image was offset from the previous line by one pixel, so all possible positions are represented. These sizes were chosen because the wavelet transform operates on a dyadic scale. This allowed for the distribution of feature sizes equally spaced according to the scale modeled at each detail level. Whole number sizes were used below $2^{2.5}$ because fractional sizes of small features become poorly defined below 4 pixels, creating large artifacts in feature shapes. Each image was decomposed, and the roughness of each detail level reconstruction was measured. These roughness distributions represent the average roughness at each detail level for features of a given size across all possible positions.

The roughnesses of feature sizes centered at each detail level were averaged. The sizes used for each detail level are summarized in Table 4-1.

It was found that for D_4 to D_9 , the distribution of roughness was the same. D_3 was slightly off of the average of D_4 to D_9 , likely because the small feature size caused shape artifacts in the generated images for fractional sizes. D_1 and D_2 are necessarily different from the rest because there are no fractional feature sizes between 1 and 2 pixels.

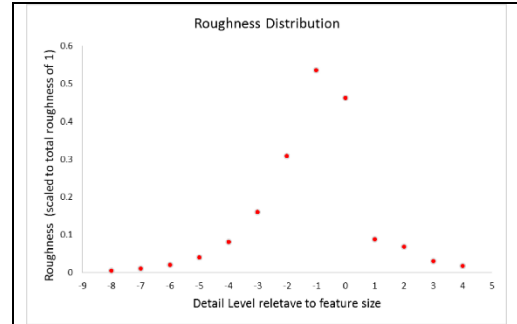


Figure 4-4. Distribution of roughness around a feature size. This shows the distribution of roughness at detail levels below and above the size of the feature centered at zero with a total roughness of 1.

The measured roughness for each size range is shown in Table S1.

Table 4-1. Feature sizes used to model each detail level. Values in parentheses are approximate values for the dyadic scale used.			
Detail Level	Sizes of features (pixels)	Detail Level	Sizes of features (pixels)
1	1	6	$2^{4.5} - 2^{5.4}$ (22.6 - 42.2)
2	2	7	$2^{5.5} - 2^{6.4}$ (45.3 - 84.4)
3	3, 4, 5	8	$2^{6.5} - 2^{7.4}$ (90.5 - 169)
4	$2^{2.5} - 2^{3.4}$ (5.7 - 10.6)	9	$2^{7.5} - 2^{8.4}$ (181 - 338)
5	$2^{3.5} - 2^{4.4}$ (11.3 - 21.1)		

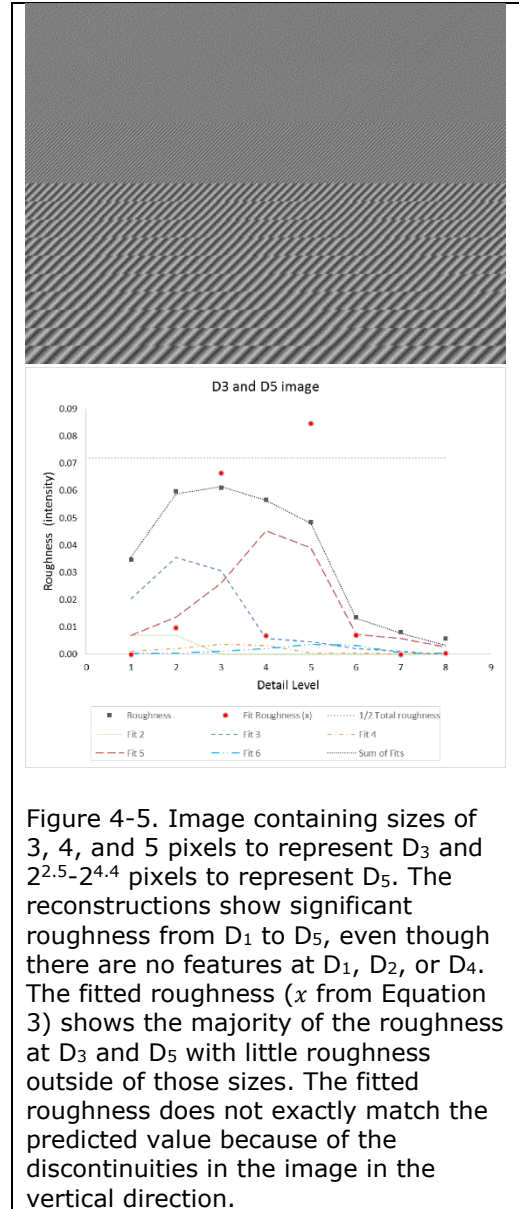
Plotting a curve of the average roughness across detail levels yields a characteristic shape that represents the roughness distribution for continuously variable sizes centered at each detail level as shown in Figure 4-4. This characteristic roughness distribution can be used as a fitting curve to fit a measured roughness distribution in much the same way that spectroscopic data are commonly fit with sums Gaussian or Lorentzian functions. Since the detail levels are discrete values, the fitting problem

reduces to a simple matrix based least-squares regression, as shown in Equation 3.

$$\min \|C \cdot x - d\|^2 \quad (3)$$

Where C is the matrix defining the detail distribution at each level, d is the detail roughness curve to be fit, and x is the coefficient matrix that represents the amount of each size present in the measured roughness curve. The C matrix is listed in Table S2, and the calculation method used is available in Reference 84.⁸⁴

When this fitting is applied to an image generated with known feature sizes, as in Figure 4-5, the roughness is more accurately attributed to features that exist in the image and roughness due to the distribution of feature positions is reduced. When this fitting procedure is applied to the Au nanospheres as above, and the zoom level is plotted against the maxima of the fits (not absolute roughness as before), the circular points shown in Figure 4-2 are obtained. The locations of these maxima agree well with the predicted curve based on the known



sizes of the nanospheres and Haar wavelet. This fitting method allows for measurement of roughness for well-defined ranges of lateral dimensions in a 2-D topography array or SEM image.

The curve used for fitting was generated with features occupying all possible positions and all sizes within a given range. These assumptions make this technique best suited for application to heterogeneous, disordered surfaces. If there are few features in a given size range or the features are ordered such that they preferentially occur in certain locations in the image, the fitting curves may not be representative because of positional bias. If the features have a narrowly distributed size range, there may be a mismatch between the true roughness and the fitted roughness due to the assumption that all feature sizes within a range are represented.

4.4.2 – Application of wavelet decomposition to catalyst surfaces

The utility of this method is investigated by application to real catalyst systems. Since the ultimate utility of a microscopic analysis method is in correlation to macroscopic properties of interest, these fitted roughness values are examined with an eye toward chemical speciation and performance of these catalysts.

Two sets of catalysts were examined. One catalyst group was synthesized in-house using the sacrificial support method and multiple precursors.^{46, 47, 73} The other group was synthesized at Pajarito Powder, LLC, all using the same precursors but different pyrolysis parameters. All catalysts are Fe-N-C type or their metal-less analogues. The in-house group was

imaged on the Hitachi SEM with a spot size of ~ 2 nm, while the Pajarito group was imaged on the FEI SEM with a spot size of ~ 10 nm (published size of 2.9 nm was never achieved on this instrument). Because different instruments were used, the two sets cannot be compared to each other. Each set was imaged with the same brightness and contrast settings on their respective instruments, allowing for comparison of catalysts within sets.

Each catalyst was imaged at a zoom level of 0.50 pixel/nm. This corresponds to wavelet and fitted sizes listed in Table S3. Due to the higher resolution available, the in-house synthesized set was also imaged at a zoom level of 2.0 pixel/nm. Chemical speciation used for correlations was from the analysis of XPS spectra. Fuel cell performance data was provided by Pajarito Powder. Because the samples

are heterogeneous, there is significant variability in surface morphology. To get an overall picture of the total surface morphology, five images per sample were acquired at 0.5 pixel/nm and ten images per sample were acquired at 2.0 pixel/nm. The roughness and fit roughness used for

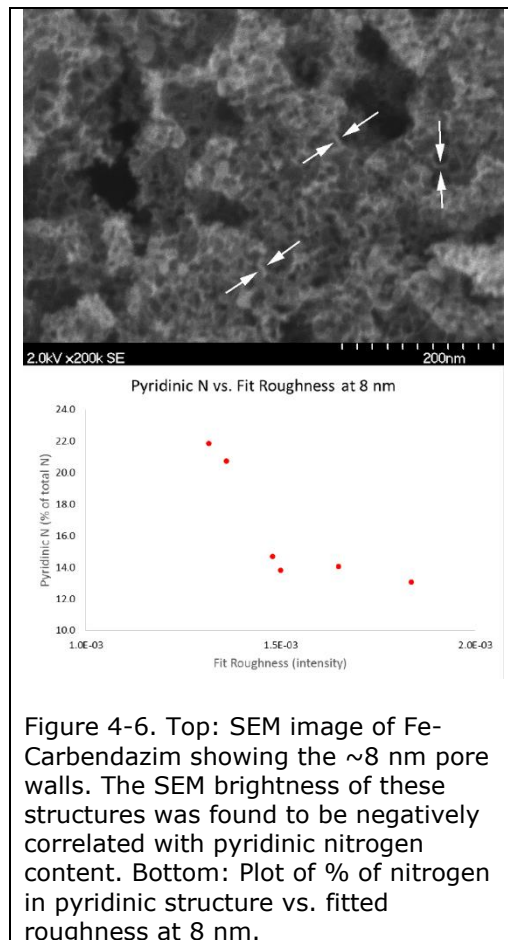
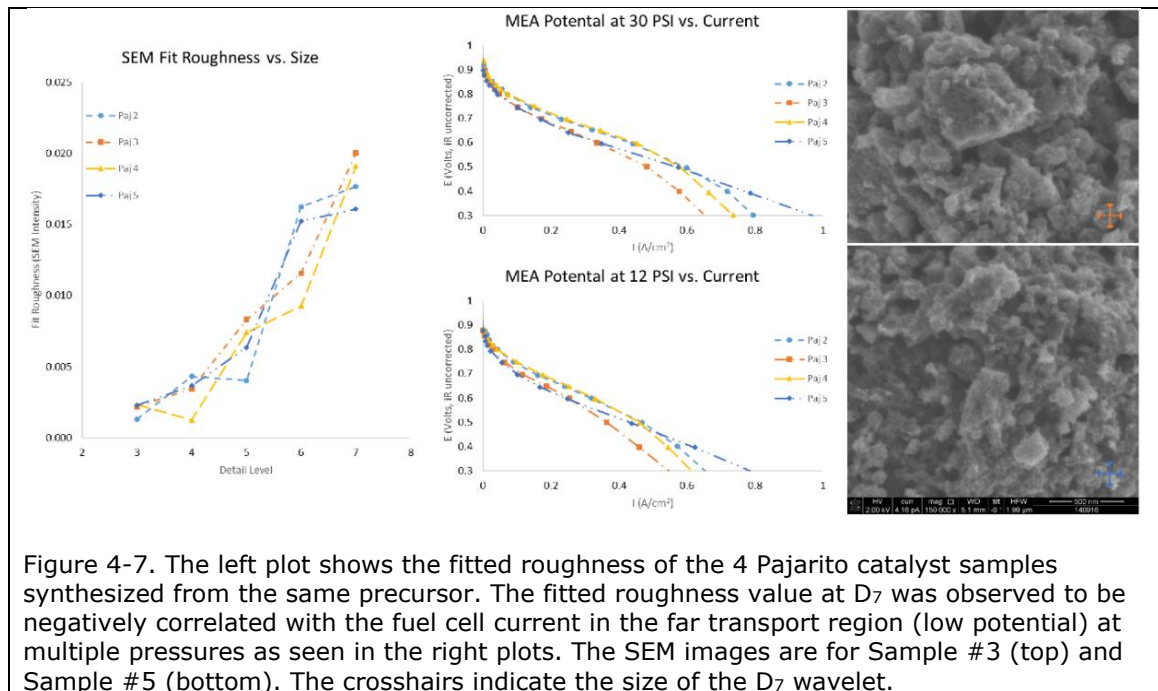


Figure 4-6. Top: SEM image of Fe-Carbendazim showing the ~ 8 nm pore walls. The SEM brightness of these structures was found to be negatively correlated with pyridinic nitrogen content. Bottom: Plot of % of nitrogen in pyridinic structure vs. fitted roughness at 8 nm.

performance and chemical correlations were the average of these values from each of the five or ten images per sample.

It was observed that as fit roughness increased for the D₃ reconstruction at 0.5 pixel/nm and the D₅ reconstruction at 2.0 pixel/nm, both of which correspond to a wavelet size of 8 nm and a fit roughness of 6-10 nm, the pyridinic nitrogen concentration decreased. This feature size of 6-10 nm corresponds to the wall thickness between voids in the catalyst as shown in Figure 4-6. It is unclear at this time if this increased roughness is due to the pore walls protruding further with less pyridinic nitrogen, or if it is a chemical effect causing the pore walls to have increased SEM brightness with less pyridinic nitrogen; future work will be performed to attempt to elucidate this. But, in either case, the roughness fitting method detects this



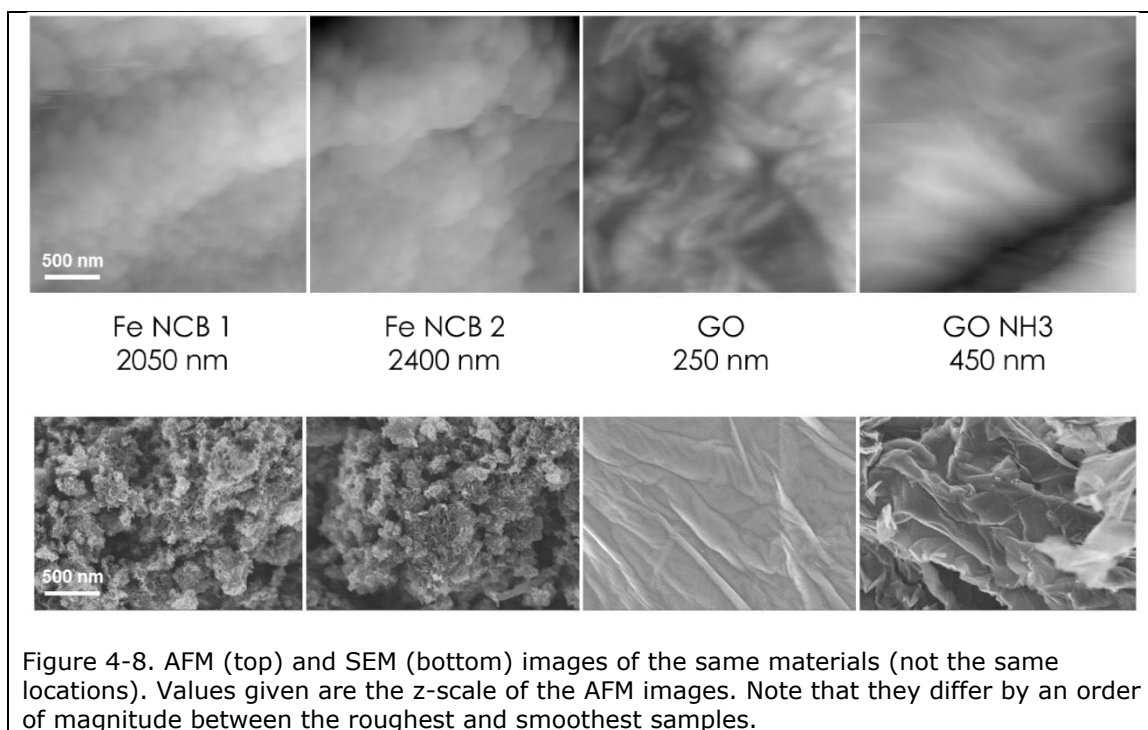
difference in intensity and quantitatively assigns it to the size range occupied

by the pore walls, allowing for correlation of morphology in a narrow length-scale range to chemical speciation.

The D_7 fit roughness was found to correlate with current in the far transport region of the fuel cell polarization curves as shown in Figure 4-7. Here, as the intensity of features in the 90 to 180 nm range increased, the current in the transport regime decreased. This range may be related to the particle size of the catalyst, though it is difficult to discern if these are separate particles or agglomerates. Future work will include independent measurement of the particle sizes of these catalysts for comparison. As this feature size is the largest that can be measured by the wavelet reconstructions at this zoom level, future work will also include imaging at a lower zoom level to better examine features at this, and larger, length scales.

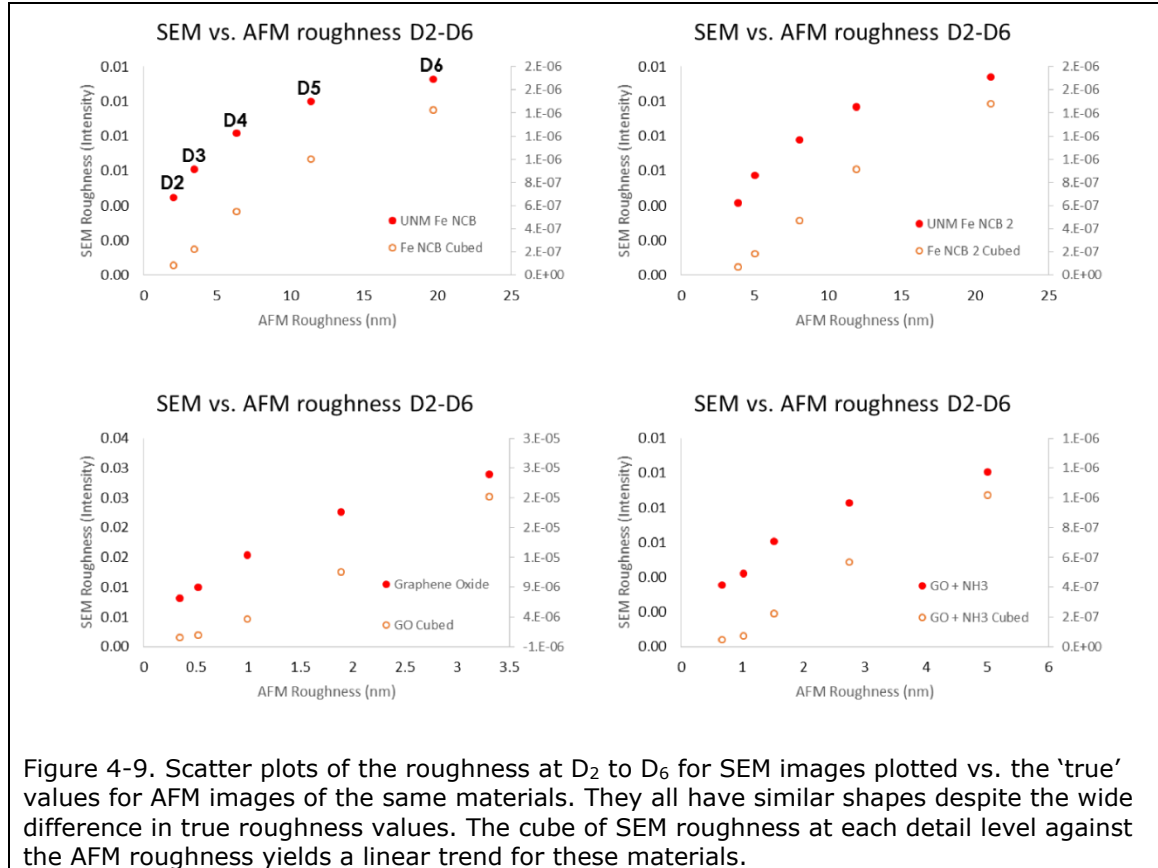
4.4.3 – Examination of the relationship between SEM and AFM images

At low voltages, the secondary electron signal from SEM images is known to contain surface information.⁷⁸ However, this surface information is not necessarily topographic. The SEM signal contains information on chemical heterogeneities and is influenced by feature shape as well as orientation with respect to the detector. Examination of the roughness of the wavelet reconstructions in both SEM and AFM of the same materials yields some insight into the relationship between roughnesses measured with these two imaging methods.



Four materials were imaged on both SEM and AFM, all with an effective zoom level of 0.5 pixel/nm (Figure 4-8). When a scatter plot of roughness at each detail level from D_2 to D_6 for SEM and AFM is created, a consistent shape is generated across all four materials as shown in Figure 4-9. By inspection, this shape appeared to be a cube root function, so the cube of SEM roughness was plotted against the AFM roughness. These scatter plots appear nearly linear across these four samples. The underlying cause for a possible cubic relationship between length-scale specific roughness in SEM and AFM has not been explored. Further, the slopes are different, indicating that there is not a fixed relationship between absolute roughness in the SEM and AFM across different samples. However, the appearance of this nearly linear trend for these scatter plots is evidence that, in this class of nanostructured carbon materials, the information obtained from SEM images is largely topographic. As a result, it is reasonable to treat DWT roughness

distributions from SEM images as representative of the true roughness distribution of these surfaces.



4.5 – Conclusion

Wavelets have been previously used for surface and image filtering where the approximate size of the feature(s) of interest was known in advance. In the cases of structure-to-property analysis and measurement of complex, heterogeneous surfaces, there is no advance knowledge of the feature size of interest and/or quantification of all size ranges is desirable. Here, the DWT was examined as a means of quantitative surface analysis across multiple length scales without advance knowledge of the features of

interest. It is observed that, though the size of the wavelet is known, it does not directly correlate to the physical size of the features being measured. To address this issue, the distribution of roughness in wavelet reconstructions was examined and found to be consistent above D_3 . This roughness distribution was used as a fitting basis for measured roughness curves and was found to be in good agreement with the known physical size of features in SEM images.

The DWT and fit roughness was applied to SEM and AFM images of non-PGM catalysts. Analysis with this method yields relationships not previously seen. SEM intensity of pore walls in the 6-10 nm range is seen to correlate with pyridinic nitrogen concentration, and SEM roughness in the 90-168 nm range correlated with transport-limited performance in a fuel cell. Previous surface analyses of these complex, heterogeneous materials had not discerned these relationships.

Application of the DWT to SEM and AFM of the same materials yielded some relationships that bear further investigation. The plots of SEM roughness vs. the AFM roughness at each detail level produced a trend that was observed for all samples examined. It is observed, though not understood, that the cube of the SEM roughness at each detail level has a nearly linear relationship with the AFM roughness. Though the relationship is not understood, this provides some evidence that the information in the SEM images of these materials is topographic, and that the measured roughness at component detail levels correlates to the true length-scale specific roughness.

4.6 – Acknowledgements

This material is based upon work supported by the National Science Foundation Graduate Research Fellowship Program under Grant No. 1418062 and the DOE Development of Novel Non-PGM Electrocatalysts for PEM Fuel Cell Applications project.

Chapter 5 – FIB/SEM Tomography Method

5.1 – Introduction

This chapter focuses on the cross-sectioning and imaging techniques, instrument parameters, and areas of concern for utilization of FIB tomography. Post-processing of the image stacks is an area of ongoing research that is not addressed in detail here.^{85, 86} My optimization of FIB tomography for PGM-free materials has not been published as a stand-alone project, but it has contributed to publication of manuscripts by Serov, *et al.* and Stariha, *et al.*, both in the Journal of Power Sources in 2016.^{66, 67}

5.2 – Background

The performance of any catalyst in real-world application is influenced by the intrinsic activity of the catalyst itself, the transport properties of the catalyst particles, and how the catalyst particles integrate with ionomer in the electrode layer. The structure of the catalyst layer determines the properties of bulk mass transport, electron transport, proton transport, and water management. Knowledge of the structure of the final catalyst layer is critical for both understanding the performance of the fuel cell and for rational design of catalysts that interact favorably with ionomer. Understanding catalyst layer morphology requires 3-D analysis of the internal structure of the catalyst layer.

Imaging catalyst layer volumes can be achieved through a few different methods. One of the most frequently used is nano-CT (x-ray computerized tomography). This method can produce voxel sizes small as

16 nm and allows for differentiation between some solid phases as well as the identification of pores.⁸⁷ Nano-CT is computationally intensive, the modeling and post-processing are complicated and prone to significant error, and it requires specialized equipment (either a dedicated instrument with a low x-ray power or a beamline). Neutron imaging is another powerful tool for imaging electrode structure. It is especially good at imaging water inside of the catalyst layer, but it has a much coarser spatial resolution of several microns.^{88, 89} Further, neutron imaging can be performed only on a few specially equipped neutron sources. FIB tomography has spatial resolution very similar to nano-CT and uses a dual-beam FIB/SEM that is relatively common in analysis laboratories.^{67, 90} This method allows for direct reconstruction of the solid and pore phases without the need for complex modeling or resource-intensive calculations. While FIB tomography does not allow for differentiation of solid phases, the higher availability of analysis instrumentation and the simplicity of reconstruction make FIB tomography an attractive alternative that is gaining in popularity.

FIB tomography has been in development since the early 1990s and was applied to analysis of fuel cell catalyst layers by Thiele and Zeigler in 2011.⁹⁰⁻⁹³ The initial application of this technique allowed for reconstruction of catalyst layers of Pt suspended on carbon. These catalyst layers are generally about 5 μm thick, have pores smaller than 1 μm , and have high e-beam contrast due to the high Pt content. Extension of this technique to PGM-free catalyst layers required adapting the technique to layers that are

on the order of 100 μm thick, have pores of several microns, and contain less than 1% metal.

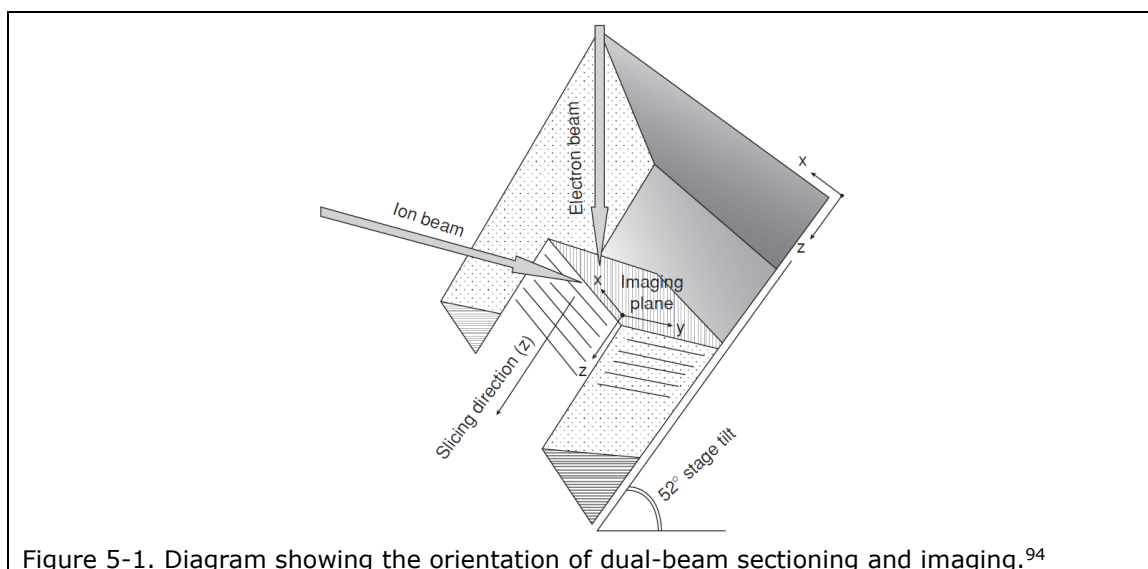
5.3 – Materials

The instrument used for electrode sectioning and imaging was an FEI Quanta 3D Dual beam scanning electron microscope equipped with a field emission gun. The gallium liquid metal ion source was operated with an accelerating voltage of 30 kV and images were collected in secondary electron mode. All imaging and milling parameters presented are specific to this instrument. Image analysis was performed using ImageJ with the StackReg plugin and Matlab routines written in-house.

5.4 – Experimental method

Fundamentally, the process for creating a series of images in the FIB/SEM dual-beam instrument is to cut a cross-section with the ion beam, image with the e-beam, then repeat until the desired number of images have been acquired. The orientation of the beams and the sample being imaged are illustrated in Figure 5-1. Analysis time is dependent on the desired size of the analysis volume, imaging time as determined by the image resolution, and slice thickness (resolution in the z-direction). Acquisition of 100 images through a surface of 3 μm x 2 μm can be completed in ~ 3 hours, while 180 images through a surface of 20 μm x 10 μm takes ~ 6 hours.

Before sectioning is initiated, the surface of the electrode must be protected with a Pt (or other metal) cap. This protective cap serves two purposes. First, it protects the electrode from stray ions. This is necessary because, although the ion beam is well focused, it still has a distribution of intensity and there are always stray ions outside of the intended beam line



that will damage anything they interact with. The second reason is to allow for clean cutting without curtaining. Curtaining occurs when there is a variable thickness or hardness in the target material. Where the material is thicker/harder, the cutting is less efficient and leaves a vertical line (Figure 5-2). The collection of these vertical lines can resemble hung draperies, hence the name. The deposited Pt has a smooth surface as compared to the electrode. Further, Pt is more resistant to ion sputtering than the carbon electrode. As a result, a higher intensity ion beam is necessary to cut through the Pt. Once the ion beam has broken through the Pt, it quickly cuts through the electrode without any stray ions cutting into the carbon.

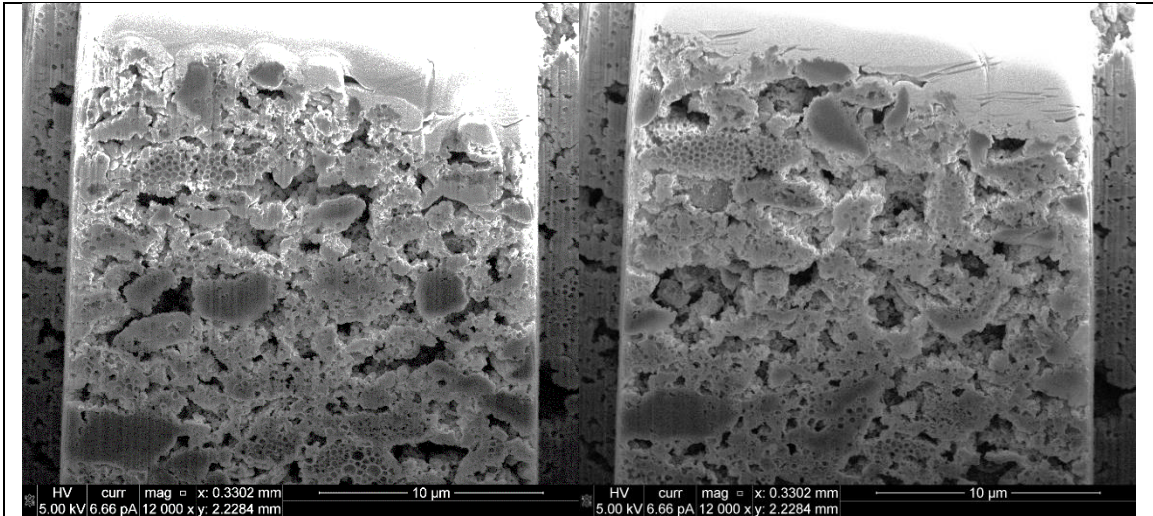


Figure 5-2. FIB sections illustrating the curtaining effect and Pt cap protection. The section on the left was from the setup phase and cutting had not yet reached the Pt cap. One of the results of cutting directly into the electrode are the vertical lines, known as curtaining. These are not imaging artifacts; they are vertical grooves in the cross-section surface. The image on the right is the same electrode cut through the Pt cap.

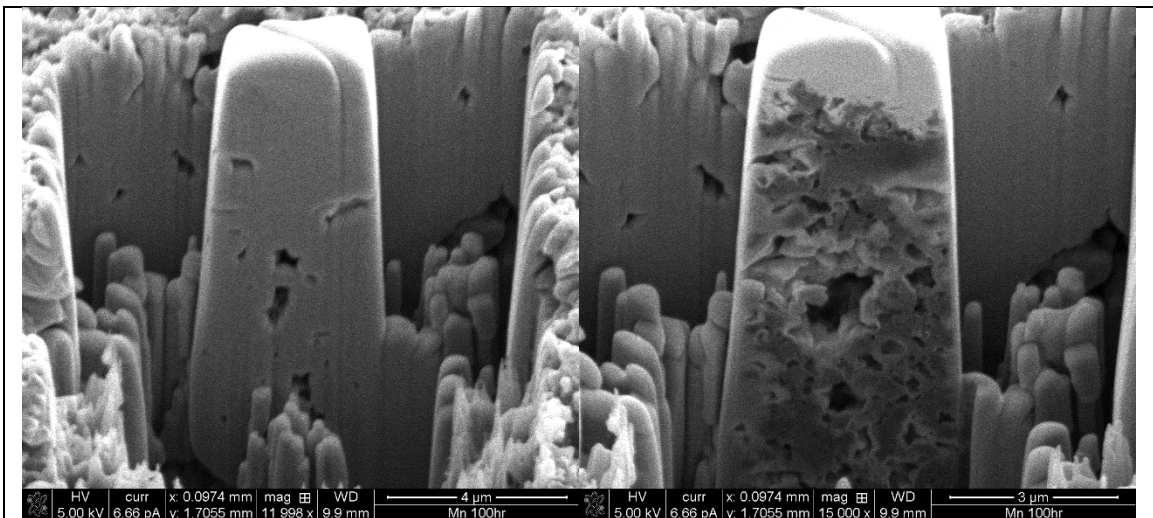


Figure 5-3. SEM images showing an analysis area. The left image shows the area after milling the initial trenches. The absence of pores is due to the high ion beam current used to create the trenches. High ion beam current damages the electrode and destroys pores. The right image shows the same analysis area after low current cutting.

After Pt deposition, trenches must be milled around the analysis area. These trenches allow for a line-of-sight from the e-beam to the cross-section surface as well as providing space for the secondary electrons ejected from the cross-section to escape and be drawn to the detector. These trenches are illustrated in Figures 5-1 & 5-3.

With the analysis area protected with a Pt cap and exposed by trenches, imaging and cutting can commence. The parameters of both the ion beam and e-beam are critical. If the ion beam current is too high, it will damage the sample and the analysis will not be representative of the electrode structure. If too low, it will either not cut deep enough to give a complete section, or will take so long that imaging of the volume cannot be completed in one session. The e-beam current must be high enough to provide adequate contrast, but not so high that it damages the ionomer during imaging. The e-beam voltage determines the imaging depth, and can also cause damage to the ionomer if it is either too high or too low. Beam parameters for different electrodes and analysis volumes are listed in Table 5-1. The thickness of the Pt layer depends on the surface area to be covered and the roughness of the electrode surface. The Ga^+ current for Pt deposition should be set such that it takes no fewer than 5 minutes for every μm of thickness (e.g. 4 μm thick deposition should take no less than 20 minutes). The imaging parameters depend on the ionomer used in the electrode. For Nafion used in PEM electrodes, 5 kV provides good resolution and surface-specific images without damaging the ionomer. For AS-4 ionomer used in

Table 5-1. Beam parameters used for PGM-free FIB/SEM cross-sectional imaging.			
Parameter	3 μm x 2 μm PEM	20 μm x 10 μm PEM	20 μm x 10 μm alkaline
Pt thickness	1 μm	4 μm	4 μm
Pt dep. current	30 pA	1 nA	1 nA
Ga^+ current cutting	0.5 nA	3 nA	3 nA
e^- current	6.7 pA	6.7 pA	13 pA
e^- voltage	5 kV	5 kV	15 kV

alkaline fuel cells, the 5 kV accelerating voltage caused nearly instant ionomer degradation at all currents. Increasing the e-beam current to 15 kV reduced this damage such that no damage was observed through the entire 120 image set. Increasing the accelerating voltage increases the e-beam penetration depth, allowing the energy to be dispersed through a greater volume of material. In the alkaline ionomer, this increased dissipation volume was the dominating parameter, whereas with Nafion, higher accelerating voltage caused greater damage.

Image stacks of 100-200 images can be acquired in a session of 3-8 hours, depending on the volume. The resolution in the z-direction depends on the cutting current (thickness of each cut) and whether images are acquired for every ion beam cross section. For the 3 μm x 2 μm analysis volumes, about 100 images were acquired by imaging every 2nd cross section. This yields a resolution in the z-direction of about 20 nm. Collecting an image for every cross section would yield a resolution of about 10 nm, but would effectively double the analysis time. The 20 μm x 10 μm analysis volumes typically yield about 180 images for a resolution in the z-direction of 55 nm. The number of images to be acquired, volume to be analyzed, and resolution of each image all must be determined to fit within the time available for analysis. On this instrument, the maximum size cross section achieved was a single section 150 μm wide. For this analysis, the trenching and polishing took 8 hours to obtain the single cross section. As this sample was a titanium-based electrode, the cutting time was slightly longer than for carbon electrodes. However, for titanium or carbon-based electrodes, at this

scale creating additional cuts to achieve a stack and volume reconstruction would not be possible in a single session.

The results of analyses on PGM-free electrodes can be seen in the published works listed at the beginning of this chapter.^{66, 67} The downloadable supplementary information contains a representative image stack, and the detailed operation procedure created by this writer and Sarah Stariha is in Appendix B.

Chapter 6 – Synthesis to Chemistry and Performance Relationships

The following chapter is presented as it was originally published in the Journal of Power Sources in 2017.⁶⁸ I gratefully acknowledge the work of my co-authors: Michael Dzara, Chilan Ngo, Svitlana Pylypenko, Alexey Serov, Sam McKinney, Jonathan Gordon, Plamen Atanassov, and Kateryna Artyushkova. My contribution to this work included: Catalyst synthesis, RDE data acquisition and analysis, MEA data acquisition and analysis, data processing, correlation analysis, and interpretation of results.

Workman, M. J.; Dzara, M.; Ngo, C.; Pylypenko, S.; Serov, A.; McKinney, S.; Gordon, J.; Atanassov, P.; Artyushkova, K. "Platinum Group Metal-Free Electrocatalysts: Effects of Synthesis on Structure and Performance in Proton-Exchange Membrane Fuel Cell Cathodes" *J Power Sources* (2017), 348, 30-39.⁶⁸

6.1 – Abstract

Development of platinum group metal free catalysts for the oxygen reduction reaction (ORR) in proton exchange membrane fuel cells (PEMFCs) requires understanding of the interactions between surface chemistry and performance, both of which are strongly dependent on synthesis conditions. To elucidate these complex relationships, a set of Fe-N-C catalysts derived from the same set of precursor materials is fabricated by varying several key synthetic parameters under controlled conditions. The results of physicochemical characterization are presented and compared with the

results of rotating disk electrode (RDE) analysis and fuel cell testing. We find that electrochemical performance is strongly correlated with three key properties related to catalyst composition: concentrations of 1) atomically dispersed Fe species, 2) species in which N is bound to Fe, and 3) surface oxides. Not only are these factors related to performance, the chemistries are shown to correlate with each other. This study provides evidence supporting the role of iron coordinated with nitrogen as an active species for the ORR, and offers synthetic pathways to increase the density of atomically dispersed iron species and surface oxides for optimum performance.

6.1 – Introduction/Background

Many studies focus on replacing platinum group metal (PGM) catalysts for the oxygen reduction reaction (ORR) at the cathode of proton exchange membrane fuel cells. The family of transition metal-nitrogen-carbon (MNC) electrocatalysts has been investigated extensively over the years^{46, 49, 56, 73, 95-116} as a PGM-free alternative, with several recent reports demonstrating dramatic improvement in ORR activity and durability in fuel cell operation.^{66, 104, 117} To further these advances and understand the underlying mechanisms, continued focus is required to link structural composition with ORR activity and durability.^{95, 103, 111, 114}

In order to provide insight for rational design of optimized catalyst materials, it is necessary to elucidate the roles various chemistries play in the activity and durability of PGM-free catalysts. The effect of different metal species, contributions of various N moieties, and impact of the C support

network are of central importance. Among the various available transition metal precursors, Fe is the most frequently studied due to the high activity and stability of the resulting catalysts.¹¹⁸ In these materials, Fe is primarily manifested in two forms: Fe-rich phases such as metallic particles and carbides,^{45, 61, 119-121} or atomically dispersed Fe coordinated to N in a variety of configurations.^{103, 122, 123} Nitrogen functionalities identified in MNCs include – but are not limited to – pyridinic, graphitic¹²⁴, hydrogenated as pyrrolic or hydrogenated pyridinic¹²⁵, cationic as quaternary or protonated, and the N coordinated with atomically dispersed Fe species (N-Fe). Multiple detailed structure-to-property and theoretical studies show that Fe coordinated to N (FeN_x) forms active sites that catalyze the complete reduction of oxygen to water, while other N types such as hydrogenated and graphitic facilitate the partial reduction of oxygen to hydrogen peroxide.^{95, 103, 114, 126} In this work, “N-Fe” is used when discussing measured concentrations of N bound to Fe and “FeN_x” is used when discussing the idealized active sites. This distinction is significant because N could be bound to Fe in nonactive configurations and the potential presence of single atom Fe particles cannot be discounted. Surface oxides present in the C network are important (indirect) indicators of defects which influence the formation of active FeN_x sites.^{95, 127} An important aspect of the C network is its contribution to hydrophilic/hydrophobic properties that are critical for the integration of catalyst powders into fuel cell catalyst layers. Length-scale specific morphology of the catalyst also plays a very important role, particularly at the point integrating the catalyst into catalyst layers.^{64, 107} The distribution and accessibility of active sites as well

as the mass transport and water management properties of catalyst layers depend on the chemical composition, surface energy, and morphology of the catalysts themselves.

The pyrolytic routes typically employed in the synthesis of MNC catalysts result in very heterogeneous materials with a multitude of C, metal, and N moieties, as well as varying physical structure. Development of PGM-free catalysts with improved activity and durability requires elucidation of the interplay between synthesis methodologies and catalyst composition, morphology, and both electrochemical and fuel cell performance characteristics. RDE testing is important for pre-screening catalyst activity and stability, as well as for mechanistic studies.¹¹⁸ Beyond RDE, it is crucial to determine correlations between catalyst synthesis, physicochemical properties, and performance in membrane electrode assembly (MEA) tests; these experiments evaluate materials upon integration into the catalyst layer, which in turn affects mass, electron, and proton transport.^{107, 128}

We have previously shown that electrocatalysts synthesized from Fe and nicarbazin precursors using the sacrificial support method (SSM) demonstrate excellent activity and durability.^{66, 104} The SSM involves using templates to create free-standing, highly porous materials with tunable pore size distributions. These materials are formed from pyrolytic treatment of C, N, and metal sources.^{46, 49, 66, 104, 107, 127} After pyrolysis, the materials are leached in order to remove the template and undesired residual metal-rich phases. A second heat treatment improves catalyst activity and durability. Type and size of the template, mixing method, etching conditions, and

pyrolysis conditions (temperature, gas, duration) all affect catalyst chemistry and morphology and its subsequent performance in both RDE testing and MEA operation. Because the type of template used affects the resultant catalyst structure and porosity, it also affects catalyst-ionomer interactions in the catalyst layer.¹²⁹ The ratio of ionomer to catalyst, as well as the method of the catalyst layer fabrication, also play critical roles in MEA performance.¹³⁰ Optimized procedures for ink preparation and MEA fabrication have previously been reported for this class of materials.^{66, 67}

The goals of this study are to elucidate: 1) chemistry-structure-performance relationships in nicarbazin-derived PGM-free catalysts, and 2) the effects of various synthetic parameters on catalyst composition, structure, and performance. A series of electrocatalysts with the same carbon/nitrogen precursor and Fe loading are fabricated under different synthetic conditions and tested for electrochemical performance in both RDE and MEA. The materials are characterized by x-ray photoelectron spectroscopy (XPS) and energy dispersive x-ray spectroscopy (EDS) on a transmission electron microscope (TEM) to build correlations between synthetic parameters, performance, and surface and bulk composition of these catalysts, with focus on their heterogeneity at multiple length scales. Additional studies into the effects of catalyst and electrode morphology on performance are ongoing.

We observe that performance is strongly correlated with the concentration of N species coordinated with Fe, as well as the amount of surface oxides present. Catalyst performance is hindered by Fe-rich phases,

even in the presence of the ideal, atomically dispersed Fe species. Specific synthetic parameters that affect these chemistries and can be used for tuning catalyst performance are laid out. Finally, we show that these materials are fairly chemically homogenous at scales of over ~ 100 nm, but are highly heterogeneous at the few-nanometer scale. Therefore, caution should be exercised in drawing structural or chemical conclusions based on high-resolution observations.

6.2 – Experimental

6.2.1 – Synthesis

Iron-Nicarbazin (Fe-NCB) electrocatalysts were prepared as follows: First, a calculated amount of silica (Stöber spheres synthesized in-house with a diameter of 370 nm, plus Cab-O-Sil[®] LM-150 and OX-50) was combined with multi-wall carbon nanotubes (Cheaptubes[®] 30-50 nm x 10-20 μ m), iron nitrate ($\text{Fe}(\text{NO}_3)_3 \cdot 9\text{H}_2\text{O}$, Sigma-Aldrich) and nicarbazin (1,3-bis(4-nitrophenyl)urea; 4,6-dimethyl-1H-pyrimidin-2-one, Sigma-Aldrich). The reagents were mixed with sufficient water to wet the powder and form a viscous gel, which was then dried with continuous stirring at 45 °C, then heated at 85 °C overnight. The resulting solid material was ground to a coarse powder in an agate mortar, then to a fine powder in an agate ball mill. This powder was then subjected to heat treatment (HT) in a controlled atmosphere of 7% H_2 /93% N_2 (flow rate 120 cc min⁻¹). HT 1 consisted of insertion into a furnace at 525 °C then immediately setting the furnace temperature to 900 °C. Once the furnace reached 900 °C, the temperature

was increased to 975 °C at a rate of 10 °C min⁻¹. The temperature was held at 975 °C for 45 minutes, then the catalyst was quenched by removing the tube from the furnace. After HT 1, the sample was ground in an agate ball mill then leached with a 2:1 mixture of 25% HF:35% HNO₃ for 3 days. The catalysts were then washed with DI water until neutral pH was reached and dried at 85 °C overnight. A second HT was performed at 950 °C for 30 minutes in reactive (7% NH₃/93% N₂) atmospheres. The final product was ground in an agate ball mill for 1 hour. The varied synthetic parameters are shown in Table 6-1.

6.2.2 – Rotating disk electrode

RDE measurements were performed with a glassy carbon working electrode and a graphite counter electrode. Ink composition was 5 mg of catalyst in 850 µL 4:1 water:isopropanol and 150 µL 0.5 wt.% Nafion

Table 6-1. Table of varied synthesis parameters. Amounts of Stöber glass and CNT are in grams. All samples used 12.5 g nicarbazin and 1.2 g iron nitrate nonahydrate.						
Sample	Stöber	CNT	Etch Prep	Etch	HT2 method	HT2 gas
2	1.0	1.0	Mortar & Pestle	HF/HNO ₃	950 °C 30 min, quench	NH ₃ /N ₂
8	1.0	1.0	Ball mill	HF/HNO ₃	950 °C 30 min, quench	NH ₃ /N ₂
9	5.0	1.0	Ball mill	HF/HNO ₃	950 °C 30 min, quench	NH ₃ /N ₂
10	1.0	-	Ball mill	HF/HNO ₃	950 °C 30 min, quench	NH ₃ /N ₂
13	1.0	1.0	Ball mill	HF/HNO ₃	950 °C 45 min, quench	H₂/N₂
14	1.0	1.0	Ball mill	HF	950 °C 30 min, quench	NH ₃ /N ₂
15	1.0	1.0	Ball mill	HF/HNO ₃	950 °C 45 min, quench	NH ₃ /N ₂

solution deposited to a catalyst loading of 600 µg cm⁻². The electrolyte was O₂ saturated 0.5 M H₂SO₄ at room temperature. A scan rate of 5 mV s⁻¹ was used with a rotation speed of 1600 RPM. Data was recorded vs. a saturated

Ag/AgCl reference electrode, then converted to reversible hydrogen electrode potentials by addition of 215 mV. The half-wave potential was determined by calculating the second derivative of the sigmoid.

6.2.3 – Fuel cell testing

Fuel cell testing was performed by Pajarito Powder, LLC. MEAs with an area of 5 cm² were prepared from gas diffusion electrodes (GDEs) pressed with XL Nafion[®] membrane using PTFE-impregnated glass-fiber sub-gaskets at 131 °C for 10 minutes at 450 psi, then cooled under 1 psi pressure. Sub-gasket thickness for the anode was 150 µm and 250 µm for the cathode. The GDE was sprayed using a Sono-Tek Exacta-Coat automated spray system delivering 1 ml min⁻¹ ink through a 25 kHz ultrasonic nozzle onto SGL 29BC Gas Diffusion Layer preheated to 65 °C. The ink was deposited at a rate of 40 µg cm⁻² per deposition pass, for a total of 3 mg_{catalyst} cm⁻² and ~75 µm thick electrode. The inks were composed of 2:1 isopropyl alcohol:deionized water (v:v), catalyst, and D2021 Nafion[®] (measured to a final loading of 45 wt%) dispersion mixed to a ratio of 3.5wt% total solids. A 50 mL vessel containing the ink ingredients was placed in a water-cooled bath and mixed for 30 min using an IKA T-18 high shear mixer with the S18-19G dispersing element at 18,000 RPM.

The MEAs were loaded into the cell testing assembly (Fuel Cell Technologies Inc.) using single serpentine pattern graphite flow plates and the cell hardware was assembled using 40 inch-lbs torque. Testing parameters were 80 °C, 100% RH, 250 sccm H₂/200 sccm air at the anode

and cathode, respectively, at an absolute pressure of 1.65 atm. The MEA was preconditioned with a potentiostatic hold at 0.3 V for 10 minutes. Data was then collected potentiostatically with 60 seconds potential holds and the current at the end of the hold reported. Data is reported without correction.

6.2.4 – XPS

XPS spectra were acquired on a Kratos Axis Ultra X-ray photoelectron spectrometer using a monochromatic Al K α source operating at 300 W, and data analysis and quantification were performed using CasaXPS software. Three regions per samples were analyzed. Survey spectra were acquired at 80 eV pass energy. High resolution O 1s, C 1s, N 1s, and Fe 2p spectra were acquired at 20 eV pass energy. No charge neutralization was necessary. High resolution C 1s and N 1s spectra were fitted with a 70% Gaussian/30% Lorentzian line shape with fixed full width half max of 1.0-1.2 eV for C and of 1.3-1.5 eV for N.

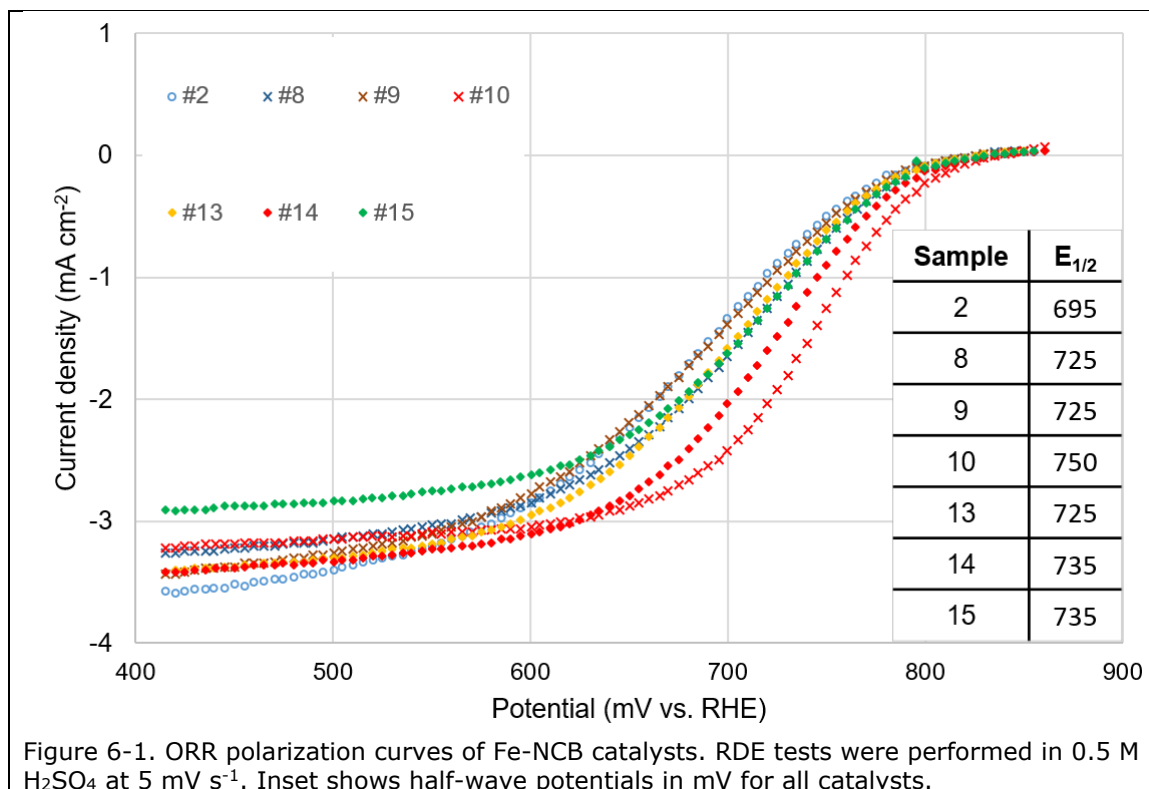
6.2.5 – TEM/EDS

Scanning transmission electron microscope (STEM) imaging and energy dispersive x-ray spectroscopy (EDS) measurements were conducted using an FEI Talos F200X operated at 200 kV. Compositional EDS maps were acquired for up to 60 min per area (typically ~10 min), and data was processed using Bruker ESPRIT software.

6.3 – Results

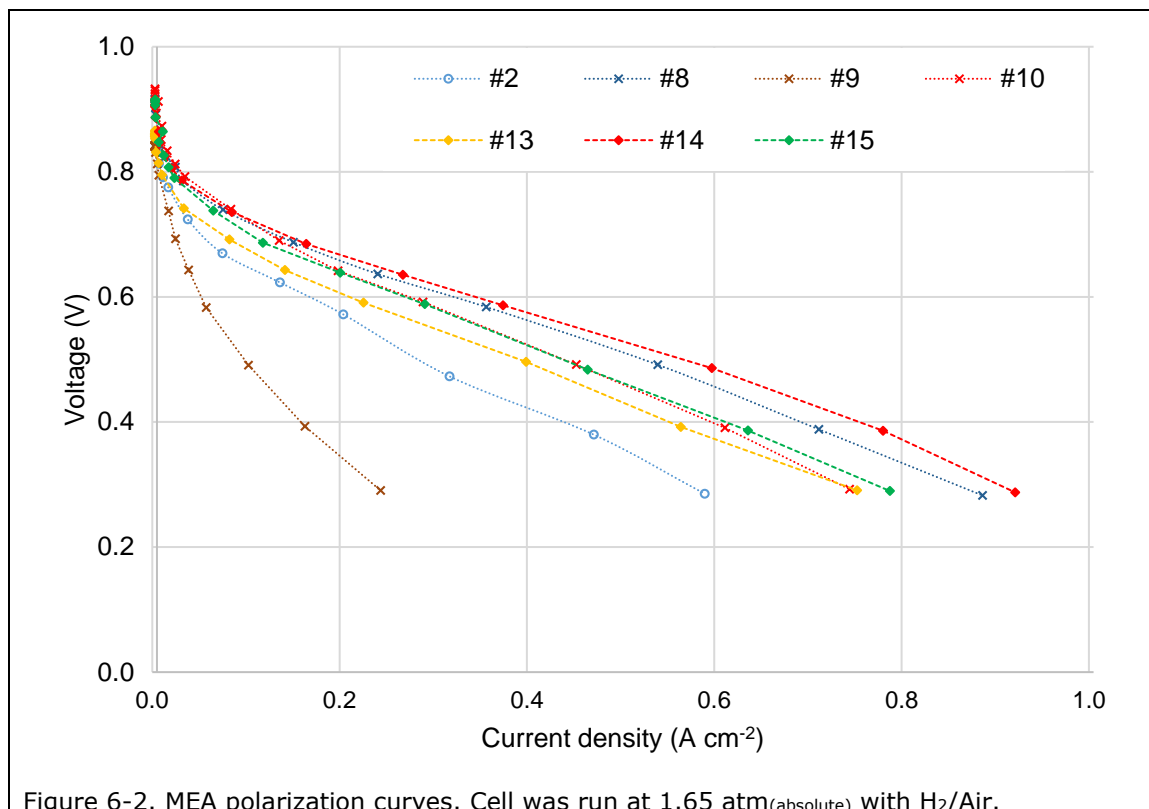
6.3.1 – Rotating Disk Electrode

Electrochemical activity was measured using the half-wave potential ($E_{1/2}$) from RDE measurement (Figure 6-1), with $E_{1/2}$ values ranging from 695 to 750 mV. The lowest $E_{1/2}$ corresponds with Sample 2, which contained excess Fe particles, perhaps due to incomplete leaching. The highest $E_{1/2}$ was generated by Sample 10 (synthesized without CNT). All other samples have similar $E_{1/2}$.



6.3.2 – Fuel Cell

Fuel cell performance was tested in a single cell MEA (Figure 6-2), results presented without iR correction. All operation regions show significant spread in performance. Kinetic performance, characterized by current densities at 0.8 V, was highest for Sample 10, which also exhibited the best $E_{1/2}$. This is likely due to higher density of active sites in the sample without CNTs since CNTs do not host active sites themselves and their addition decreases the amount of material available for active site formation. The lowest kinetic performance was observed in Samples 2, 13, and 9. Sample 2 suffered from incomplete leaching that resulted in a significant amount of



excess Fe in the final product. PGM-free catalysts containing excess Fe have previously been reported to exhibit poor performance.⁵⁶ Sample 9 was

synthesized with five times the amount of silica spheres as the other samples and was an outlier in all regimes of fuel cell testing. Although this additional silica did not significantly change the chemical composition, as will be presented below, it clearly had a profound effect on integration of the catalyst into the catalyst layer. Cross-sectional imaging on a subset of catalyst layers was performed using FIB-SEM (Figure SI 1). It is observed that Sample 9 has a much greater overall pore volume and larger sizes of pores than the other samples imaged. We suggest that the poor MEA performance of Sample 9 is due to one of two mechanisms: either poor solid phase connectivity hindering electron or proton transport, or a thicker catalyst layer increasing limitations for mass transport.

In the transition and transport-limited regions, Samples 2 and 9 continued to perform poorly, Sample 10 had mediocre performance, and Samples 14 and 8 exhibited the best performance. For the best two samples in this regime, the synthesis differs only in the type of leaching acid: HF/HNO₃ (Sample 8) vs. HF (Sample 14).

6.3.3 – XPS

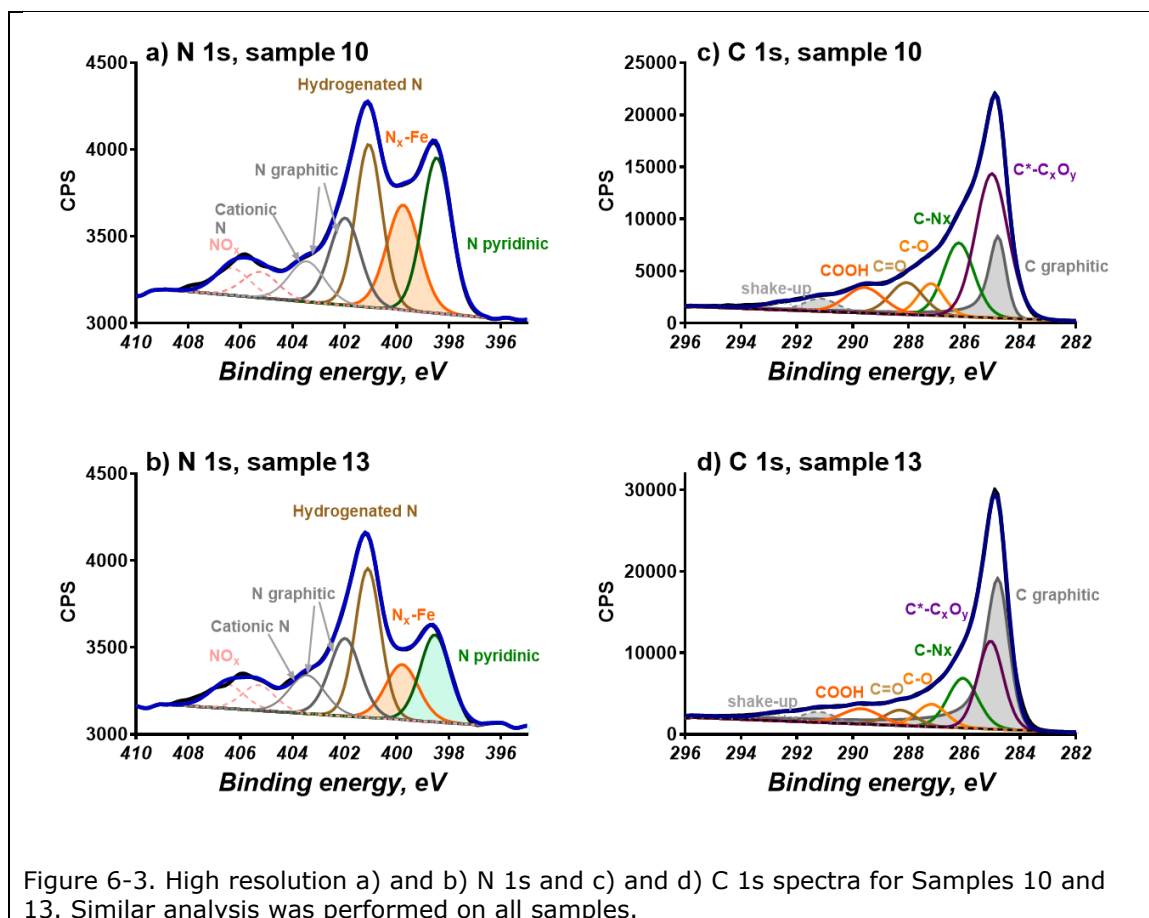
Catalyst surface composition was investigated using high-resolution XPS. Elemental composition as well as C and N speciation was determined for seven catalysts (Table 6-2). High resolution C 1s and N 1s spectra for two selected samples are presented in Figure 6-3 to illustrate differences in chemical composition. The catalysts consist of 88-92 at.% C, 4-9 at.% O, 2.8-4.0 at.% N and 0.1-0.2 at.% Fe, which are typical compositions for this

Table 6-2. XPS elemental composition, C 1s and N 1s speciation of catalyst powders.								
s.2 s.8 s.9 s.10 s.13 s.14 s.15	catalyst elemental composition, at. %							
	C	O	N	Fe				
	91.4	4.5	4.0	0.22				
	87.8	9.3	2.8	0.11				
	90.3	5.9	3.8	0.09				
	89.5	6.4	4.0	0.12				
	92.4	4.2	3.3	0.11				
	88.3	8.8	2.9	0.12				
	91.6	4.5	3.9	0.11				
	catalyst C speciation, rel. %				catalyst N speciation, rel. %			
C gr	C-N	C _x O _y	N pyrid	N _x - Fe	N hydrogenated	N gr/ N ⁺	NO _x	
s.2	38.0	15.2	40.4	24.9	13.0	21.8	17.5	22.5
s.8	8.2	27.9	60.7	22.9	18.8	18.8	18.3	20.4
s.9	27.5	17.5	49.3	23.2	16.5	21.6	17.6	20.8
s.10	9.5	15.2	69.3	24.5	19.8	22.5	15.5	17.7
s.13	35.4	16.1	42.6	18.0	13.9	25.9	19.4	22.7
s.14	22.2	25.5	49.1	22.2	17.4	24.6	18.0	17.9
s.15	27.2	16.4	50.7	22.3	17.5	22.7	16.7	20.8

class of materials.^{95, 104, 114} Samples 8 and 14 have both the highest amounts of O and smallest amounts of N detected. The highest concentration of Fe is observed for Sample 2 – an important confirmation that without proper milling prior to leaching, the material lacks morphology that facilitates efficient leaching of Fe-rich particles.

Figure 6-3 a) and b) show high resolution N 1s spectra fitted with multiple peaks of fixed width and shape as described in experimental section. The positions of peaks and corresponding chemical species that contribute to them have been discussed in thorough detail.^{95, 125} In summary, pyridinic N appears at 398.4 eV, N coordinated to Fe at 399.8 eV, pyrrolic or hydrogenated N at 401.4 eV, graphitic and cationic N at 402 and 403 eV and NO_x species at a highest binding energy between 405 and 407 eV. The

biggest difference in N composition is in relative amounts of pyridinic N, N coordinated with Fe, and pyrrolic/hydrogenated N species. Because the at.% of N depends on the amounts of other elements, and C, O, N, and Fe represent signal from different sampling depths, our analysis focuses on how the relative distribution of individual N types contribute to overall activity.⁹⁵



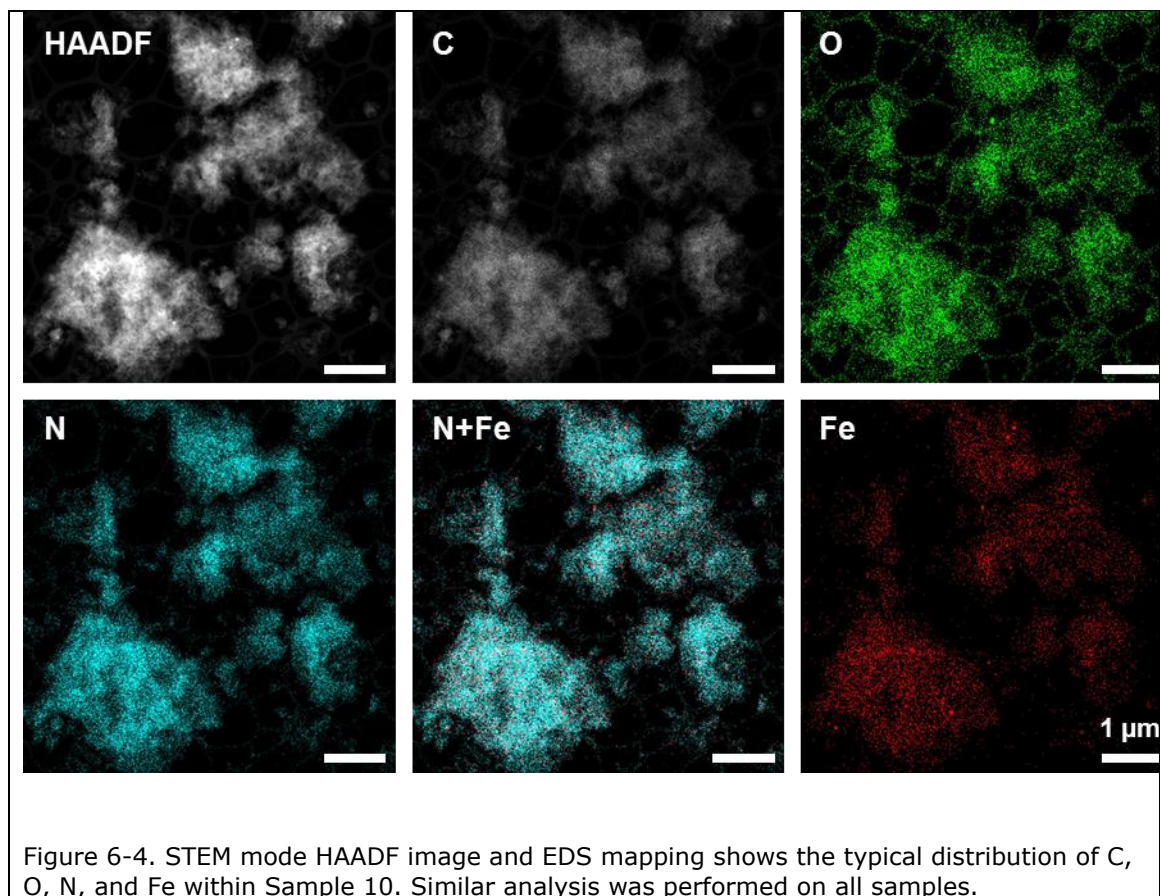
As clearly seen in Figure 6-3, Sample 10 has a larger contribution from peaks due to pyridinic N (24.5%) and N_x -Fe (19.8%) than Sample 13 with 18% and 13.9%, respectively. These species of N have been previously discussed by many as active sites for the ORR. Pyrrolic or hydrogenated N moieties, which have been reported to promote the partial reduction of oxygen to hydrogen peroxide, are largest for Samples 13 and 14.^{95, 131} For the same two samples,

high resolution C 1s spectra fitted with multiple peaks representing different types of C chemical environments are illustrated in Figure 6-3 c) & d).

Graphitic sp² C has been curve fitted by an asymmetrical peak at 284.4 eV due to excitation of low-energy electron-hole pairs, which then contribute to higher binding energy values. The peak at 285 eV has contribution from aliphatic C and from secondary carbons that are bonded to O groups – as discussed below. Nitrogen defects in the C network contribute to the peak at 286.2 eV. A series of peaks due to different C-O species (e.g. C-OH/C-OC, C=O, COOH) appears between 287 and 290 eV. The peak at 286.2 can also have a contribution from secondary carbons as above. Finally, between 291 and 293 eV two peaks due to π - π^* transition caused by the excitement of aromatic ring by exiting photoelectrons that contribute to shake-up peaks. We have combined peaks due to all surface oxides (peaks between 287 and 290 eV and peak at 285 eV) into one component C_xO_y (Table 6-2). The major C chemistries are the graphitic sp² network, C-N_x defects, and surface oxides C_xO_y. Previously, we have shown the importance of C_xO_y as a metric for the number of defects in the C network, which is correlated with formation of active sites and consequently with electrochemical activity.¹²⁷ From Table 6-2 it is seen that Samples 8 and 10 have the smallest relative amounts of graphitic C and largest concentrations of C_xO_y groups. Samples 8 and 14 have the highest amounts of C-N_x defects in C.

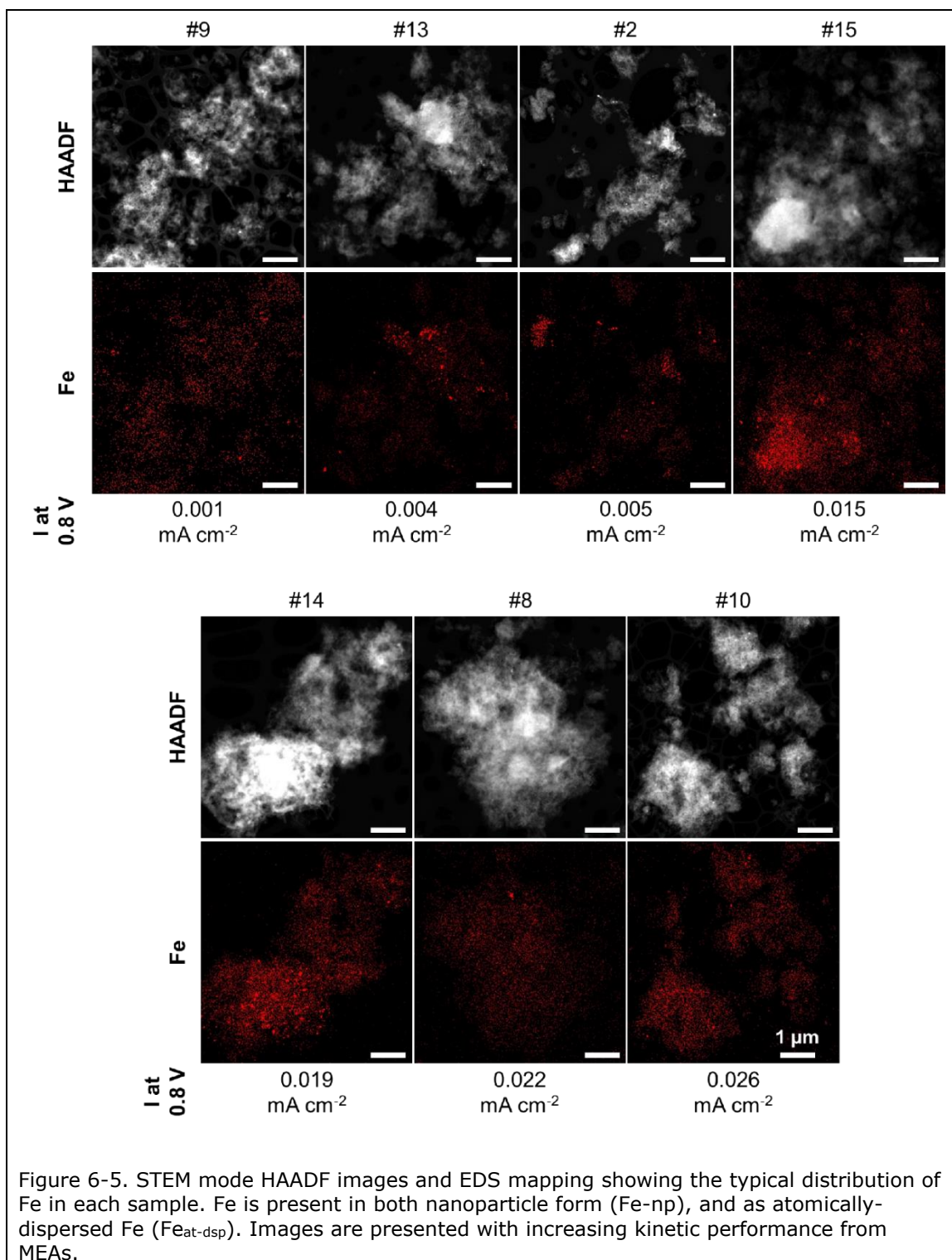
6.3.4 – TEM/EDS

STEM imaging and EDS mapping were used to determine elemental distribution across the materials, with a specific focus on N and Fe. Elemental maps of C, N, Fe, and O were generated for all samples, with representative maps displayed for Sample 10 (Figure 6-4). Each sample has a heterogeneous distribution of Fe, suggesting the presence of two types of Fe: Fe-rich nanoparticles (Fe-np) and atomically-dispersed Fe (Fe_{at-dsp}). High contrast particles that appear in high angle annular dark field (HAADF) imaging correspond to areas with high Fe concentration and do not correlate with any other elements (Figure SI 2). The more homogenously distributed



$\text{Fe}_{\text{at-dsp}}$ does correlate with C, O, and N. Composite maps of N and Fe show good correspondence between N and dispersed Fe in the material.

Higher magnification HAADF images and Fe elemental maps of particle-free areas (Figure SI 3) were preferentially selected for quantitative analysis to compare two important parameters from EDS: the content of $\text{Fe}_{\text{at-dsp}}$, and the ratio of total N to $\text{Fe}_{\text{at-dsp}}$. Elemental composition for each sample was quantified in multiple areas (as shown for Sample 10, Figure SI 4). The amount of $\text{Fe}_{\text{at-dsp}}$ and the ratios of $\text{N}/\text{Fe}_{\text{at-dsp}}$ were averaged across all areas for a given sample (Table SI 1). In mesomeric FeN_4 centers, portrayed by many as an ORR active site, the N/Fe ratio should be ~ 4 . Other types of disordered FeN_x centers may be present, which would result in a lower number of N per Fe, and thus smaller N/Fe ratios.^{56, 123} However, as indicated by XPS analysis, not all of the N present is coordinated to Fe. The EDS analysis yields N/Fe ratios significantly greater than 4, which is consistent with the XPS analysis results showing only a fraction of the total N is coordinated to Fe. The N/Fe ratio gives a measure of the amount of excess N in the material which can be viewed either as a measure of the efficiency of integrating N into active structures or, as discussed in the Analysis and Results section, a measure excess N affecting integration of the catalyst material with ionomer in electrodes.



The most general trend between the two EDS parameters is that the N/Fe_{at-dsp} ratio decreases as Fe_{at-dsp} increases, which is expected as the two parameters are interconnected.

6.4 – Analysis and Discussion

The presence of Fe-nps in the catalyst correlates with poor performance. Further, the presence of these particles does not necessarily indicate a higher total Fe content. Many Fe-nps were observed by STEM in Samples 13 and 15, but no increase in Fe content was measured by XPS and EDS. Consequently, samples with Fe-rich particles exhibited a lower concentration of dispersed Fe. It is clear that the materials with more uniform distributions of Fe show better electrochemical performance (Figure 6-5). The synthesis parameters that promote formation of these Fe-nps (and hinder formation of Fe_{at-dsp}) include incomplete leaching due to poor milling before acid treatment, and additional reduction during the second pyrolysis. This additional reduction results from either increased second pyrolysis time or use of a stronger reducing agent, i.e. H₂ as opposed to NH₃.

Electrochemical performance, as measured by E_{1/2} and MEA current at 0.8 V, correlates with the concentrations of N-Fe and C_xO_y measured by XPS, as well as with Fe_{at-dsp} measured by EDS (Figure 6-6) – consistent with prior work.^{49, 95, 118} Correlation between N-Fe and Fe_{at-dsp} (Figure 6-6 d) provides evidence that the quantitative information on the amount of N coordinated to Fe extracted from curve-fitting of high resolution N 1s XPS spectra, and the bulk material composition measured with EDS, are good representations of the material composition. Furthermore, the correlation of N-Fe and Fe_{at-dsp} with performance is consistent with the hypothesis that the active species in these catalysts involve FeN_x sites.

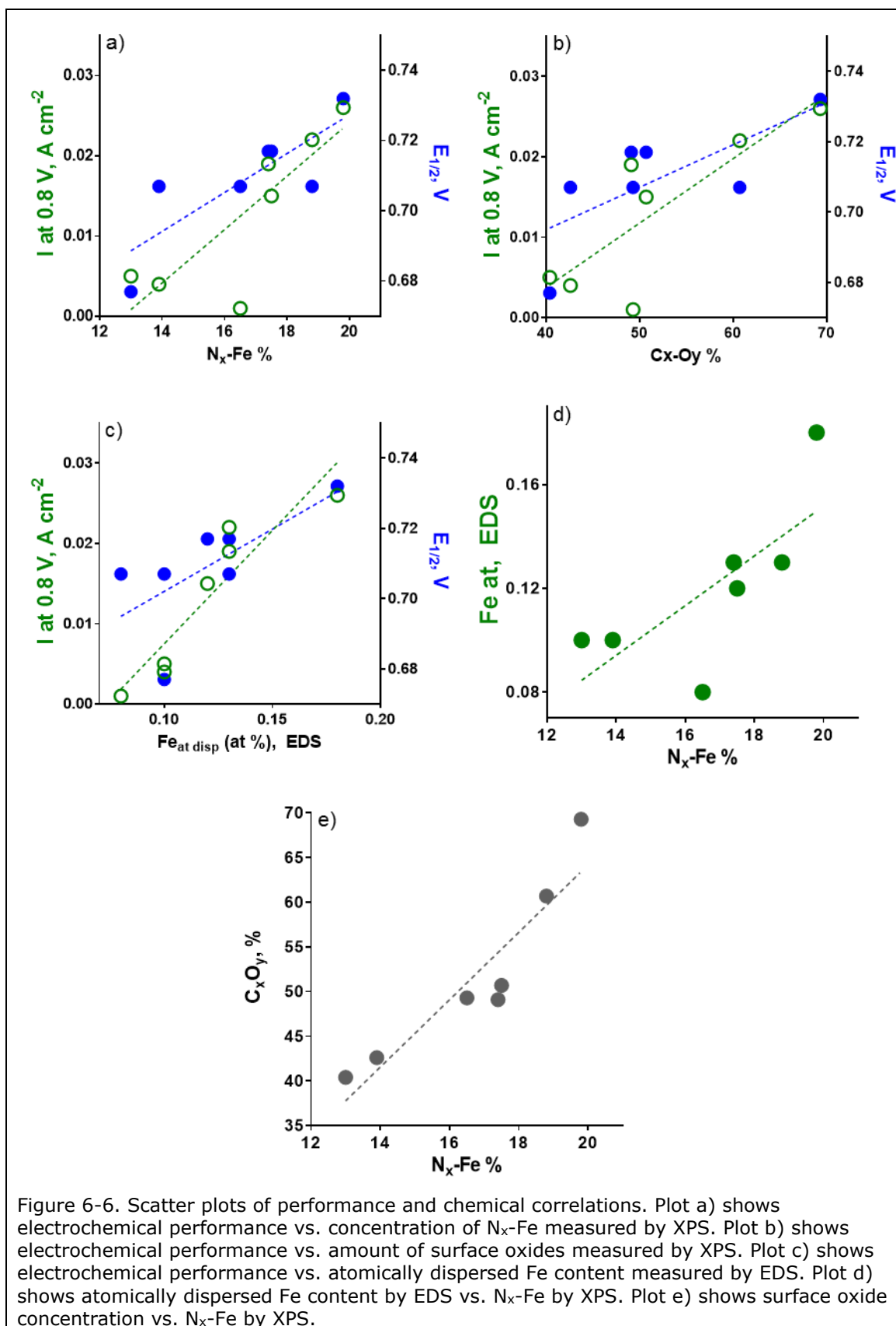
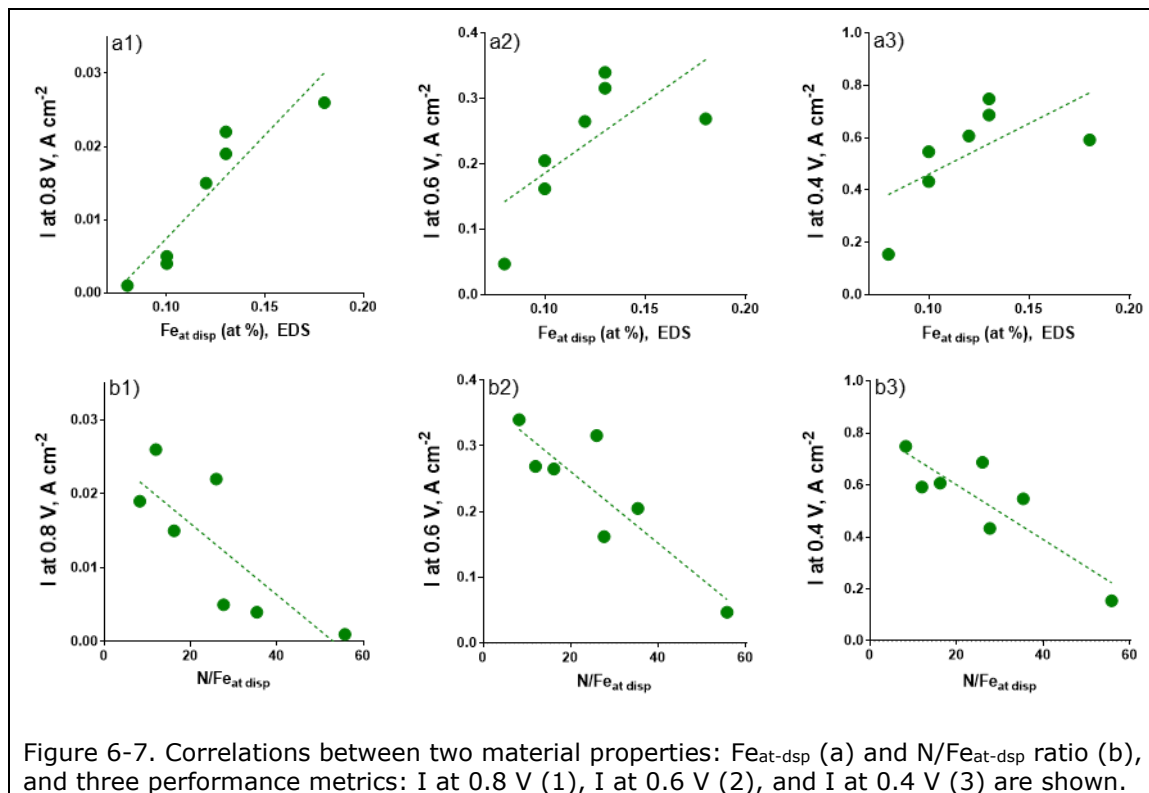


Figure 6-6. Scatter plots of performance and chemical correlations. Plot a) shows electrochemical performance vs. concentration of N_x-Fe measured by XPS. Plot b) shows electrochemical performance vs. amount of surface oxides measured by XPS. Plot c) shows electrochemical performance vs. atomically dispersed Fe content measured by EDS. Plot d) shows atomically dispersed Fe content by EDS vs. N_x-Fe by XPS. Plot e) shows surface oxide concentration vs. N_x-Fe by XPS.

Prior work reports that pyridinic N correlates with performance.^{95, 126} Here, it is observed that amount of N-Fe – rather than pyridinic N – is the better indicator of electrochemical performance in MEA and $E_{1/2}$. The linear trend between N-Fe and C_xO_y (Figure 6-6 e) indicates that increased active site concentrations correlate to an increased concentration of defects in graphitic structures, which commonly contain oxygen species. Synthesis parameters that influenced the amount of graphitic defects, and consequently surface oxide concentration, were the gas used during the second pyrolysis (H_2 reduced oxides), the acid used for leaching (HNO_3 promoted oxides), and incomplete leaching of Fe following the first pyrolysis reduced oxides. Surface oxides and hence defected graphitic structures can be directly influenced by altering synthesis parameters. Their strong correlation with N-Fe and activity provides a potential knob to influence the activity of these catalysts. Also, since reductive treatments following the first HT significantly affect both performance and the concentrations of C_xO_y and N-Fe, it appears that the active species are easily destroyed following the first pyrolysis and/or are largely formed during the second pyrolysis.

Performance in the transport region is best correlated with the N/Fe_{at-dsp} ratio (Figure 6-7). While catalysts with a high amount of Fe_{at-dsp} show the highest kinetic current, materials with a low N/Fe_{at-dsp} ratio have the highest transport current. This relationship is also present when considering the intermediate current range, but is less pronounced in the kinetic region. Lower N/Fe_{at-dsp} ratios suggest more coordination between Fe and N relative

to the total amount of N species and therefore a greater density of active sites – thus explaining the improved electrochemical performance.



Several samples deviate from these trends due to other compositional differences. Although Sample 10 shows the best performance in the kinetic region, it is expected to have an even higher kinetic current based on the amount of $\text{Fe}_{\text{at-dsp}}$. Despite having the highest amount of $\text{Fe}_{\text{at-dsp}}$ (that could be coordinated to N), the N-Fe percentage is lower and the $\text{N}/\text{Fe}_{\text{at-dsp}}$ ratio is higher than expected. This is likely due to the fact that Sample 10 was synthesized without CNTs, suggesting that N preferentially integrates with the pyrolyzed C matrix over CNTs. Sample 9 follows the chemical correlation trends well, but is an outlier in all MEA performance characteristics due to poor integration in the catalyst layer as discussed in the supplementary information.

6.5 – Conclusion

A set of PGM-free ORR electrocatalysts has been synthesized using the same precursor and with varying synthetic conditions. The materials were tested for catalytic performance in RDE and full MEA fuel cell operation, and characterized by XPS, STEM, and EDS. Analysis of the performance testing and physicochemical results yields several important correlations between synthesis, chemical composition, and performance. In this class of catalysts, the presence of Fe-nps is correlated with reduced $\text{Fe}_{\text{at-dsp}}$ in the material, leading to a decrease in electrochemical performance. Incomplete leaching and more aggressive reduction in the second pyrolysis both reduce $\text{Fe}_{\text{at-dsp}}$ and increase the occurrence of Fe-rich phases.

Electrochemical performance as measured by both RDE and MEA is strongly positively correlated with $\text{Fe}_{\text{at-dsp}}$, N-Fe, and C_xO_y . Furthermore, these chemical characteristics are related to each other, so direct synthetic control over any one of these parameters provides a means to tune catalyst performance. The number of defects in the C matrix, which promote formation of active sites and are manifested as higher amounts of C_xO_y , can be influenced during catalyst synthesis by minimizing the reductive conditions during the second pyrolysis, adding nitric acid during leaching, and ensuring complete leaching of excess Fe. The significant influence of treatments following the first pyrolysis indicates that the active sites are either fragile and easily destroyed before the second pyrolysis, or are primarily created during the second pyrolysis.

This work provides insight into synthetic methods that affect catalyst composition and performance. These insights can be used to improve PGM-free catalyst performance synthesized by a variety of techniques. Additionally, the strong correlations observed between $\text{Fe}_{\text{at-dsp}}$ and N-Fe species with ORR performance provide evidence that Fe coordinated with N function as active sites.

6.6 – Acknowledgements

We gratefully acknowledge support from the Center for Micro-Engineered Materials and NSF GRFP Grant No. 1418062. The authors deny any conflicts of interest related to this study.

Chapter 7 – Morphology, Chemistry, and Performance

7.1 – Introduction

Catalyst performance is dependent on both chemistry and morphology. In fact, chemistry and morphology are themselves interrelated. Traditional methods for analysis of catalyst morphology were discussed in Chapter 2, and new techniques for analysis of the catalyst surface and electrode internal morphology were presented in Chapters 4 & 5. In this section, additional characterization methods are utilized and correlations between morphology, chemistry, and performance are explored. The results presented in this chapter have not yet been published (except the subset included in Chapter 6). Portions of the work in this chapter will be submitted for publication. The coauthors for that publication will likely include Kateryna Artyushkova, Plamen Atanassov, Alexey Serov, Sam McKinney, Alex Mirabal, and Scott Calabrese-Barton. My contribution to this work included: Catalyst synthesis, RDE data acquisition and analysis, SEM data acquisition and analysis, MEA data acquisition and analysis, DWT analysis, BET acquisition and analysis, XRD analysis, data processing, correlation analysis, and interpretation of results.

7.2 – Experimental

The catalysts discussed in this chapter were prepared as described in Chapter 6. The catalysts used for the study in Chapter 6 include Samples 2, 8, 9, 10, 13, 14, and 15 from the full set discussed here. The synthesis

parameters of the full catalyst set are listed in Table 7-1. The methods for RDE, XPS, and MEA testing are the same as presented in Chapter 6.

<p>Table 7-1. Varied synthetic parameters. Parameters altered from the base process (Sample 8) are highlighted. All samples prepared as outlined in Chapter 6 except Sample 3, which was placed in a 900 °C oven for HT 1, and Sample 4, which was cooled at 25 °C min⁻¹ after HT 1 instead of being quenched. Samples 11 & 12 used LM-150D instead of LM-150.</p> <p>The columns are: LM-150 – amount (g) of LM-150 Stöber – amount (g) of 370 nm silica spheres CNT – amount (g) of CNT Fe(NO₃)₃ – amount of iron nitrate nonahydrate (g) Ball mill – ball mill used before etching Etch acid – which acid(s) used to etch silica and excess Fe Etch time – length of time sample was left in acid HT2 time – length of the 2nd pyrolysis HT2 gas – gas(es) used for the 2nd pyrolysis (NH₃ = 10%:90% NH₃:N₂, H₂ = 7%:93% H₂:N₂, gas for Sample 16 was changed half-way through HT2).</p>									
Sample	LM-150	Stöber	CNT	Fe(NO₃)₃	Ball mill	Etch acid	Etch time	HT2 time	HT2 gas
2	2.5	1.0	1.0	1.2	X	HF/HNO ₃	?	30 min	NH ₃
3	2.5	1.0	1.0	1.2	X	HF/HNO ₃	?	30 min	NH ₃
4	2.5	1.0	1.0	1.2	X	HF/HNO ₃	?	30 min	NH ₃
5	2.5	1.0	X	12.7	Yes	HF	5 days	45 min	H ₂
6	2.5	5.0	X	1.2	Yes	HF	5 days	45 min	H ₂
7	2.5	10.0	1.0	1.2	Yes	HF	5 days	45 min	H ₂
8	2.5	1.0	1.0	1.2	Yes	HF/HNO ₃	4 days	30 min	NH ₃
9	2.5	5.0	1.0	1.2	Yes	HF/HNO ₃	4 days	30 min	NH ₃
10	2.5	1.0	X	1.2	Yes	HF/HNO ₃	4 days	30 min	NH ₃
11	2.5 D	1.0	1.0	1.2	Yes	HF	4 days	30 min	NH ₃
12	2.5 D	1.0	1.0	1.2	Yes	HF/HNO ₃	4 days	45 min	NH ₃
13	2.5	1.0	1.0	1.2	Yes	HF/HNO ₃	4 days	45 min	H ₂
14	2.5	1.0	1.0	1.2	Yes	HF	4 days	30 min	NH ₃
15	2.5	1.0	1.0	1.2	Yes	HF/HNO ₃	4 days	45 min	NH ₃
16	2.5	1.0	X	1.2	Yes	HF	4 days	30 min	NH ₃ → Ar
17	2.5	1.0	X	1.2	Yes	HF	4 days	30 min	NH ₃

Catalyst surface area and pore size distributions were calculated by analysis of nitrogen adsorption isotherms. All samples were analyzed for surface area using Brunauer, Emmet, and Teller (BET) theory.²⁸ Samples were degassed at 120 °C for a minimum of 12 hours under flowing N. Isotherms were acquired on a Micrometrics Gemini system, and the surface area was calculated with multipoint BET. A subset of samples was also analyzed using a Micromeritics ASAP 2020 Nitrogen adsorption analyzer.

These samples were degassed at 200 °C for 12 hours under vacuum. The surface area was measured using the BET methodology. Pore size distributions were obtained from the isotherms using the Barrett-Joyner-Halenda (BJH)¹³² and Nonlocal Density Functional Theory (DFT)^{30, 133} approaches. BJH calculations were performed using the desorption branch of the isotherm, while DFT used the adsorption branch. Data smoothing was performed by the ASAP 2020 software for BJH and DFT analysis.

The crystalline structure of the catalysts was examined using x-ray diffraction (XRD). The diffraction patterns were acquired on a Rigaku SmartLab diffractometer equipped with a sealed-tube Cu source and a position-sensitive D/teX detector with a Ni filter to remove the Cu K β radiation component. Processing of the spectra was accomplished with the structure refinement program written by Shi, Reimers, and Dahn,⁴² which was updated to function on modern computer hardware by Lok-kun Tsui.¹³⁴

Catalyst surface analysis was accomplished by analysis of SEM images using texture analytics as described in work by Artyushkova, *et al.*¹³⁵ and the DWT as described in Chapter 4 with some modification.⁶⁴ Images were not acquired with identical brightness and contrast settings. To compensate for varying brightness, contrast, and intrinsic variations in how materials interact with the e⁻ beam, the roughness at each detail level and all roughness fits were normalized to the total roughness of the image. This normalization yields the relative fraction of roughness that occurs in each size range, independent of overall image contrast.

7.3 – Results and discussion

7.3.1 – Synthesis

The design parameters varied in the catalyst set are summarized in Table 7-1. Sample 1 was lost to a runaway exothermic reaction upon addition of HF. It should be noted that Samples 2-7 were handled by multiple people during the synthesis process. The acid etching, washing, and HT 1 were completed by different group members on different samples, so variations in performance, chemistry, and structure of these catalysts cannot necessarily be attributed to specific synthetic parameters.

Samples 8-17 were handled exclusively by me from beginning to end and all synthetic and process parameters were carefully controlled and documented.

Following the synthesis, the presence of residual metallic Fe was qualitatively screened for by use of a neodymium magnet (access to a Curie balance could not be secured). This was

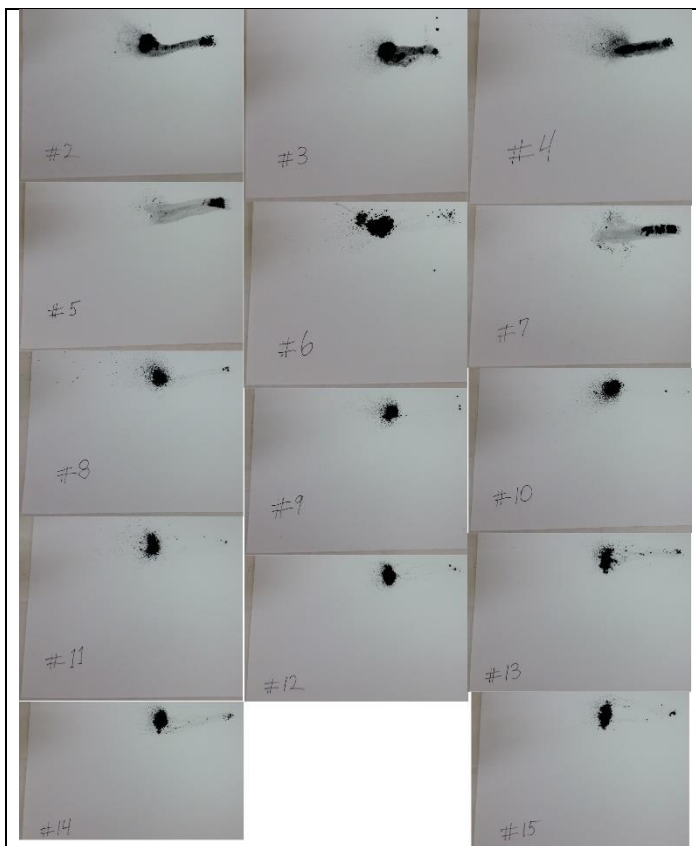


Figure 7-1. Images of magnet tests. Catalyst powder was placed on paper and a neodymium magnet was dragged from left to right in contact with the bottom of the paper.

accomplished by placing a small amount of catalyst powder on paper and dragging a neodymium magnet in contact with the bottom surface of the paper past the powder. The results of this test are shown in Figure 7-1. The behavior of the catalysts in the presence of the magnet can be divided into three categories: majority of powder interacting with magnet (high metallic Fe content), minority of powder interacting with magnet (medium metallic Fe content), and little/no interaction with magnet (low metallic Fe content). Samples 2-5 and 7 exhibited high magnetic interaction, Samples 6 and 13-15 medium interaction, and Samples 8-12 little interaction.

Sample 5 was synthesized with 10x the Fe as the rest of the samples. It is observed to be the worst performing catalyst in all performance testing metrics. As discussed in the introduction, there are two schools of thought on the active sites in PGM-free catalysts. Though specific values are not always present in the literature, it appears that those who believe Fe-rich phases (or graphitic structures modified by underlying Fe-rich particles) are the active species synthesize their catalysts using 10-50 wt.% Fe. Those who purposefully design catalysts to maximize Fe-N-C sites synthesize catalysts with ~1 wt.% Fe (as is the case with the materials in this study). As discussed in the introduction and supported in previous chapters, I believe the primary active species in MNC catalysts to be Fe coordinated with N in the C matrix. I also believe these are the active species present in the Fe-rich catalysts referenced by groups touting Fe-rich particles as the active species. In that class of materials, it appears those researchers have optimized the synthesis parameters to create Fe-N-C sites in addition to the Fe-rich phases.

However, since those materials have a predominance of Fe-rich phases over atomically dispersed Fe, measurement of the Fe-N-C active species becomes difficult/impossible as any signal from these moieties are drowned out by the Fe-rich phases. I address this here because I believe that Sample 5 is ostensibly an un-optimized version of an Fe-rich catalyst. As such, it exhibits significantly different composition and morphology and exists in a different structure-to-property space than the rest of the catalysts in this study.

7.3.2 – Isotherm analysis

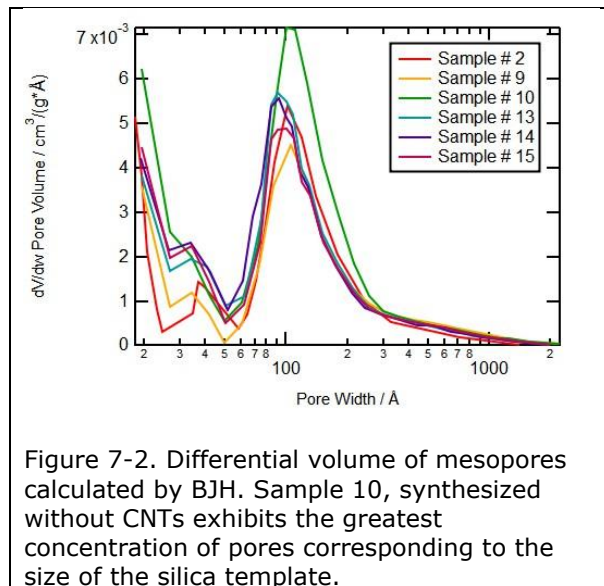
Surface area for all samples was calculated using the BET method. The surface area of all samples is shown in Table 7-2. The surface areas fall into two categories: those without CNTs in the range of 500-600 m² g⁻¹, and those with CNTs with area over 700 m² g⁻¹. This is likely because the CNT account for approximately 1/3 of the mass of the final catalyst and they have a surface area <100 m² g⁻¹.

A subset of the catalysts was selected for PSD analysis. Both BJH and DFT were applied and are applicable in different size ranges. The DFT analysis is useful for analysis of micropores, but is less accurate for mesopores. For these materials, BJH is expected to yield good results for mesopores.³¹ Figure 7-2 shows the BJH pore size distributions for all samples. It is observed that the mesopores distributions are similar for all samples with Sample 10 being

Table 7-2. Surface area measured using multipoint BET (m² g⁻¹)

Sample	Surface area
2	637
3	621
4	554
5	715
6	741
7	565
8	605
9	650
10	769
11	504
12	660
13	570
14	575
15	620

an outlier. Sample 10 was synthesized without CNTs and has the highest surface area of this subset, however, the increased area is due primarily to an increase in micropores, not mesopores. I believe the increased mesopore volume can also be attributed to the lack of CNTs.



Pores in this range are formed by the silica templates, OX50 and LM-150, which have primary particle sizes of 80-120 nm. During the impregnation phase of synthesis, the nicarbazin powder and dissolved iron nitrate are able to be in close contact with the silica templates. The CNTs are not able to tightly bend around templating agents of this size, so do not participate in formation of pores on this scale. Since, as mentioned above, the CNTs account for a significant mass percent of the final product, the mass-specific pore distribution will have a lower concentration of pores on this scale in the presence of CNTs.

Figures 7-3 a) and b) show comparisons of PSD by DFT and BJH for two samples in the mesopore region. They show similar mesopore volume, though the peak pore size is slightly shifted. The DFT model exhibits a flat region from 2-6 Å for Sample 10. This feature is present in 4 of the 6 samples analyzed. This blind-spot is common in DFT analysis and can result from mismatch between modeling parameters and the material properties, in

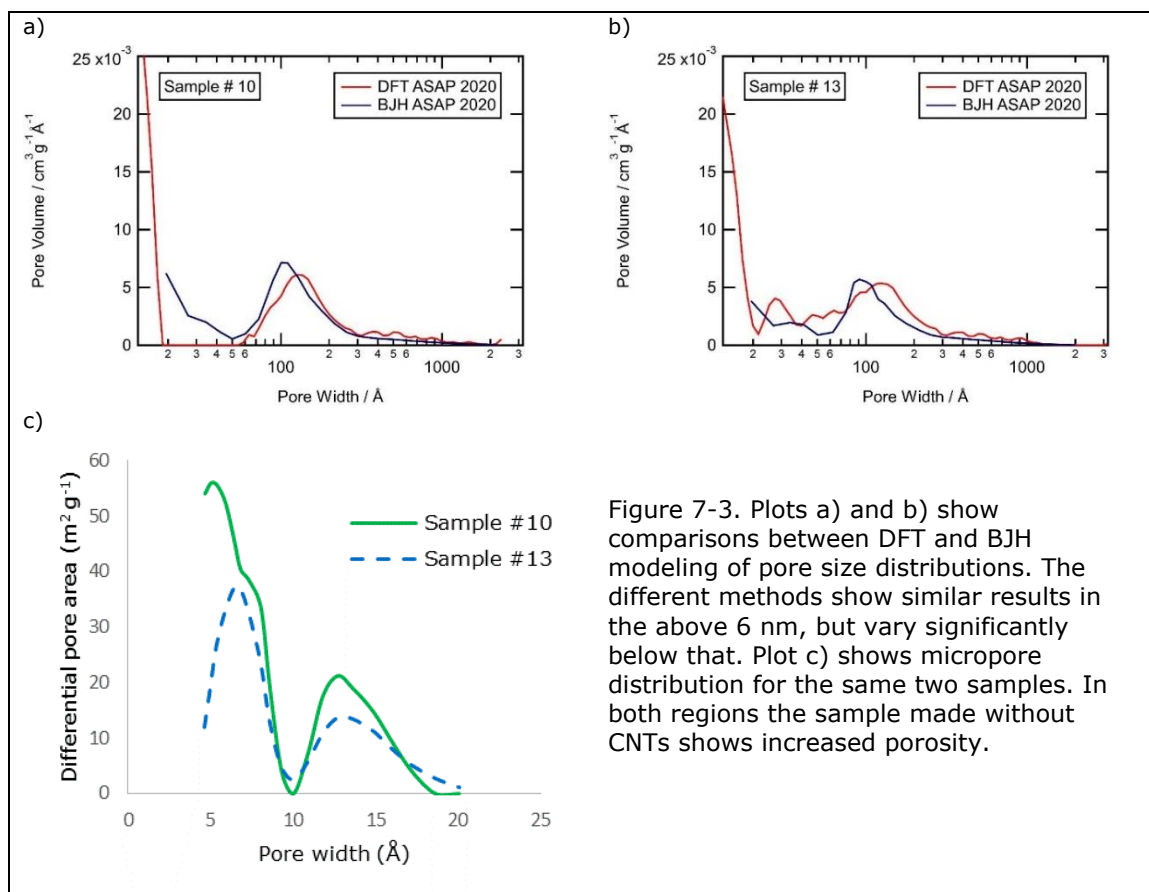


Figure 7-3. Plots a) and b) show comparisons between DFT and BJH modeling of pore size distributions. The different methods show similar results in the above 6 nm, but vary significantly below that. Plot c) shows micropore distribution for the same two samples. In both regions the sample made without CNTs shows increased porosity.

this case, likely heterogeneities in the material.^{136, 137} Figure 7-3 c) shows a comparison of the microporous region of two catalysts. Here it can be seen that Sample 10, synthesized without CNTs, has a significantly greater volume of micropores, contributing to its greater total surface area. The average pore width and micropore volumes are listed in Table 7-3.

Table 7-3. Results of pore size distribution analysis. Micropore volume calculated by DFT (cm³ g⁻¹). Average pore width calculated with BJH theory (Å).

Sample	Micropore volume	Average pore width
2	0.159	120
9	0.172	153
10	0.206	124
13	0.131	121
14	0.154	122
15	0.143	124

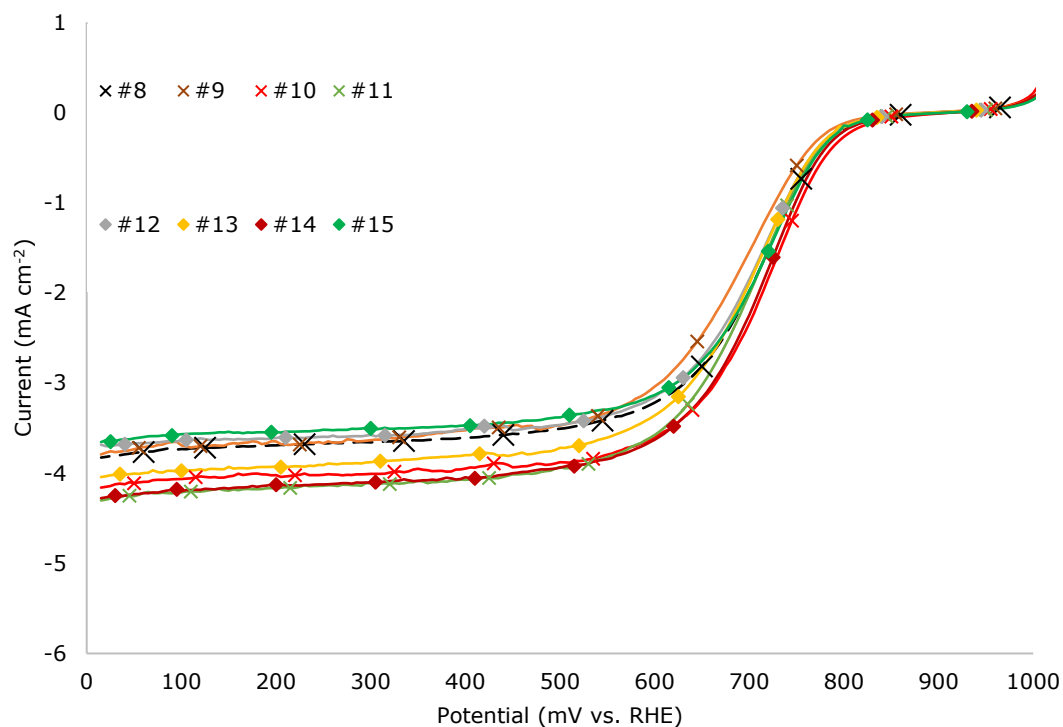
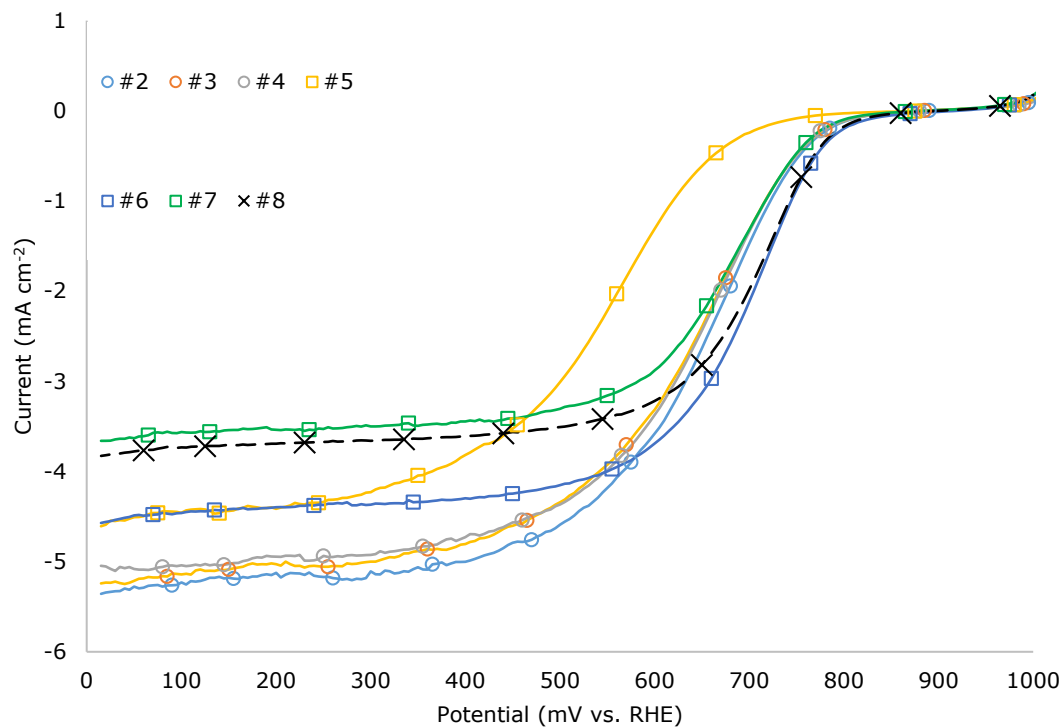


Figure 7-4. ORR polarization curves of Fe-NCB catalysts. RDE tests were performed in 0.5 M H₂SO₄ at 5 mV s⁻¹.

7.3.3 – Rotating disk electrode

Electrochemical activity was measured using the half-wave potential ($E_{1/2}$) from RDE data (Figure 7-4). The $E_{1/2}$ values range from 565 to 735 mV vs. RHE and are listed in Table 7-4. The sample with the highest $E_{1/2}$ is Sample 10, which was synthesized without CNTs. The worst performing sample was Sample 5, which was synthesized with 10x the standard amount of Fe. The second lowest $E_{1/2}$ is Sample 3 at 685 mV.

Table 7-4. Half-wave potentials measured by RDE (mV vs. RHE).

Sample	$E_{1/2}$
2	690
3	685
4	690
5	565
6	720
7	700
8	730
9	715
10	735
11	720
12	720
13	720
14	730
15	730

The worst performing samples by RDE all exhibited high magnetic interaction. As discussed in Chapter 6, catalysts with high metallic Fe content perform worse than samples with little/no metallic Fe. This trend is consistent through the full catalyst set.

7.3.4 – Membrane electrode assembly

Fuel cell performance was tested in a single cell MEA (Figure 7-5). There is a significant spread of performance in all operation regimes. Current values representative of the kinetic regime (0.8 V), transition region (0.6 V), and transport regime (0.4 V) as well as open-circuit voltage (OCV) are presented in Table 7-5. In general, samples with higher $E_{1/2}$ performed better in the kinetic region during fuel cell testing as seen in Figure 7-6.

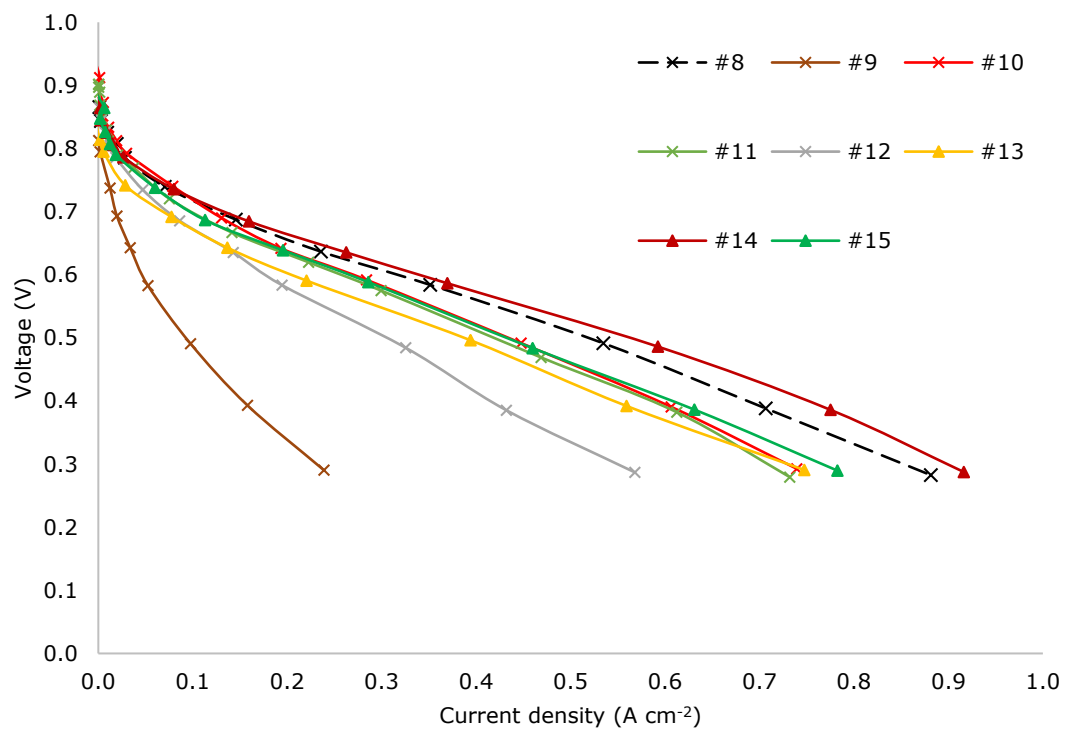
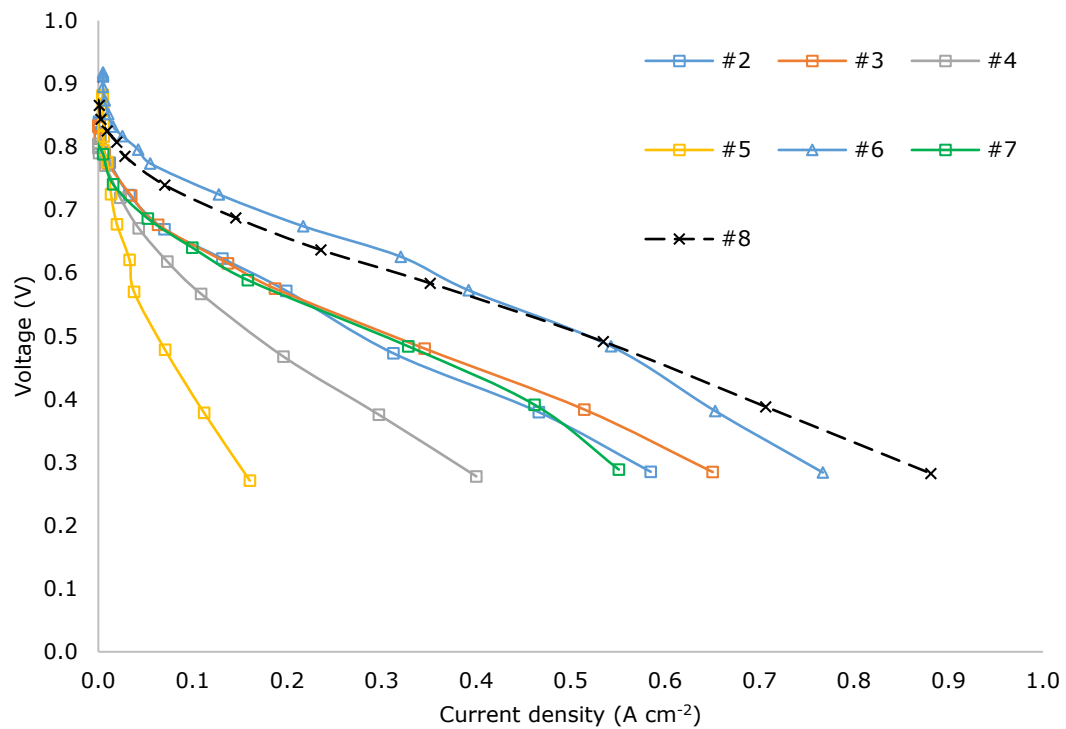


Figure 7-5. MEA polarization curves. Cell operated at 1.65 atm_{abs} with H₂/Air.

The samples exhibiting the best kinetic performance (Samples 6 and 10) were synthesized without CNTs. As discussed in Chapter 6, this is likely a result of active sites not forming on the CNTs. Aside from the two best performing samples being made without CNTs, and therefore having the highest surface area, there is no observed correlation between either total surface area or micropore volume with performance.

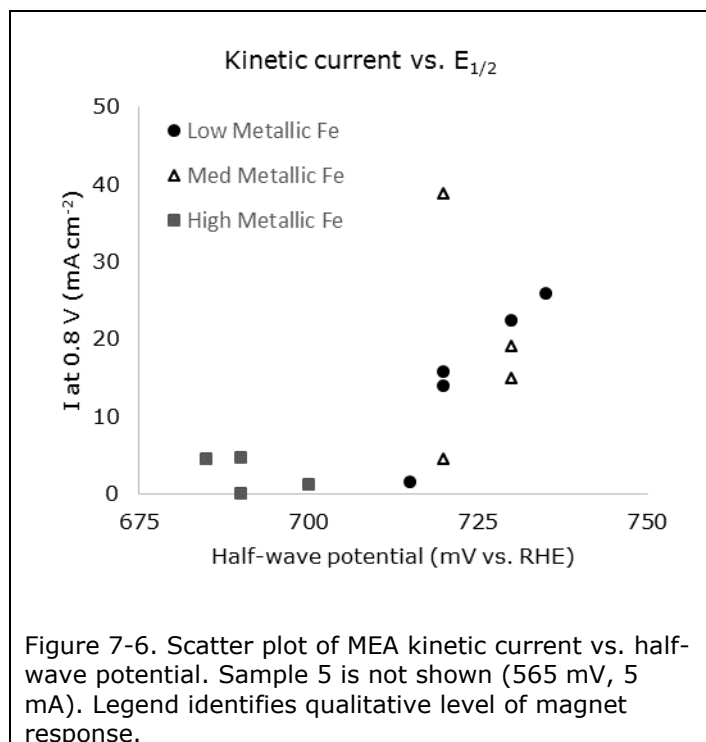
7.3.5 – X-ray diffraction

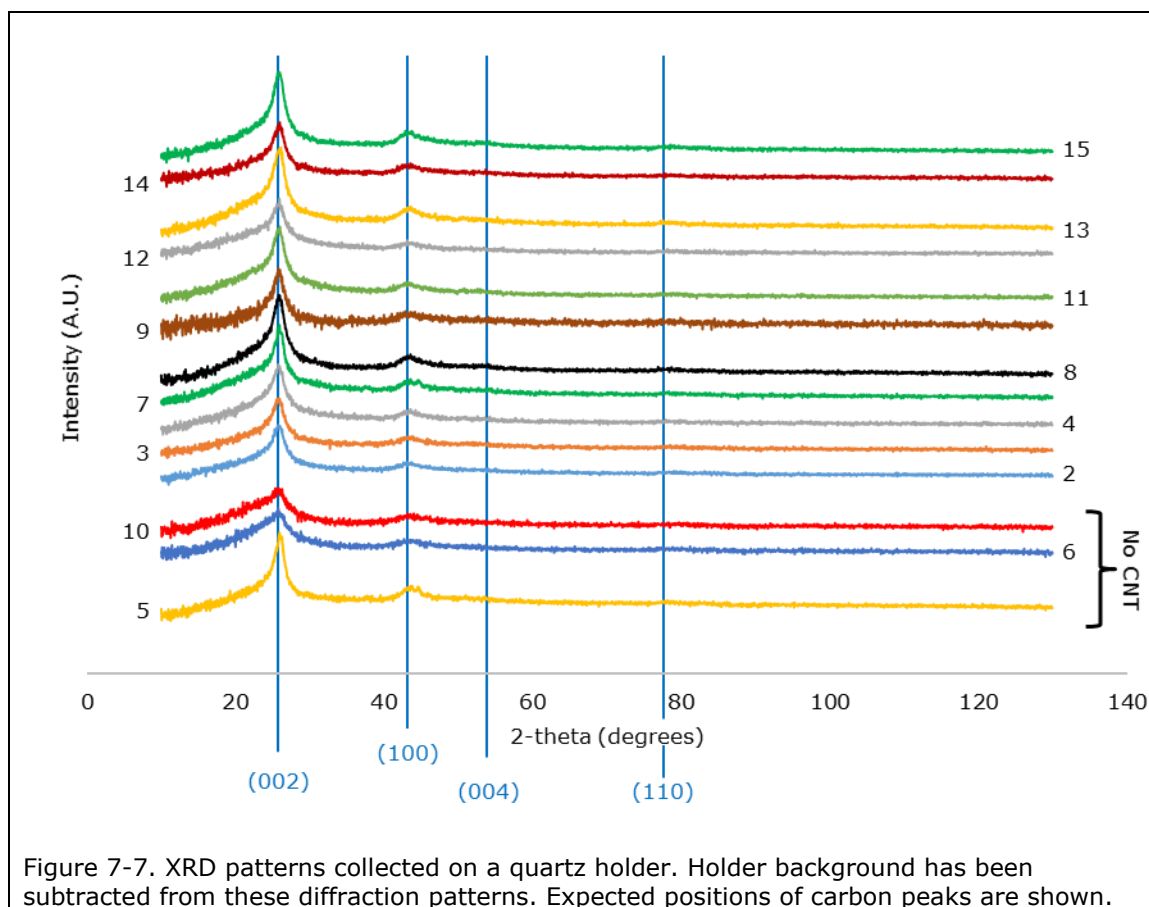
X-ray diffraction patterns were acquired for all samples. The spectra are shown in Figure 7-7. No Fe peaks are detectable in any of the patterns. This could be due to the low

concentration of metallic Fe and/or the small particle size. The samples synthesized without CNTs tend to have less pronounced diffraction peaks,

Table 7-5. MEA OCV (V) and current densities (mA cm^{-2}) at 0.8 V, 0.6 V, and 0.4 V. Testing performed at 12 psi back pressure (1.65 $\text{atm}_{\text{absolute}}$) in H_2/Air .

Sample	OCV	0.8 V	0.6 V	0.4 V
2	0.84	4.7	162	433
3	0.83	4.4	157	486
4	0.81	0.1	86	270
5	0.87	5.4	35	103
6	0.91	38.8	355	633
7	0.84	1.2	146	449
8	0.92	22.4	316	687
9	0.84	1.4	47	154
10	0.93	25.9	269	592
11	0.90	15.8	256	583
12	0.92	13.9	178	416
13	0.87	4.5	205	547
14	0.92	19.0	340	749
15	0.92	15.0	265	607





which is reasonable as the CNTs significantly affect the diffraction patterns.

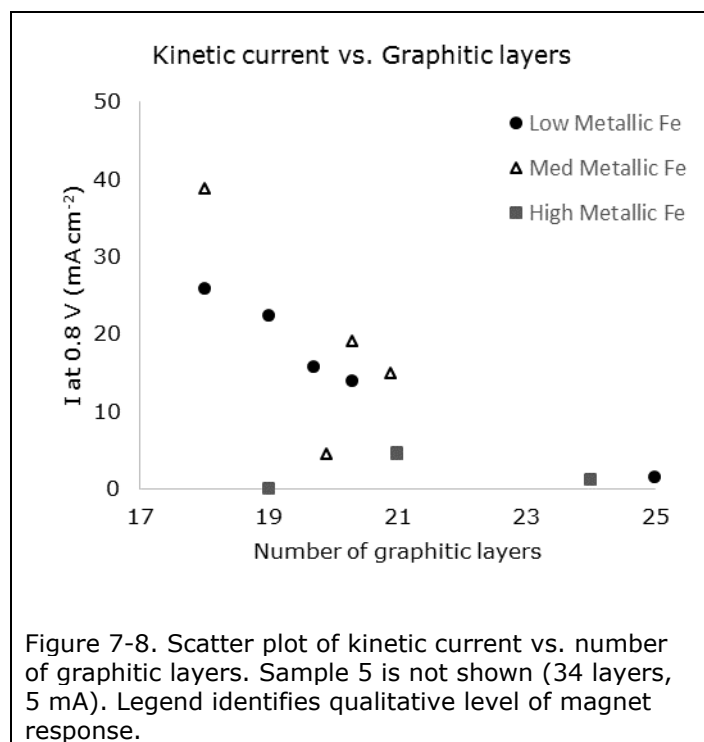
The exception to this is Sample 5, which shows the most defined carbon peaks of any sample. Fe is known to facilitate graphitization, and it appears that the metallic Fe in Sample 5 created a significant amount of graphitized carbon.

Examination of the C crystalline structure was performed using CarbonXS, a structure refinement for disordered carbon structures. The full details of the modeling theory can be seen in the original paper by Shi, *et al.*⁴² and the dissertation from which that manuscript was developed.¹³⁸ In summary, this refinement program fits XRD patterns based on 3-D modeling to account for the in-plane cell constant, interlayer spacing, crystallite

scattering coherence length, average number of layers, in-plane strain, through-plane strain, probability of random stacking, probability of 3R stacking, preferred orientation factor, and the Debye-Waller temperature factor. Of these modeling parameters, only the lateral coherence length, in-plane strain, and interlayer spacing were found to vary significantly between samples. This can be attributed to the similarity of the materials and/or limitations of the modeling program and the quality of the data. The calculated values for coherence

Table 7-6. Number of graphitic layers, in-plane strain (A.U.), and lateral coherence length (Å) measured by XRD.

Sample	# of Layers	Strain	Lateral size
2	21	0.033	123
3	21	0.034	124
4	19	0.027	166
5	34	0.030	96
6	18	0.035	222
7	24	0.028	170
8	19	0.025	83
9	25	0.049	239
10	18	0.048	248
11	20	0.027	107
12	20	0.034	119
13	20	0.030	110
14	20	0.031	124
15	21	0.029	82



length, in-plane strain, and number of layers are presented in Table 7-6. For all samples, the unit cell was 2.47 Å (except Sample 5) and the layer spacing

was 3.42 Å. The literature value for the unit cell in graphite is 2.46 Å. Sample 5 has a unit cell of 2.46 Å, supporting the conclusion that it has a higher level of graphitization.

The number of graphitic layers was found to correlate well with performance as shown in Figure 7-8. No correlation was observed with either the lateral size or in-plane strain. The presence of a strong correlation between the number of graphitic layers and performance, coupled with a lack of similar correlation with lateral crystallite size, gives some insight into the likely location of active sites in the graphitic structures. If the active sites were predominantly edge defects, I would expect a correlation between lateral crystallite size and performance. For active sites existing primarily as in-plane defects, materials with fewer graphitic layers will have increased exposed graphitic planes and thus increased performance. As the latter is observed, I believe it is likely that the primary active sites in this class of PGM-free catalysts consist of in-plane defects.

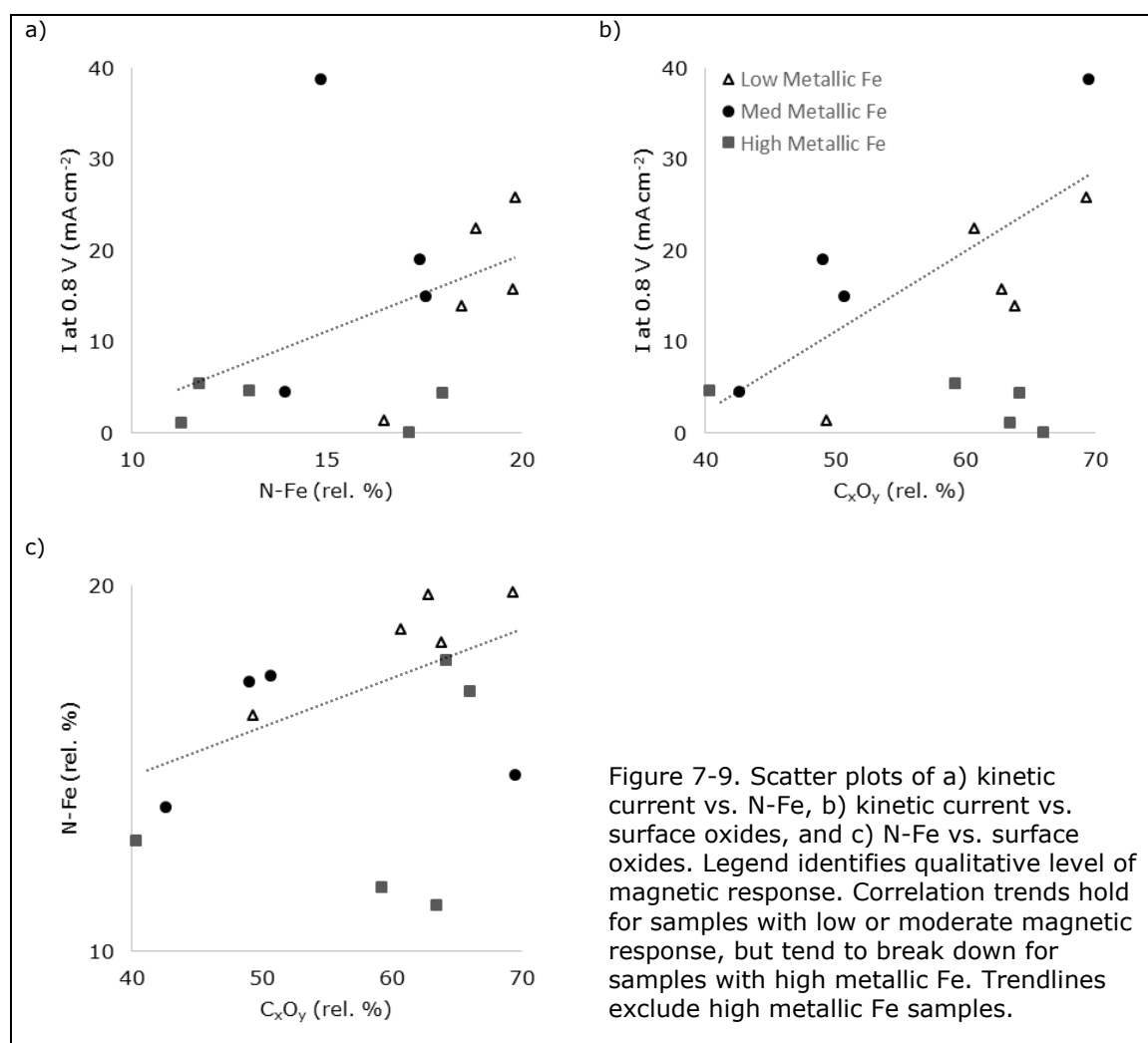
7.3.6 – X-ray photoelectron spectroscopy

The XPS methodology and results for Samples 2, 8, 9, 10, 13, 14, and 15 have been discussed in detail in Chapter 6. Here that discussion will be extended to the full catalyst set and additional insights explored. XPS results are shown in Table 7-7. As above, Samples 8 and 14 have among the highest amounts of O and smallest amounts of N. In the full set, Sample 7 has the highest amount of O and Samples 7 and 5 have the lowest N content, both extrema significantly outside the range of the subset.

Table 7-7. XPS elemental composition, C 1s and N 1s speciation of catalyst powders.								
	Catalyst elemental composition, at. %							
	C	O	N	Fe				
s.2	91.4	4.5	4.0	0.22				
s.3	91.6	3.8	4.5	0.18				
s.4	90.5	5.6	3.8	0.23				
s.5	92.2	6.2	1.5	0.10				
s.6	90.2	6.7	3.0	0.07				
s.7	87.5	10.9	1.6	0.09				
s.8	87.8	9.3	2.8	0.11				
s.9	90.3	5.9	3.8	0.09				
s.10	89.5	6.4	4.0	0.12				
s.11	88.5	8.2	3.3	0.14				
s.12	88.7	8.4	2.9	0.11				
s.13	92.4	4.2	3.3	0.11				
s.14	88.3	8.8	2.9	0.12				
s.15	91.6	4.5	3.9	0.11				
	catalyst C speciation, rel. %			catalyst N speciation, rel. %				
	C gr	C-N	C _x O _y	N pyrid	N _x -Fe	N hydrogenated	N gr/ N ⁺	NO _x
s.2	38.0	15.2	40.4	24.9	13.0	21.8	17.5	22.5
s.3	16.3	12.9	64.2	24.6	18.0	20.7	16.9	20.0
s.4	12.7	14.2	66.1	23.3	17.1	25.8	14.0	19.9
s.5	17.4	19.5	59.2	12.6	11.7	32.6	21.2	29.4
s.6	6.6	20.0	69.5	17.1	14.8	33.7	16.5	23.7
s.7	12.5	21.7	63.5	16.1	11.3	26.8	22.2	21.6
s.8	8.2	27.9	60.7	22.9	18.8	18.8	18.3	20.4
s.9	27.5	17.5	49.3	23.2	16.5	21.6	17.6	20.8
s.10	9.5	15.2	69.3	24.5	19.8	22.5	15.5	17.7
s.11	11.8	21.4	62.8	23.3	19.8	21.9	16.1	18.9
s.12	11.2	21.0	63.8	23.3	18.4	24.0	14.9	19.3
s.13	35.4	16.1	42.6	18.0	13.9	25.9	19.4	22.7
s.14	22.2	25.5	49.1	22.2	17.4	24.6	18.0	17.9
s.15	27.2	16.4	50.7	22.3	17.5	22.7	16.7	20.8

Correlations explored in Chapter 6 included relationships between kinetic MEA current, N-Fe, and C_xO_y. Plots of these relationships for the full set are shown in Figure 7-9. The same general trends are observed: kinetic performance increases with increasing N-Fe concentration, kinetic performance increases with increasing C_xO_y, and concentrations of N-Fe and

C_xO_y are positively correlated. These relationships hold for samples with low or moderate magnetic response but tend to break down for samples with high metallic Fe content. This is consistent with prior observations that metallic Fe hinders catalyst performance and supports the hypothesis that high-Fe content catalysts are a different class of materials that exist in a different structure-to-property space.



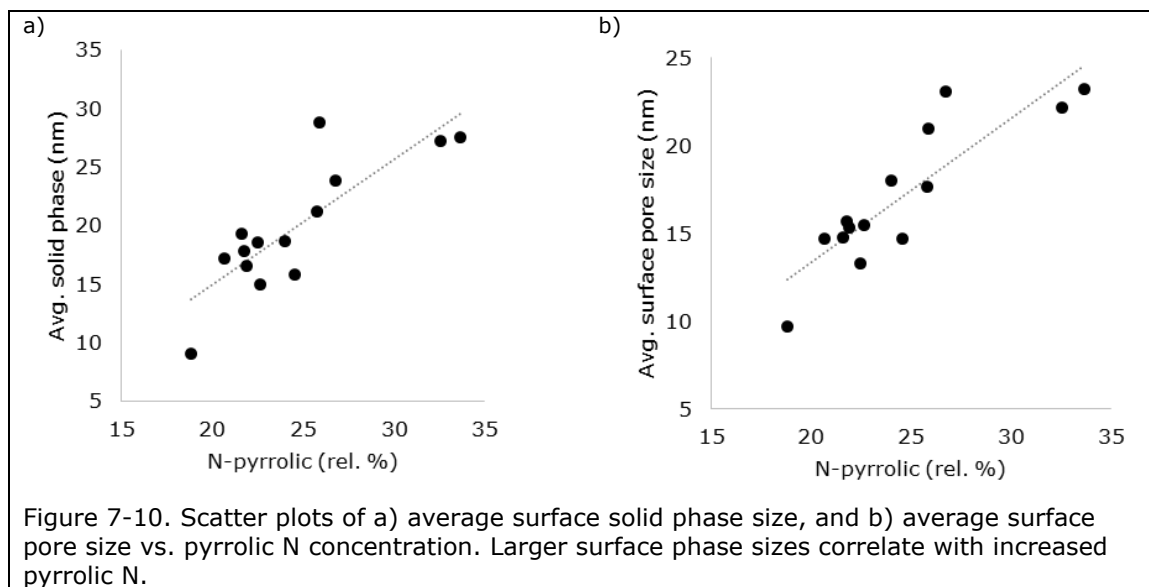
7.3.7 – Scanning electron microscopy surface analysis

Catalyst surface was imaged by SEM and analyzed using a variety of metrics.^{38, 64, 135} Texture parameters were calculated including:

- Average run length – the average consecutive number of pixels in either the solid phase or pores. This is a measure of the average size of the solid phase and pores at the catalyst surface.
- Euler number – a measure of the connectivity of either the solid phase or pores. A lower Euler number represents a more connected phase.
- Correlation – a measure of the linear dependency of neighboring pixels. Repeating patterns increase correlation.
- Entropy – a measure of randomness in an image. Complex textures and highly heterogeneous images have high entropy.
- Uniformity – a measure of homogeneity or orderliness of an image. Frequently repeated patterns or highly random features decrease uniformity while large contiguous domains increase uniformity.

These texture parameters do not require imaging with the same brightness and contrast settings as they are not influenced by these factors. However, it is necessary that the images be acquired on the same instrument as the way the micrographs are rendered can have a significant effect on the values. All samples were imaged on the same instrument, however, the SEM was moved from one location to another, recalibrated, and had hardware replaced after imaging of Sample 8 but before imaging of the rest of the samples. As a result, the texture parameters for Sample 8 are quite different

from the rest of the catalyst set. The length-scale specific parameters based on the normalized DWT were not similarly affected.



Analysis of the texture parameters yields several correlations. As the average pore and solid domain sizes in SEM images increase, the relative amount of pyrrolic N also increases (Figure 7-10). Conversely, relative concentrations of N-Fe and pyridinic N decrease (Figure 7-11 a & b). So, beneficial chemical species correlate with smaller pore and solid domains. The Euler number is also positively correlated with N-Fe and pyridinic N (Figure 7-11 c & d). As the Euler number decreases, phases are more connected, indicating that smaller, less connected solid and pore surface phases correlate with beneficial chemistries. Both grayscale correlation (the measure of repeated patterns), and uniformity are negatively correlated with N-Fe and pyridinic N (Figure 7-11 e & f). This means that materials with smaller, less connected phases, that exhibit higher degrees of heterogeneity are correlated with positive chemistries. Extending these image analyses to

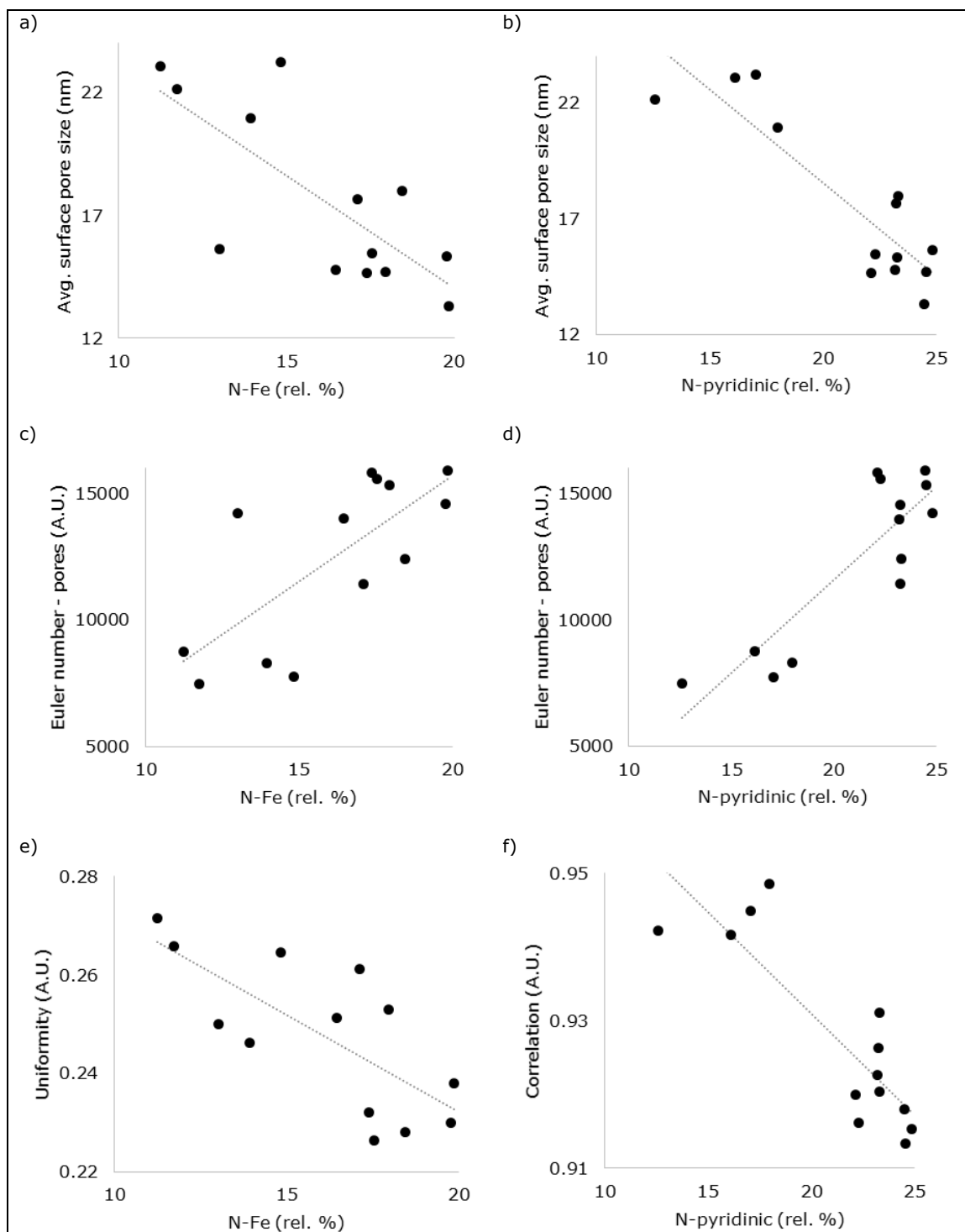
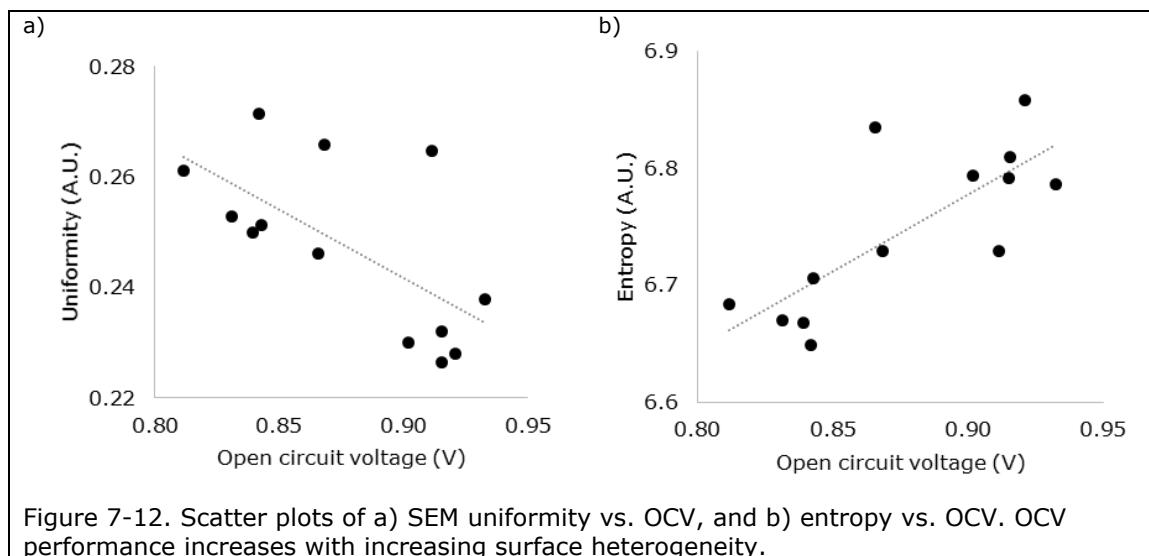


Figure 7-11. Scatter plots of relationships between catalyst composition and surface analysis parameters. Left plots show relationships between N-Fe and a) average surface pore size, c) Euler number (connectivity), and e) uniformity. Right plots show relationships between pyridinic N and b) average surface pore size, d) Euler number, and f) grayscale correlation. Sample 8 is not shown. Its values are: a) (18.8, 9.7) – b) (22.9, 9.7) – c) (18.8, 30887) – d) (22.9, 30887) – e) (18.8, 0.151) – f) (22.9, 0.87)

performance characteristics, it is observed that the image uniformity is negatively correlated with OCV while image entropy is positively correlated (Figure 7-12). Further, N-Fe and pyridinic N are correlated with performance (Figures 6-6 & 7-9).



Size-specific analysis of surface features was performed using the DWT. The fraction of surface roughness from 2-21 nm is seen to negatively correlate with pyrrolic N content (Figure 7-13 a), which is consistent with the surface domain size analysis presented above. However, no correlation is observed between pyridinic N and roughness from 2-21 nm, as illustrated in Figure 7-13 b). It is seen that correlations between pyridinic N and N-Fe are specifically confined to the 8 nm size range (Figure 7-13 c & d), which is consistent with my previous DWT analysis of these chemistries (Chapter 4 and work by Rojas-Carbonell, *et al.*).^{64, 65} Catalyst kinetic performance also positively correlates with roughness from 2-21 nm (Figure 7-13 e).

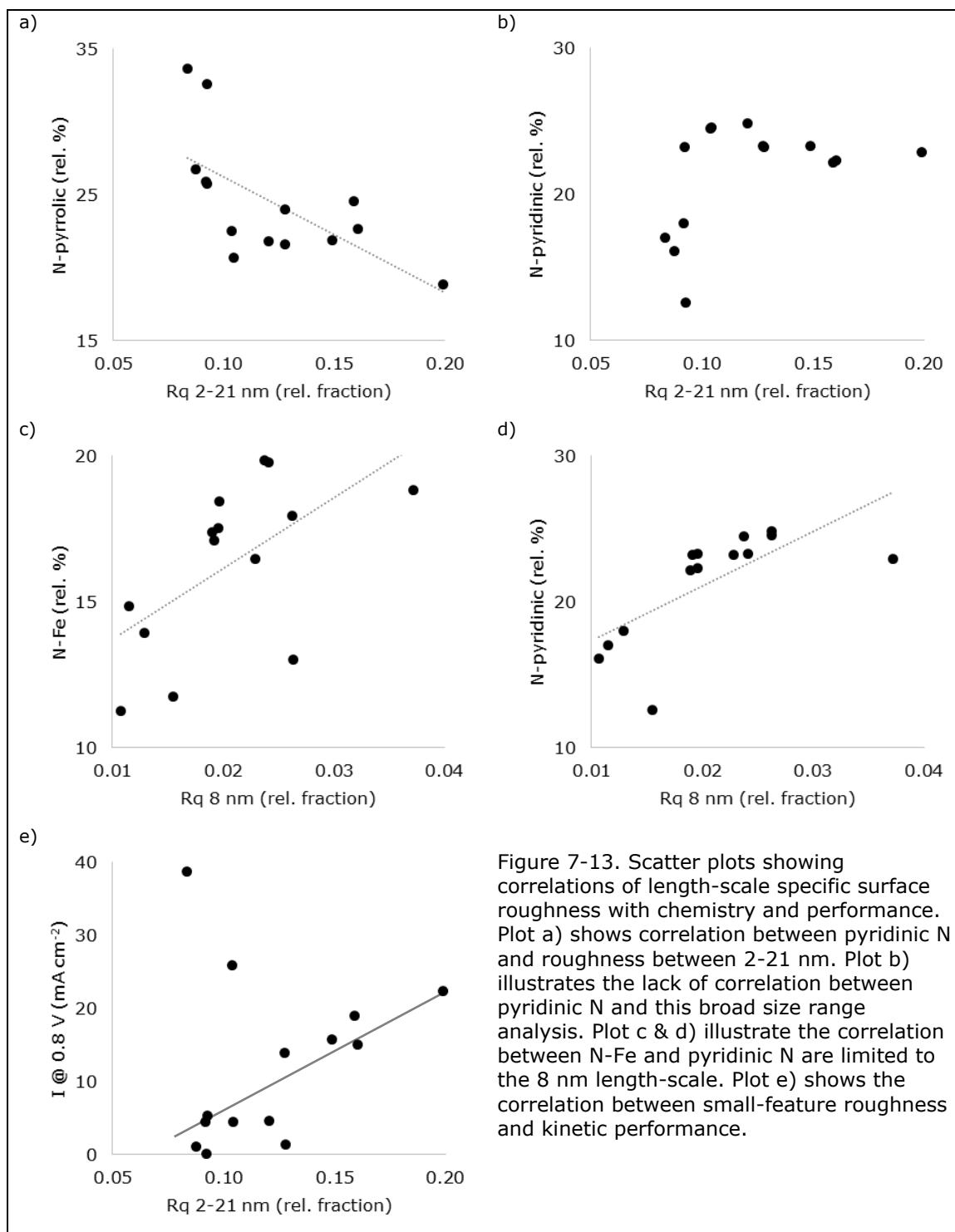


Figure 7-13. Scatter plots showing correlations of length-scale specific surface roughness with chemistry and performance. Plot a) shows correlation between pyridinic N and roughness between 2-21 nm. Plot b) illustrates the lack of correlation between pyridinic N and this broad size range analysis. Plot c & d) illustrate the correlation between N-Fe and pyridinic N are limited to the 8 nm length-scale. Plot e) shows the correlation between small-feature roughness and kinetic performance.

7.4 – Conclusion

Chapter 6 examined relationships between synthesis, chemistry, nanostructure, and performance on a subset of catalysts. Here the full catalyst set is examined and relationships between morphology, chemistry, and performance are explored. The analysis techniques include chemical analysis by XPS, qualitative testing for metallic Fe by magnetic attraction, morphology characterization by XRD and isotherm analysis, surface characterization by analysis of SEM images, and performance testing by RDE and MEA.

Several structure – chemistry – performance relationships are elucidated. Catalysts exhibiting high magnetic affinity due to the presence of metallic Fe have the lowest performance, even in the presence of traditionally beneficial chemistries such as pyridinic N and surface oxides. The presence of CNTs decreases the micropore, mesopore, and total surface area. They also reduce the available material in which active sites can form, limiting kinetic performance in RDE and MEA. Beneficial chemistries and catalyst performance are positively correlated with small, heterogeneous surface phases. A greater density of small surface features correlates with performance, and a greater density of surface features around 8 nm correlates with pyridinic N and N-Fe. Finally, catalyst performance improves with fewer graphitic layers. As no similar correlation is observed between performance and lateral crystallite size, this provides evidence that the active species in this class of catalysts may exist predominantly within the graphitic plane as opposed to edge defects.

Chapter 8 – Application of Structure to Property Predictions

8.1 – Introduction

In the previous chapters, I have discussed analysis of catalyst structure, chemistry, and performance. The goal of structure-to-property analysis is ultimately property prediction and improved rational design of catalysts. In this chapter, I discuss synthesis of new catalysts based on the results of my prior work. Their performance is reported and consistency with prior structure-to-property relationships is explored.

8.2 – Experimental

The synthesis parameters for Samples 16 & 17 are shown in Table 7-1. They were synthesized as discussed in Chapter 6. One batch of double the standard amount was prepared and split in half before the 2nd pyrolysis. As this was a single batch from precursor mixing through etching, variation between the samples results only from the 2nd pyrolysis.

Catalysts were characterized by XRD, XPS, RDE, and MEA as described previously. The parameters of MEA testing are the same as previously discussed, but a different cell and test station were used. Samples 2-15 underwent MEA testing at Pajarito Powder, LLC. Though the Pajarito Powder and UNM test cells are both 5 cm² with single serpentine pattern graphite flow plates, performance results for identically prepared MEAs yield different results, especially in the transport region. This is possibly due to differences in the width/depth of the flow channels. For accurate comparison, Samples

16 & 17 are compared with results for Samples 8, 10, & 14 that were tested on the UNM station and cell.

8.3 – Results and discussion

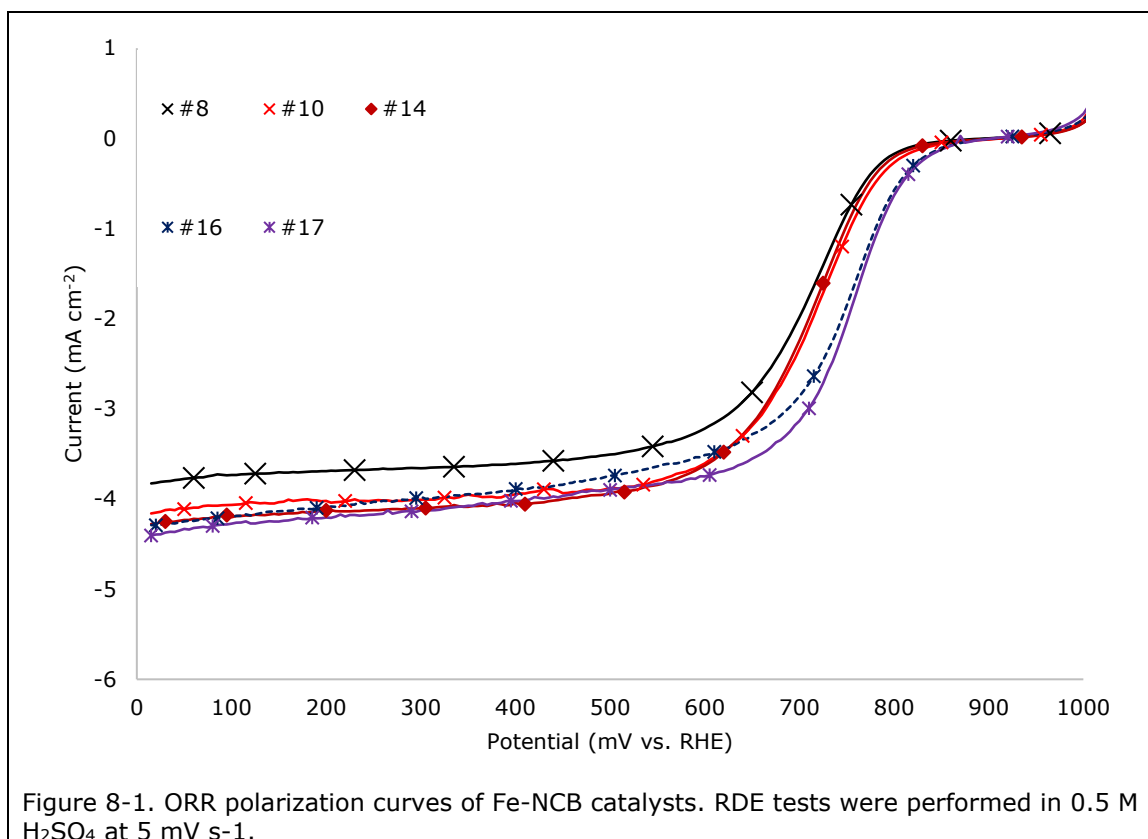
8.3.1 – Synthesis

The design parameters for Samples 16 & 17 were chosen based on results of previous analyses:

- No CNTs – Samples without CNTs exhibited better kinetic performance as CNTs do not host active sites.
- Ball mill for 60 minutes before etching – Samples without ball milling before etching had higher metallic Fe. Ball mill time increased from 10 to 60 minutes to promote most efficient etching.
- Etch in HF – Sample 14, which differed from Sample 8 only in etching acid, exhibited the best transport characteristics.
- HT 2 in NH_3 – Samples pyrolyzed in H_2 exhibited reduced performance from reduced oxides and increased metallic Fe.
- Change gas from NH_3 to Ar half-way through HT 2 (Sample 16 only) – Surface oxides correlate with active site formation and 2nd pyrolysis had a significant effect on surface oxides.

8.3.2 – Rotating disk electrode

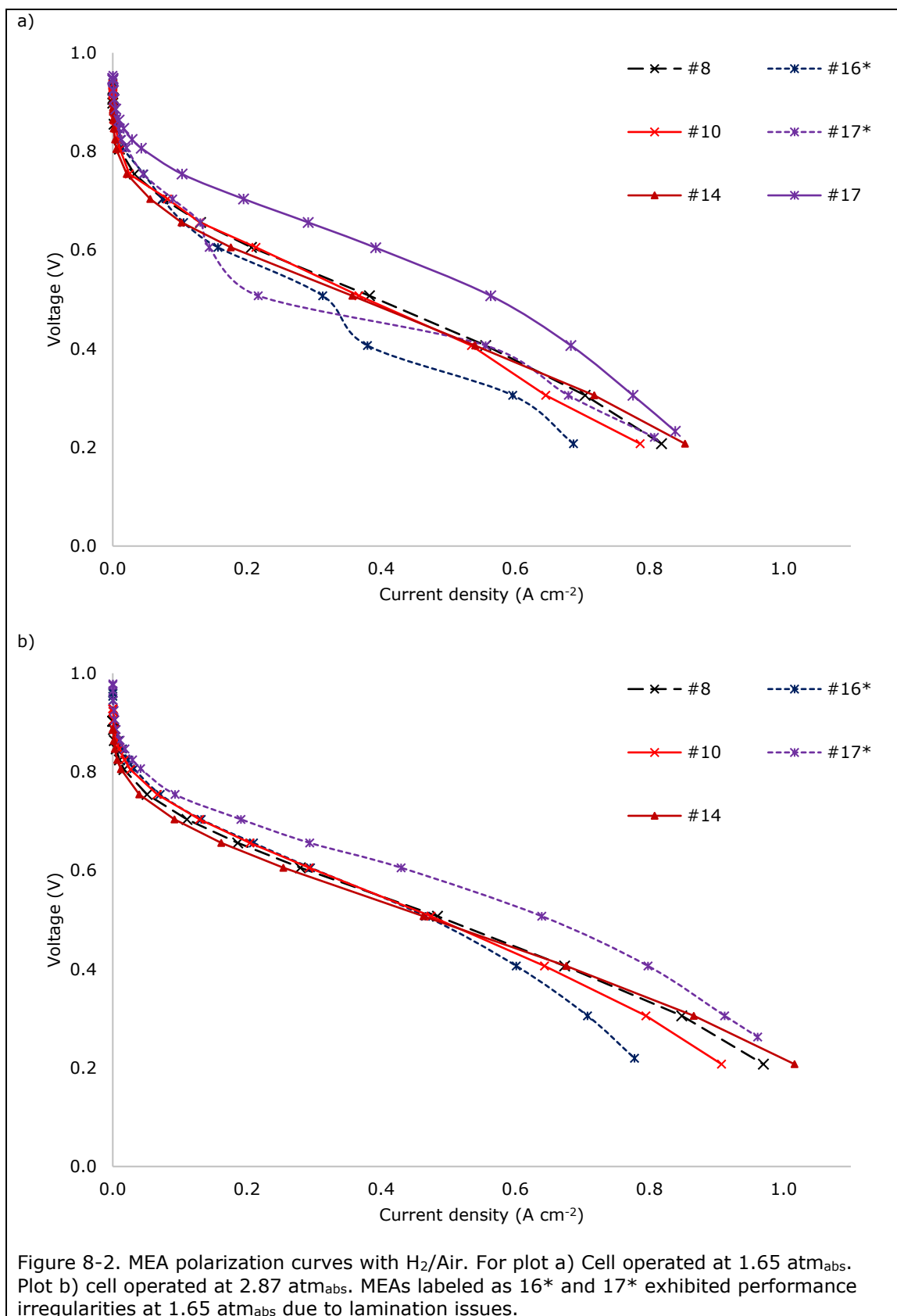
Electrochemical characterization by RDE was performed. Polarization curves are shown in Figure 8-1. Curves for Sample 8 (baseline recipe) Sample 10 (best kinetic performance), and Sample 14 (best transport



performance) are included for comparison. Samples 16 & 17 both have $E_{1/2}$ of 765 mV vs. RHE, which is 30 mV better than the next best catalyst in this set.

8.3.3 – Membrane electrode assembly

Fuel cell performance was tested in a single cell MEA (Figure 8-2). Of the 3 MEAs tested (one for Sample 16, two for Sample 17), two showed significant lamination issues. These polarization curves, labeled 16* and 17*, had unexpected dips in current with decreasing potential during the 12 psig (1.65 atm_{abs}) runs. The baseline high-frequency resistance for these MEAs was ~20% higher than the other MEAs and at some points spiked to 2x higher. Operation at 30 psig (2.87 atm_{abs}) did not exhibit these issues.



Polarization curves at both operating pressures are shown to allow for direct comparison of catalyst performance. The curve labeled as Sample 17 in Figure 8-2 a) was tested without the potential hold at 0.3 V.

MEA performance is summarized in Table 8-1. At 30 psig, Samples 16* & 17* can be directly compared with previous samples as they do not suffer from

performance

loss due to poor

lamination. Of

the original

samples,

Sample 10 has

the best kinetic

performance

and Sample 14

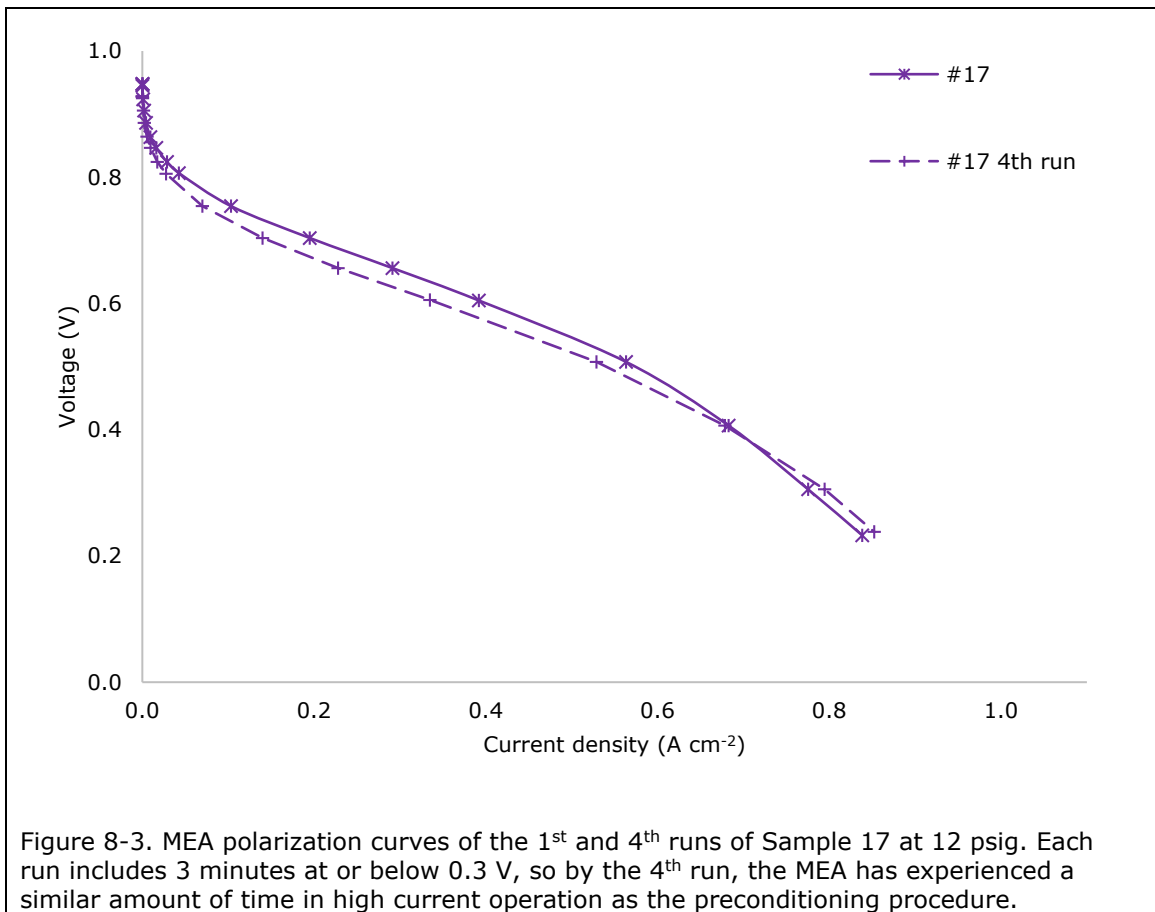
has the best

transport performance.

Table 8-1. MEA performance results. OCV in V, current at selected voltages in mA cm ⁻² . Samples 16* and 17* exhibited lamination issues with MEAs.						
12 psig (1.65 atm_{abs})						
Sample	OCV	0.9 V	0.85 V	0.8 V	0.6 V	0.4 V
8	0.909	0	3	12	217	566
10	0.937	1	5	12	187	542
14	0.903	0	1	7	186	552
16*	0.939	1	7	19	166	394
17*	0.954	2	8	24	148	564
17	0.948	3	15	50	400	689
30 psig (2.87 atm_{abs})						
8	0.903	0	4	20	291	685
10	0.928	1	9	30	303	653
14	0.887	0	3	15	266	688
16*	0.962	3	13	36	305	608
17*	0.979	4	17	48	442	805

Sample 16* demonstrates significantly improved kinetic performance with OCV and current above 0.8 V outperforming Sample 10. However, its transport performance is slightly worse than Sample 10, making it the worst performer below 0.5 V. Sample 17* has the best kinetic performance with an OCV 50 mV higher than Sample 10. This enhanced performance is present in all operation regimes with Sample 17 outperforming Sample 14 by 117 mA at 0.4 V.

At 12 psig, Sample 17 was run without the 0.3 V preconditioning hold. The original purpose of this hold was to activate the MEA and provide a baseline for stable, repeatable performance. I examined the stability and repeatability of testing an MEA without this hold. The 1st and 4th polarization curves are shown in Figure 8-3. There is little change in the performance of Sample 17 after multiple runs. Comparison of Sample 17 with the other samples shows that it outperforms them all by a wide margin in all operation regimes.



Performance testing of Sample 17 was also carried out using the US DOE protocols of 1 bar partial pressure O₂ and 2 bar partial pressure of air

(1.5 bar total O₂ at 100% RH and 2.5 bar total air at 100% RH). Polarization curves are shown in Figure 8-4, and the performance metrics are listed in Table 8-2. The current DOE target is 44 mA cm⁻² at 0.9 V in 1 bar O₂. Sample 17 produces 9 mA cm⁻² at 0.9 V and 44 mA cm⁻² at 0.85 V.

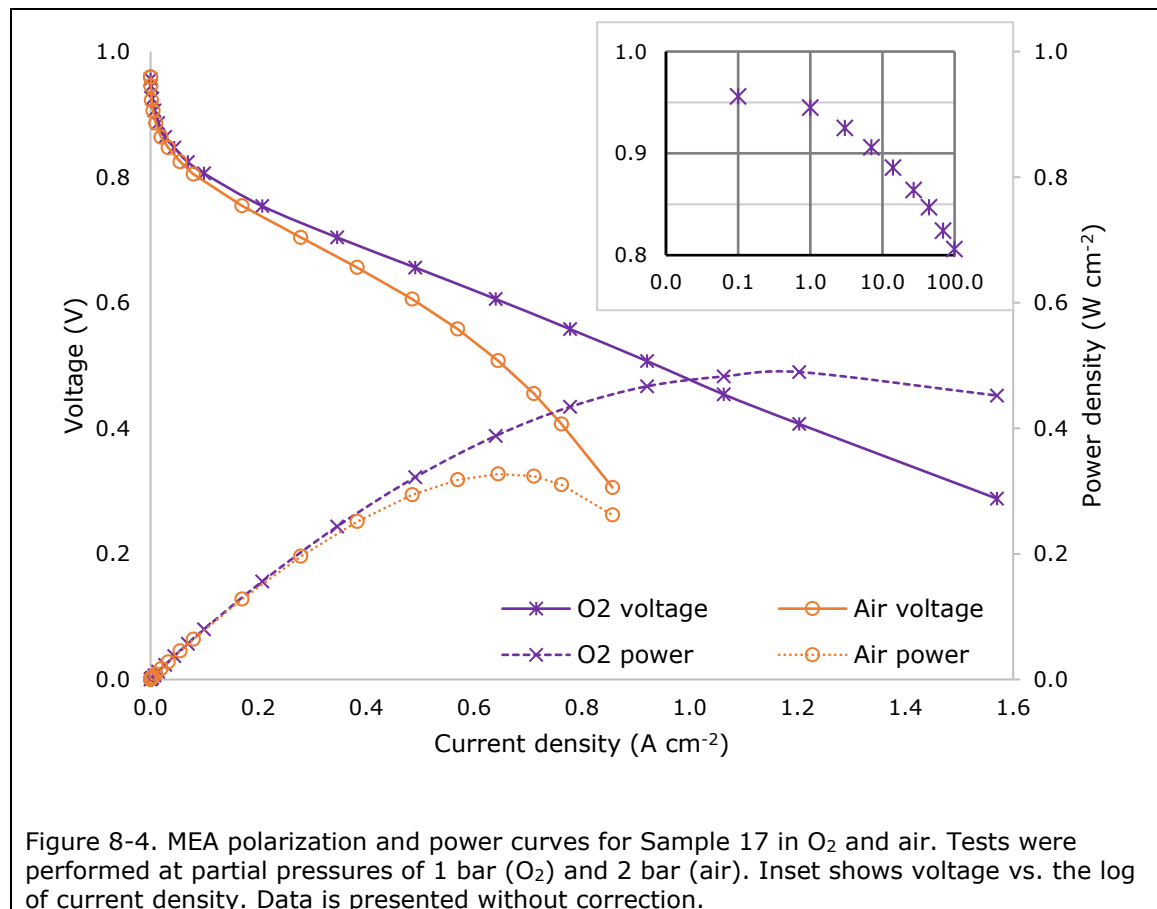


Table 8-2. Performance metrics from MEA testing of Sample 17. Testing conditions were 100% RH, 80 °C, 250/200 sccm at the anode/cathode respectively, 1.5 bar (H ₂ /O ₂) and 2.5 bar (H ₂ /Air) total pressures. Values presented are uncorrected.				
Testing conditions	OCV	Current density @ 0.9 V (mA cm ⁻²)	Current density @ 0.6 V (mA cm ⁻²)	Maximum power density (mW cm ⁻²)
1 bar O ₂	0.956	9	657	490
2 bar Air	0.959	6	496	324

8.3.4 – X-ray diffraction

X-ray diffraction patterns were acquired and processed using the structure refinement program for disordered carbons.¹³⁴ The results of that

analysis are shown in Table 8-3.

Table 8-3. Number of graphitic layers, in-plane strain (A.U.), and lateral coherence length (Å) measured by XRD.			
Sample	# of Layers	Strain	Lateral size
8	19	0.025	83
10	18	0.048	248
14	20	0.031	124
16	17	0.042	242
17	16	0.041	168

Samples 16 & 17 have fewer graphitic layers than any of the previous samples. This is consistent with the observed trend that samples with fewer layers exhibit increased electrochemical performance and further supports the

hypothesis that the primary active sites exist in the graphitic plane.

8.3.5 – X-ray photoelectron spectroscopy

Surface chemistry was analyzed by XPS. Elemental composition and speciation of C and N are presented in Table 8-4. Sample 17 has a total Fe content consistent with other well-performing samples. Sample 16 with 0.16 at.% Fe is higher than any other sample that exhibited good performance. Sample 16 has a graphitic C content consistent with other well-performing samples, whereas samples with high metallic Fe had increased graphitic C. Further, neither Sample 16 nor 17 exhibited high magnetic affinity, consistent with an absence of metallic Fe. Both samples have high concentrations of surface oxides, which have been correlated with good performance. However, their concentration of N-Fe, which correlates with both performance and surface oxides in other samples, are mediocre. The

concentration of N-Fe being lower than other well performing catalysts bears further examination. Nanoscale elemental distribution analysis, as performed in Chapter 6, could provide additional insight.

Table 8-4. XPS elemental composition, C 1s and N 1s speciation of catalyst powders.								
	Catalyst elemental composition, at. %							
	C	O	N	Fe				
s.8	87.8	9.3	2.8	0.11				
s.10	89.5	6.4	4.0	0.12				
s.14	88.3	8.8	2.9	0.12				
s.16	90.3	6.3	3.2	0.16				
s.17	91.8	4.6	3.5	0.12				
	catalyst C speciation, rel. %			catalyst N speciation, rel. %				
	C gr	C-N	C _x O _y	N pyrid	N _x -Fe	N hydrogenated	N gr/ N ⁺	NO _x
s.8	8.2	27.9	60.7	22.9	18.8	18.8	18.3	20.4
s.10	9.5	15.2	69.3	24.5	19.8	22.5	15.5	17.7
s.14	22.2	25.5	49.1	22.2	17.4	24.6	18.0	17.9
s.16	11.2	14.2	70.6	25.0	15.0	21.7	22.6	15.7
s.17	9.6	17.2	68.7	21.8	15.1	35.2	14.5	13.4

Sample 16, having had the 2nd pyrolysis gas changed from NH₃ to Ar half way through, was under reductive atmosphere for only half of its second heat treatment. Sample 17 was under reductive conditions for the entire second pyrolysis. As expected, Sample 16 has a higher concentration of surface oxides, though only by a small amount (71% vs. 69%). Also interesting is the fact that Sample 16 has a higher concentration of NO_x (16% vs. 13%). This is representative of chemical changes that occur specifically during the second pyrolysis. The second heat treatment does more than just solidify the material structure; significant solid-state chemical reactions that affect the chemistry, structure, and performance of the final catalyst occur during the second pyrolysis.

8.4 – Conclusion

I have synthesized new materials based on synthesis – structure – property relationships developed in the previous chapters. One of the new samples outperformed all previous samples in RDE testing and the kinetic region of MEA operation but exhibited poor MEA transport performance. The other new sample far outperformed all previous samples both RDE testing and all regimes of MEA operation.

In these new materials, though the positive correlation between surface oxides and performance is observed, the correlation between N-Fe and performance is absent. Samples 16 & 17 do have the fewest graphitic layers of all analyzed samples, which is consistent with the previously observed trend. This correlation is consistent with MNC catalyst active sites existing in the graphitic plane as opposed to on edge defects.

Chapter 9 – Conclusion and Significance

Detailed analysis of synthetic parameters, physicochemical properties, length-scale specific morphology, and performance characteristics elucidate several structure-to-property relationships in iron-nicarbazin derived catalysts for the oxygen reduction reaction in fuel cells:

- Increased concentrations of atomically dispersed iron promote both electrochemical activity and fuel cell performance.
- The presence of iron nanoparticles tends to reduce the concentration of atomically dispersed iron; however, even in cases where atomically dispersed iron remains abundant, iron nanoparticles reduce catalyst performance.
- Atomically dispersed iron concentration trends as the concentration of nitrogen bound to iron, providing evidence that the active species in these catalysts are iron-nitrogen centers as opposed to iron-rich particles.
- The concentration of surface oxides represent defects in the carbon structure where these active sites can form.
- Concentrations of nitrogen bound to iron and pyridinic nitrogen are related to catalyst surface features in the size range of 8 nm.
- Catalysts with fewer graphitic layers show increased activity, which is consistent with active sites residing in the graphitic plane as opposed to on edge defects.

Synthetic parameters have been identified that affect these chemistries and can be used to synthesize materials with improved catalytic performance:

- Thorough milling of the material after the 1st pyrolysis and before leaching promotes more complete leaching of iron-rich phases.
- The addition of carbon nanotubes results in a reduced active site concentration and lower catalyst activity.
- A more reductive atmosphere and increased time during the 2nd pyrolysis each decrease the concentration of surface oxides and active sites.
- Much of the chemical modification necessary for catalyst activity occurs during the second pyrolysis, making it a powerful tool for fine-tuning catalyst performance.

Utilizing the insights gained in this work, I have synthesized new catalyst materials with significantly improved performance in all performance regimes. The structure-to-property relationships and changes in synthetic techniques used to improve these iron-nicarbazin derived catalysts can be applied to platinum-group metal free catalysts of multiple precursors.

Integration of fuel cell technology into everyday life requires a significant reduction in the cost of materials, a cost that is currently dominated by the need for platinum as a catalyst. Development of low-cost platinum-group metal free catalysts requires understanding of both the fundamental structure-to-property relationships of these materials as well as

engineering parameters necessary to improve their performance in fuel cell operation. My research provides substantive new knowledge in both areas, advancing the state of the art and facilitating improved rational design of low-cost fuel cell catalysts.

10 – Publications in Peer-Reviewed Journals

Workman, M. J.; Dzara, M. J.; Ngo, C.; Pylypenko, S.; Serov, A.; McKinney, S.; Gordon, J.; Atanassov, P.; Artyushkova, K. Platinum Group Metal-Free Electrocatalysts: Effects of Synthesis on Structure and Performance in Proton-Exchange Membrane Fuel Cell Cathodes. *J Power Sources* (2017), 348, 30-39.

Rojas-Carbonell, S.; Babanova, S.; Serov, A.; Artyushkova, K.; **Workman, M. J.**; Santoro, C.; Mirabal, A.; Calabrese Barton, S.; Atanassov, P. Integration of Platinum Group Metal-Free Catalysts with Bilirubin Oxidase into a Hybrid Material for Oxygen Reduction Reaction: Interplay of Chemistry and Morphology. *ChemSusChem* (2017), DOI: 10.1002/cssc.201601822.

Stariha, S.; Artyushkova, K.; **Workman, M. J.**; Serov, A.; McKinney, S.; Halevi, B.; Atanassov, P. PGM-free Fe-N-C catalysts for oxygen reduction reaction: Catalyst layer design. *J Power Sources* (2016), 326, 43-49.

Serov, A.; **Workman, M. J.**; Artyushkova, K.; Atanassov, P.; McCool, G.; McKinney, S.; Romero, H.; Halevi, B.; Stephenson, T. Highly stable precious metal-free cathode catalyst for fuel cell application. *J Power Sources* (2016), 327, 557-564.

Workman, M. J.; Serov, A.; Halevi, B.; Atanassov, P.; Artyushkova, K. Application of the Discrete Wavelet Transform to SEM and AFM Micrographs for Quantitative Analysis of Complex Surfaces. *Langmuir* (2015), 31, 4924-33.

11 – Presentations Published as Abstracts

Workman, M. J.; Serov, A.; Dzara, M. J.; Ngo, C.; Gordon, J.; McKinney, S.; Pylypenko, S.; Atanassov, P.; Artyushkova, K. Relationship of Chemical Composition, Crystalline Structure, and Morphology to ORR Performance in Transition Metal-Nitrogen-Carbon (MNC) Catalysts. In *2016 Pacific Rim Meeting of the Electrochemical Society*, Honolulu, HI, 2016.

Artyushkova, K.; **Workman, M. J.**; Gordon, J.; Matanovic, I.; Serov, A.; Atanassov, P. Interplay Between Chemistry and Morphology of the Catalytic Layer in Platinum Group Metal-Free Cathodes. In *2016 Pacific Rim Meeting of the Electrochemical Society*, Honolulu, HI, 2016.

Dzara, M. J.; Ngo, C.; **Workman, M. J.**; Atanassov, P.; Artyushkova, K. Advanced Microscopy of Non-Precious Metal Catalysts for Structure-Property-Performance Correlations. In *2016 Pacific Rim Meeting of the Electrochemical Society*, Honolulu, HI, 2016.

Workman, M. J.; Artyushkova, K.; Halevi, B.; Serov, A.; Atanassov, P. Three-Dimensional Microstructure of PEFC Electrodes: Activity and Durability. In *228th Electrochemical Society Meeting*, Phoenix, AZ, 2015.

Artyushkova, K.; Serov, A.; **Workman, M. J.**; Atanassov, P. The Role of Chemistry and Morphology of Carbon in Oxygen Reduction Reaction. Structure-to-Property Studies. In *227th Electrochemical Society Meeting*, Chicago, IL, 2015.

Artyushkova, K.; Serov, A.; **Workman, M. J.**; Atanassov, P. Role of Surface Chemistry and Morphology in Oxygen Reduction Reaction. In *AVS Regional Meeting*, Golden, CO 2015.

Serov, A.; Stariha, S.; **Workman, M. J.**; Artyushkova, K.; Atanassov, P. "Smart MEA" Approach: Design of Catalyst Layer. In *2015 AIChE Annual Meeting*, Salt Lake City, UT, 2015.

Workman, M. J.; Serov, A.; Atanassov, P.; Artyushkova, K. Structure-to-Property Relationships in Non-Platinum Group Fuel Cell Catalysts at the Mesoscale. In *226th Electrochemical Society Meeting*, Cancun, Quintana Roo, Mexico, 2014.

Leonard, N.; Serov, A.; **Workman, M. J.**; Atanassov, P.; Calabrese Barton, S. Transport Model for Non-PGM Cathodes in Proton-Exchange Membrane Fuel Cells. In *226th Electrochemical Society Meeting*, Cancun, Quintana Roo, Mexico, 2014.

Workman, M. J.; Serov, A.; Rojas Carbonell, M. S.; Atanassov, P.; Artyushkova, K. Structure-to-Property Relationships in Non-Platinum Group Fuel Cell Catalysts: Examination of Length Scale Correlations. In *224th Electrochemical Society Meeting*, San Francisco, CA, 2013.

Artyushkova, K.; **Workman, M. J.**; Serov, A.; Kiefer, B.; Atanassov, P. Structure-to-property relationship between chemistry, hierarchy of morphology, and performance for non-platinum ORR electrocatalysts. In *245th American Chemical Society National Meeting*, New Orleans, LA, 2013.

Appendix A – SI for DWT Manuscript

Application of the Discrete Wavelet Transform to SEM and AFM for
Quantitative Analysis of Complex Surfaces

Supporting Information

Mathematical description of the Discrete Wavelet Transform (DWT)

The terms used in this description are:

The original signal S , where $S = S(x)$ for a continuous signal and $S = S(n)$ for a discrete signal of n points.

The scaling (or dilation factor) a at level j such that $a = 2^j$, where j is a positive integer.

The translation factor b such that $b = ka$, where k is an integer.

The details at level j , D_j .

The approximation at level j , A_j .

The one-dimensional wavelet Ψ with the property that $\int \Psi(x)dx = 0$.

The one-dimensional scaling function Φ with the property that $\int \Phi(x)dx = 1$.

The detail coefficients, $C_{j,k}$.

The approximation coefficients, $B_{j,k}$.

The wavelet function is convoluted with the signal to get the detail coefficients at each level and position.

$$C_{j,k} = \sum_n S(n) \Psi_{j,k}(n) \quad (S1)$$

These detail coefficients represent the amount of the wavelet function present in the original signal at each position and scale. These coefficients can be analyzed directly as they contain information about the signal energy (related to roughness), and retain the location of features in the signal. Note that the scaling factor operates on a dyadic scale and that the translation factor depends on the scaling factor. The results of this are that each detail level is twice the scale as the previous level and that the convolution is performed at discrete locations corresponding to the size of the wavelet. These details can then be reconstructed at each level by:

$$D_j(n) = \sum_k C(j, k) \Psi_{j,k}(n) \quad (S2)$$

It is these detail reconstructions, not the coefficients, that are used for analysis in this work.

While the details contain the signal information from a narrow size range, the approximations contain all of the information of the signal *larger* than a given size. Approximations are particularly useful for filtering as they allow the removal of smaller features while retaining the overall shape. The approximation coefficients are given by:

$$B_{j,k} = \sum_n S(n) \Phi_{j,k}(n) \quad (S3)$$

The approximations can be defined equivalently by the scaling function and by the details. For a specific level, J , the approximation is:

$$A_J(n) = \sum_k B_{J,k} \Phi_{J,k}(n) = \sum_{j>J} D_j(n) \quad (S4)$$

This means that the approximation at any level is the sum of all of the details at every higher level.

From Equations S1 – S4, and the fact that these wavelets are a complete orthonormal basis, some important properties follow. Because the wavelets at different levels are orthogonal, information at one detail level is not repeated in any other detail level. Because it is a complete basis, the original signal is preserved between the transform and inverse transform. Further, the original signal can be recovered from an approximation and all of the detail levels below it, so:

$$S(n) = A_J + D_J + D_{J-1} + D_{J-2} + \cdots + D_1 \quad (S5)$$

Equation 7 leads to some important properties and applications. For traditional filtering, the small detail levels are discarded as noise and the approximation is kept as the useful part of the signal for analysis. This allows for removal of information of small features known to be noise without loss of information of large features of interest. As discussed earlier, wavelet analysis has previously been used to remove the small and large detail levels in order to isolate a known intermediate size range for analysis. However, Equation S5 also indicates that all of the information *up to* a maximum size of interest can be captured, without loss, in the details, and the approximation can be discarded as waviness/tilt of a surface. This is the approach taken here.

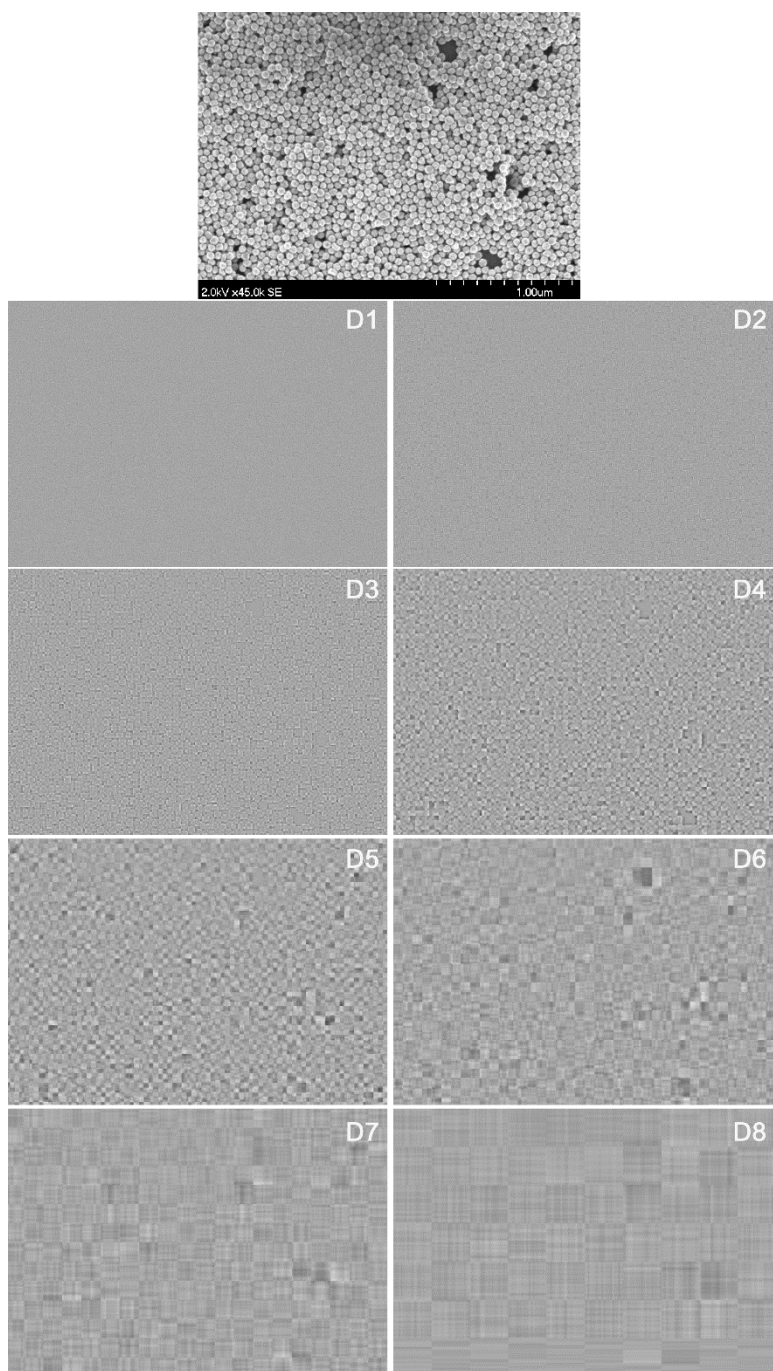


Figure S1. D₁-D₈ reconstructions for an SEM image of 55 nm Au nanospheres. Reconstructions created by averaging vertical and horizontal reconstructions. At this zoom level (0.45 pixel/nm), the average lateral size of the nanospheres is 19 pixels. The size of the wavelet at D₅ is 16 pixels.

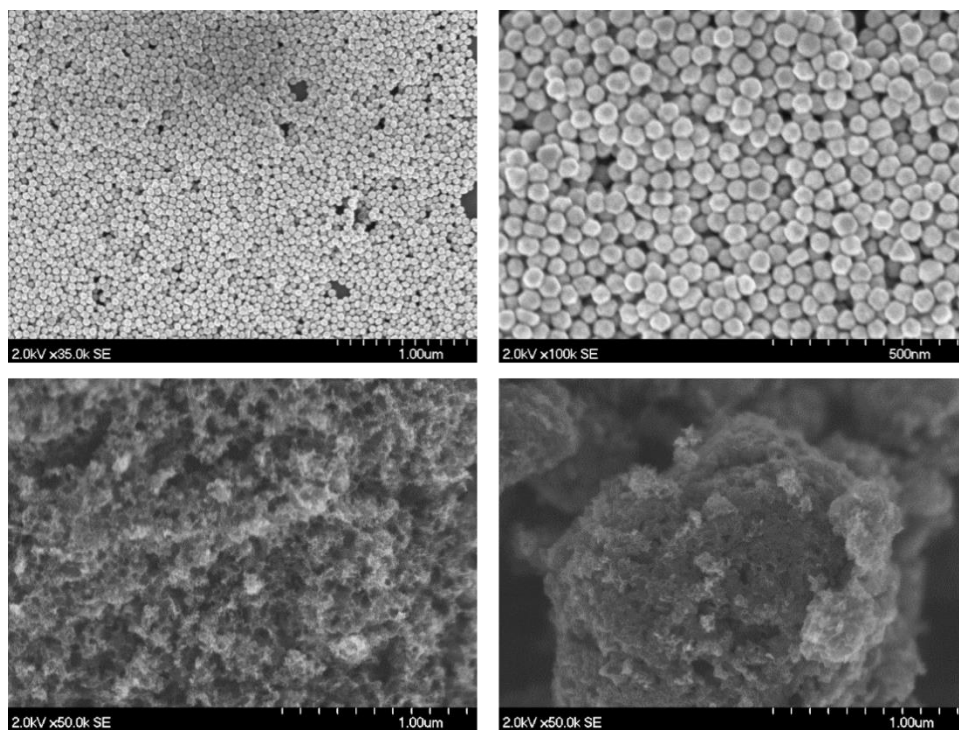


Figure S2. SEM images used for best wavelet selection. The top images are Au nanospheres at different zoom levels. From left to right, the bottom images are Fe-Aminoantipyrine and Fe-Carbendazim based non-PGM catalysts. All images are 1280 pixels horizontally and 890 pixels vertically (not including the SEM information bar).

Table S1

Average Roughness at each detail level (Total roughness = 1)		Size of image features (pixels)							
		2	3, 4, 5	$2^{2.5} - 2^{3.4}$	$2^{3.5} - 2^{4.4}$	$2^{4.5} - 2^{5.4}$	$2^{5.5} - 2^{6.4}$	$2^{6.5} - 2^{7.4}$	$2^{7.5} - 2^{8.4}$
	D ₁	0.707	0.328	0.165	0.083	0.041	0.021	0.010	0.005
	D ₂	0.707	0.559	0.313	0.161	0.081	0.041	0.021	0.010
	D ₃	0.000	0.488	0.548	0.309	0.160	0.081	0.041	0.021
	D ₄	0.019	0.088	0.474	0.542	0.307	0.160	0.081	0.041
	D ₅	0.015	0.072	0.075	0.472	0.542	0.307	0.160	0.081
	D ₆	0.011	0.027	0.066	0.070	0.471	0.542	0.310	0.160
	D ₇	0.008	0.020	0.030	0.064	0.069	0.470	0.539	0.309
	D ₈	0.000	0.006	0.013	0.026	0.060	0.066	0.444	0.513
	D ₉	0.007	0.012	0.010	0.019	0.035	0.062	0.137	0.453
	D ₁₀	0.006	0.011	0.008	0.009	0.020	0.032	0.089	0.098

Table S1. Measured roughness at each detail level for the generated images. The values are in relative intensity for an image with a total roughness of 1.

Table S2

1.0000	0.7071	0.3084	0.1601	0.0815	0.0410	0.0206	0.0103	0.0000	0.0000
0.0000	0.7071	0.5355	0.3084	0.1601	0.0815	0.0410	0.0206	0.0103	0.0000
0.0000	0.0000	0.4620	0.5355	0.3084	0.1601	0.0815	0.0410	0.0206	0.0103
0.0000	0.0000	0.0881	0.4620	0.5355	0.3084	0.1601	0.0815	0.0410	0.0206
0.0000	0.0000	0.0686	0.0881	0.4620	0.5355	0.3084	0.1601	0.0815	0.0410
0.0000	0.0000	0.0309	0.0686	0.0881	0.4620	0.5355	0.3084	0.1601	0.0815
0.0000	0.0000	0.0173	0.0309	0.0686	0.0881	0.4620	0.5355	0.3084	0.1601
0.0000	0.0000	0.0000	0.0173	0.0309	0.0686	0.0881	0.4620	0.5355	0.3084
0.0000	0.0000	0.0000	0.0000	0.0173	0.0309	0.0686	0.0881	0.4620	0.5355
0.0000	0.0000	0.0000	0.0000	0.0000	0.0173	0.0309	0.0686	0.0881	0.4620

Table S2. This is the C matrix used for fitting of the roughness curves. The orientation of the rows and columns is the same as in Table S1. For the curve fitting, the 3rd column which corresponds to sizes at D₃, the average values for sizes corresponding to D₄-D₉ were used.

Table S3

Detail Level	Wavelet size (nm) at 0.5 pixel/nm zoom	Fit Range (nm) at 0.5 pixel/nm zoom	Wavelet size (nm) at 2.0 pixel/nm zoom	Fit Range (nm) at 2.0 pixel/nm zoom
2	4	4	1	1
3	8	6-10	2	1.5-2.5
4	16	11-21	4	3-5
5	32	22-42	8	6-10
6	64	45-84	16	11-21
7	128	90-168	32	22-42

Table S3. Wavelet and fit roughness size ranges at each detail level for each zoom level.

Appendix B – FIB tomography procedure

For FEI Quanta 3D dual-beam FIB/SEM

Sample Preparation

- **Vent** chamber
- SEM stub → carbon tape → small sample square
- Screw in SEM stub into holder → set rotation to -160° → brace holder
- Make sure BSE detector is removed
- **Pump** chamber
- ETD (BSE) detector

Electron Beam / Ion Beam Start Up

- Electron Beam → 5.0 kV, 6.7 pA
 - Under Beam tab, SEM aperture, set to 30 μm
- Click auto contrast
- Roughly zoom on the corner of the sample
- set $z = 10$ → Click link z → set $z = 10$ → link z
- Ion Beam → 30.0 kV, 3 nA
 - Make sure box turns yellow
- May need to click auto contrast
- Couple magnification

First Electron Beam Optimization

- Zero beam shift
- Source tilt, crossover → make sure X is in center of the circle
- Lens alignment → image should pulse in and out NOT UP AND DOWN
- Optimization stigmation at 1 μm using small box → scan rate of 3 μs
- *Set Snapshot Preferences*
- Beam → preferences → snap 5.0-10 μs (depending on available time, longer is better)
 - Dwell time: 5-10 μs , Resolution: 2048x1768, Acquisition: 16 bit, Save As tif.16 (18.4-60 seconds)

Eucentric Ion Beam

- Right click Pt dep (heater)
- 20-30 μm zoom → find feature toward test area → focus (1 μm) → z link → set $z = 10$
- Tilt 15° → adjust z knob on drawer so feature is on same level as yellow marker
- Tilt back to 0° → re-center feature → focus → z link
- Tilt 30° → adjust z knob on drawer so feature is on same level as yellow marker
- Tilt back to 0° → re-center feature → focus → z link
- Snapshot electron beam → tilt 52°

- Click on ion beam square, turn on beam → zero beam shift, may need to manually to match electron beam snapshot, may need to auto contrast
- Optimize ion beam → BLANK ION BEAM
- Tilt back to 0°

Pt Deposition

- Find analysis area
- Zoom in to 5000x → focus → z link
- Zoom back out
- Tilt back to 52°
- Go to ion beam square → Open small box for ion beam in corner → set to deposition current (1 nA for 20x10 µm) → optimize
- Make rectangle 20x10x4 µm → Make sure application **Pt dep**
- zoom until rectangle is most of screen
- Insert needle → PLAY! (~27 min)
- Withdraw needle → Uncouple magnification → snapshot ion beam → look with electron beam
- Pattern line → advances setting 45°, 1.0 µm deep, **application Si**

Trenches

- Back to ion beam → WITHOUT BEAM ON, zoom out, scroll Pt cap up
- Set ion beam to 15 nA (can possibly go higher) → open up small box across bottom, AWAY FROM PT CAP → optimize beam in corner → snapshot
- Front trench → Cleaning cross section 35x30x5 µm ~7 µm away from Pt cap → PLAY! (~23min) → ion beam snapshot → check electron beam 5000x magnification
- Side Trenches → rectangle 10x20x4 µm (can do both at one time)

Clean-Up Cuts

- Drop current to 5 nA → open up small box across bottom, AWAY FROM PT CAP → optimize beam in corner → snapshot
- Cut 4 µm right up to Pt cap, leave a little space on the sides from Pt cap
- Snapshot ion beam → optimize electron beam

Imaging Slices

- Set contrast as high as possible, make sure image is bright enough to see everything
- On ion screen make Pt cap most of screen and centered
- Set cleaning cross section → 3 nA, 3 µm deep, close to front, little extra on sides, past the back
- Name first image section, set snapshot preferences to save
Will need to shift y down (counter clock wise) to make sure reference line stays in view

References

1. U.S. Energy Information Administration / Monthly Energy Review February 2016. U.S. DOE. Washington DC, 2016.
2. Zamuda, C.; Mignone, B.; Bilello, D.; Hallett, K.; Lee, C.; Macknick, J.; Newmark, R.; Steinberg, D. *US Energy Sector Vulnerabilities to Climate Change and Extreme Weather*; Department of Energy: Washington DC, 2013.
3. Heller, A. Wealth, Global Warming and Geoengineering. In *228th Meeting of the Electrochemical Society*, Phoenix, AZ, 2015.
4. Williams, H.; Havens, D.; Banks, K.; Wachal, D. Field-based monitoring of sediment runoff from natural gas well sites in Denton County, Texas, USA. *Environmental Geology* 2008, 55, 1463-1471.
5. Burton, A.; Nadelhoffer, K. Hydraulic Fracturing in the State of Michigan-Environment/Ecology Technical Report. 2013.
6. Annual Energy Review 2011. Energy Information Administration. Government Printing Office: 2012.
7. Shao, M.; Chang, Q.; Dodelet, J. P.; Chenitz, R. Recent Advances in Electrocatalysts for Oxygen Reduction Reaction. *Chem Rev* 2016.
8. Wang, Y.; Chen, K. S.; Mishler, J.; Cho, S. C.; Adroher, X. C. A review of polymer electrolyte membrane fuel cells: Technology, applications, and needs on fundamental research. *Applied Energy* 2011, 88, 981-1007.
9. Jaouen, F.; Proietti, E.; Lefevre, M.; Chenitz, R.; Dodelet, J. P.; Wu, G.; Chung, H. T.; Johnston, C. M.; Zelenay, P. Recent advances in non-precious metal catalysis for oxygen-reduction reaction in polymer electrolyte fuel cells. *Energ Environ Sci* 2011, 4, 114-130.
10. Fuel cell: proton exchange membrane fuel cell.
<http://kids.britannica.com/comptons/art-106689> (accessed 4/4/2016).
11. Robson, M. H.; Serov, A.; Artyushkova, K.; Atanassov, P. A mechanistic study of 4-aminoantipyrine and iron derived non-platinum group metal catalyst on the oxygen reduction reaction. *Electrochim Acta* 2013, 90, 656-665.
12. Loferski, P. J. *U.S. Geological Survey, Mineral Commodity Summaries, January 2015*; U.S. Geological Survey: Washington DC, January 2015, 2015; pp 120-121.
13. Chen, Z.; Higgins, D.; Yu, A.; Zhang, L.; Zhang, J. A review on non-precious metal electrocatalysts for PEM fuel cells. *Energ Environ Sci* 2011, 4, 3167-3192.
14. Jaouen, F.; Herranz, J.; Lefevre, M.; Dodelet, J. P.; Kramm, U. I.; Herrmann, I.; Bogdanoff, P.; Maruyama, J.; Nagaoka, T.; Garsuch, A.; Dahn, J. R.; Olson, T.; Pylypenko, S.; Atanassov, P.; Ustinov, E. A. Cross-laboratory experimental study of non-noble-metal electrocatalysts for the oxygen reduction reaction. *ACS Appl Mater Interfaces* 2009, 1, 1623-39.
15. Jasinski, R. A new fuel cell cathode catalyst. 1964.
16. Kramm, U. I. Fuel Cells, Non-Precious Metal Catalysts for Oxygen Reduction Reaction. In *Encyclopedia of Applied Electrochemistry*, Kreysa, G.; Ota, K.-i.; Savinell, R. F., Eds. Springer New York: New York, NY, 2014; pp 909-918.

17. Bezerra, C. W.; Zhang, L.; Lee, K.; Liu, H.; Marques, A. L.; Marques, E. P.; Wang, H.; Zhang, J. A review of Fe-N/C and Co-N/C catalysts for the oxygen reduction reaction. *Electrochim Acta* 2008, 53, 4937-4951.
18. Higgins, D. C.; Chen, Z. Recent progress in non-precious metal catalysts for PEM fuel cell applications. *The Canadian Journal of Chemical Engineering* 2013, 91, 1881-1895.
19. Liu, G.; Li, X.; Lee, J.-W.; Popov, B. N. A review of the development of nitrogen-modified carbon-based catalysts for oxygen reduction at USC. *Catalysis Science & Technology* 2011, 1, 207-217.
20. Su, D. S.; Sun, G. Nonprecious-Metal Catalysts for Low-Cost Fuel Cells. *Angewandte Chemie International Edition* 2011, 50, 11570-11572.
21. Wood, K. N.; O'Hayre, R.; Pylypenko, S. Recent progress on nitrogen/carbon structures designed for use in energy and sustainability applications. *Energ Environ Sci* 2014, 7, 1212-1249.
22. Jaouen, F. Heat-Treated Transition Metal-NxCy Electrocatalysts for the O₂ Reduction Reaction in Acid PEM Fuel Cells. In *Non-Noble Metal Fuel Cell Catalysts*, Wiley-VCH Verlag GmbH & Co. KGaA: 2014; pp 29-118.
23. Johnston, C. M.; Piela, P.; Zelenay, P. Transition metal/polymer catalysts for O₂ reduction. In *Handbook of Fuel Cells*, John Wiley & Sons, Ltd: 2010.
24. Kramm, U. I.; Herranz, J.; Larouche, N.; Arruda, T. M.; Lefevre, M.; Jaouen, F.; Bogdanoff, P.; Fiechter, S.; Abs-Wurmbach, I.; Mukerjee, S.; Dodelet, J. P. Structure of the catalytic sites in Fe/N/C-catalysts for O₂-reduction in PEM fuel cells. *Phys Chem Chem Phys* 2012, 14, 11673-11688.
25. Collman, J. P.; Decréau, R. A. Functional biomimetic models for the active site in the respiratory enzyme cytochrome c oxidase. *Chemical Communications* 2008, 5065-5076.
26. Gloaguen, F.; Andolfatto, F.; Durand, R.; Ozil, P. Kinetic study of electrochemical reactions at catalyst-recast ionomer interfaces from thin active layer modelling. *J Appl Electrochem* 1994, 24, 863-869.
27. Jaouen, F.; Lefèvre, M.; Dodelet, J.-P.; Cai, M. Heat-treated Fe/N/C catalysts for O₂ electroreduction: are active sites hosted in micropores? *The Journal of Physical Chemistry B* 2006, 110, 5553-5558.
28. Brunauer, S.; Emmett, P. H.; Teller, E. Adsorption of gases in multimolecular layers. *Journal of the American chemical society* 1938, 60, 309-319.
29. Barrett, E. P.; Joyner, L. G.; Halenda, P. P. The determination of pore volume and area distributions in porous substances. I. Computations from nitrogen isotherms. *Journal of the American Chemical society* 1951, 73, 373-380.
30. Ustinov, E. A.; Do, D. D.; Fenelonov, V. B. Pore size distribution analysis of activated carbons: Application of density functional theory using nongraphitized carbon black as a reference system. *Carbon* 2006, 44, 653-663.
31. Burrell, J. W. Gas Sorption in Engineered Carbon Nanospaces. University of Missouri, Columbia, MO, 2009.
32. Szakacs, C. E.; Lefevre, M.; Kramm, U. I.; Dodelet, J. P.; Vidal, F. A density functional theory study of catalytic sites for oxygen reduction in

- Fe/N/C catalysts used in H₂/O₂ fuel cells. *Phys Chem Chem Phys* 2014, 16, 13654-61.
33. Slavcheva, E.; Ganske, G.; Topalov, G.; Mokwa, W.; Schnakenberg, U. Effect of sputtering parameters on surface morphology and catalytic efficiency of thin platinum films. *Applied Surface Science* 2009, 255, 6479-6486.
 34. Ang, S.; Walsh, D. Palladium-vanadium alloy electrocatalysts for oxygen reduction: Effect of heat treatment on electrocatalytic activity and stability. *Applied Catalysis B-Environmental* 2010, 98, 49-56.
 35. Aragane, J.; Urushibata, H. XPS and Fe-SEM Analysis of Platinum Electrocatalysts in a Phosphoric-acid Fuel-Cell. *Nippon Kagaku Kaishi* 1995, 736-742.
 36. Maksumov, A.; Vidu, R.; Palazoglu, A.; Stroeve, P. Enhanced feature analysis using wavelets for scanning probe microscopy images of surfaces. *Journal of Colloid and Interface Science* 2004, 272, 365-377.
 37. Tsai, D. M.; Hsiao, B. Automatic surface inspection using wavelet reconstruction. *Pattern Recognit.* 2001, 34, 1285-1305.
 38. Artyushkova, K.; Pylypenko, S.; Dowlapalli, M.; Atanassov, P. Use of digital image processing of microscopic images and multivariate analysis for quantitative correlation of morphology, activity and durability of electrocatalysts. *Rsc Adv* 2012, 2, 4304-4310.
 39. Reshetenko, T. V.; St-Pierre, J.; Artyushkova, K.; Rocheleau, R.; Atanassov, P.; Bender, G.; Ulsh, M. Multianalytical Study of the PTFE Content Local Variation of the PEMFC Gas Diffusion Layer. *J. Electrochem. Soc.* 2013, 160, F1305-F1315.
 40. ISO. Geometrical Product Specifications (GPS) - Surface texture: Profile method -Terms, definitions and surface texture parameters. In 4287, 1997; Vol. 4287.
 41. Santoro, C.; Guilizzoni, M.; Correa Baena, J. P.; Pasaogullari, U.; Casalegno, A.; Li, B.; Babanova, S.; Artyushkova, K.; Atanassov, P. The effects of carbon electrode surface properties on bacteria attachment and start up time of microbial fuel cells. *Carbon* 2013.
 42. Shi, H.; Reimers, J.; Dahn, J. Structure-refinement program for disordered carbons. *Journal of applied crystallography* 1993, 26, 827-836.
 43. Jia, Q.; Ramaswamy, N.; Hafiz, H.; Tylus, U.; Strickland, K.; Wu, G.; Barbiellini, B.; Bansil, A.; Holby, E. F.; Zelenay, P. Experimental Observation of Redox-Induced Fe-N Switching Behavior as a Determinant Role for Oxygen Reduction Activity. *Acs Nano* 2015, 9, 12496-12505.
 44. Serov, A.; Artyushkova, K.; Niangar, E.; Wang, C.; Dale, N.; Jaouen, F.; Sougrati, M.-T.; Jia, Q.; Mukerjee, S.; Atanassov, P. Nano-structured non-platinum catalysts for automotive fuel cell application. *Nano Energy* 2015, 16, 293-300.
 45. Strickland, K.; Miner, E.; Jia, Q.; Tylus, U.; Ramaswamy, N.; Liang, W.; Sougrati, M.-T.; Jaouen, F.; Mukerjee, S. Highly active oxygen reduction non-platinum group metal electrocatalyst without direct metal-nitrogen coordination. *Nat Commun* 2015, 6.

46. Serov, A.; Artyushkova, K.; Atanassov, P. Fe-N-C Oxygen Reduction Fuel Cell Catalyst Derived from Carbendazim: Synthesis, Structure, and Reactivity. *Adv Energy Mater* 2014, 4.
47. Serov, A.; Robson, M. H.; Artyushkova, K.; Atanassov, P. Templated non-PGM cathode catalysts derived from iron and poly(ethyleneimine) precursors. *Applied Catalysis B: Environmental* 2012, 127, 300-306.
48. Serov, A.; Robson, M. H.; Halevi, B.; Artyushkova, K.; Atanassov, P. Highly active and durable templated non-PGM cathode catalysts derived from iron and aminoantipyrine. *Electrochemistry Communications* 2012, 22, 53-56.
49. Serov, A.; Tylus, U.; Artyushkova, K.; Mukerjee, S.; Atanassov, P. Mechanistic studies of oxygen reduction on Fe-PEI derived non-PGM electrocatalysts. *Applied Catalysis B-Environmental* 2014, 150, 179-186.
50. Artyushkova, K.; Pylypenko, S.; Dowlapalli, M.; Atanassov, P. Structure-to-property relationships in fuel cell catalyst supports: Correlation of surface chemistry and morphology with oxidation resistance of carbon blacks. *J Power Sources* 2012, 214, 303-313.
51. Wu, G.; Johnston, C. M.; Mack, N. H.; Artyushkova, K.; Ferrandon, M.; Nelson, M.; Lezama-Pacheco, J. S.; Conradson, S. D.; More, K. L.; Myers, D. J.; Zelenay, P. Synthesis-structure-performance correlation for polyaniline-Me-C non-precious metal cathode catalysts for oxygen reduction in fuel cells. *J Mater Chem* 2011, 21, 11392-11405.
52. Matter, P. H.; Zhang, L.; Ozkan, U. S. The role of nanostructure in nitrogen-containing carbon catalysts for the oxygen reduction reaction. *Journal of Catalysis* 2006, 239, 83-96.
53. Domínguez, C.; Pérez-Alonso, F. J.; Abdel Salam, M.; Al-Thabaiti, S. A.; Obaid, A. Y.; Alshehri, A. A.; Gómez de la Fuente, J. L.; Fierro, J. L. G.; Rojas, S. On the relationship between N content, textural properties and catalytic performance for the oxygen reduction reaction of N/CNT. *Applied Catalysis B: Environmental* 2015, 162, 420-429.
54. Lin, L.; Zhu, Q.; Xu, A.-W. Noble-Metal-Free Fe-N/C Catalyst for Highly Efficient Oxygen Reduction Reaction under Both Alkaline and Acidic Conditions. *Journal of the American Chemical Society* 2014, 136, 11027-11033.
55. Singh, D.; Tian, J.; Mamtani, K.; King, J.; Miller, J. T.; Ozkan, U. S. A comparison of N-containing carbon nanostructures (CNx) and N-coordinated iron-carbon catalysts (FeNC) for the oxygen reduction reaction in acidic media. *Journal of Catalysis* 2014, 317, 30-43.
56. Kramm, U. I.; Lefèvre, M.; Larouche, N.; Schmeisser, D.; Dodelet, J.-P. Correlations between Mass Activity and Physicochemical Properties of Fe/N/C Catalysts for the ORR in PEM Fuel Cell via ⁵⁷Fe Mössbauer Spectroscopy and Other Techniques. *Journal of the American Chemical Society* 2014, 136, 978-985.
57. Artyushkova, K.; Serov, A.; Rojas-Carbonell, S.; Atanassov, P. Chemistry of Multitudinous Active Sites for Oxygen Reduction Reaction in Transition Metal-Nitrogen-Carbon Electrocatalysts. *The Journal of Physical Chemistry C* 2015, 119, 25917-25928.

58. Kattel, S.; Atanassov, P.; Kiefer, B. Density Functional Theory Study of Ni-Nx/C Electrocatalyst for Oxygen Reduction in Alkaline and Acidic Media. *The Journal of Physical Chemistry C* 2012, 116, 17378-17383.
59. Masa, J.; Xia, W.; Muhler, M.; Schuhmann, W. On the Role of Metals in Nitrogen-Doped Carbon Electrocatalysts for Oxygen Reduction. *Angewandte Chemie International Edition* 2015, 54, 10102-10120.
60. Koslowski, U. I.; Abs-Wurmbach, I.; Fiechter, S.; Bogdanoff, P. Nature of the catalytic centers of porphyrin-based electrocatalysts for the ORR: A correlation of kinetic current density with the site density of Fe-N-4 Centers. *J Phys Chem C* 2008, 112, 15356-15366.
61. Varnell, J. A.; Edmund, C.; Schulz, C. E.; Fister, T. T.; Haasch, R. T.; Timoshenko, J.; Frenkel, A. I.; Gewirth, A. A. Identification of carbon-encapsulated iron nanoparticles as active species in non-precious metal oxygen reduction catalysts. *Nature communications* 2016, 7.
62. Wu, Z. Y.; Xu, X. X.; Hu, B. C.; Liang, H. W.; Lin, Y.; Chen, L. F.; Yu, S. H. Iron Carbide Nanoparticles Encapsulated in Mesoporous Fe-N-Doped Carbon Nanofibers for Efficient Electrocatalysis. *Angewandte Chemie International Edition* 2015, 54, 8179-8183.
63. Tian, J.; Morozan, A.; Sougrati, M. T.; Lefevre, M.; Chenitz, R.; Dodelet, J. P.; Jones, D.; Jaouen, F. Optimized Synthesis of Fe/N/C Cathode Catalysts for PEM Fuel Cells: A Matter of Iron-Ligand Coordination Strength. *Angew Chem Int Edit* 2013, 52, 6867-6870.
64. Workman, M. J.; Serov, A.; Halevi, B.; Atanassov, P.; Artyushkova, K. Application of the Discrete Wavelet Transform to SEM and AFM Micrographs for Quantitative Analysis of Complex Surfaces. *Langmuir* 2015, 31, 4924-33.
65. Rojas-Carbonell, S.; Babanova, S.; Serov, A.; Artyushkova, K.; Workman, M.; Santoro, C.; Mirabal, A.; Calabrese Barton, S.; Atanassov, P. Integration of Platinum Group Metal-Free Catalysts with Bilirubin Oxidase into a Hybrid Material for Oxygen Reduction Reaction: Interplay of Chemistry and Morphology. *ChemSusChem* 2017.
66. Serov, A.; Workman, M. J.; Artyushkova, K.; Atanassov, P.; McCool, G.; McKinney, S.; Romero, H.; Halevi, B.; Stephenson, T. Highly stable precious metal-free cathode catalyst for fuel cell application. *J Power Sources* 2016, 327, 557-564.
67. Stariha, S.; Artyushkova, K.; Workman, M. J.; Serov, A.; McKinney, S.; Halevi, B.; Atanassov, P. PGM-free Fe-N-C catalysts for oxygen reduction reaction: Catalyst layer design. *J Power Sources* 2016, 326, 43-49.
68. Workman, M. J.; Dzara, M. J.; Ngo, C.; Pylypenko, S.; Serov, A.; McKinney, S.; Gordon, J.; Atanassov, P.; Artyushkova, K. Platinum Group Metal-Free Electrocatalysts: Effects of Synthesis on Structure and Performance in Proton-Exchange Membrane Fuel Cell Cathodes. *J Power Sources* 2017, 348, 30-39.
69. Borup, R.; Meyers, J.; Pivovar, B.; Kim, Y. S.; Mukundan, R.; Garland, N.; Myers, D.; Wilson, M.; Garzon, F.; Wood, D.; Zelenay, P.; More, K.; Stroh, K.; Zawodzinski, T.; Boncella, J.; McGrath, J. E.; Inaba, M.; Miyatake, K.; Hori, M.; Ota, K.; Ogumi, Z.; Miyata, S.; Nishikata, A.; Siroma, Z.; Uchimoto, Y.; Yasuda, K.; Kimijima, K. I.; Iwashita, N. Scientific aspects of

- polymer electrolyte fuel cell durability and degradation. *Chem Rev* 2007, 107, 3904-3951.
70. Alshibli, K. A.; Alsaleh, M. I. Characterizing surface roughness and shape of sands using digital microscopy. *Journal of Computing in Civil Engineering* 2004, 18, 36-45.
 71. Pyun, S. I.; Rhee, C. K. An investigation of fractal characteristics of mesoporous carbon electrodes with various pore structures. *Electrochim Acta* 2004, 49, 4171-4180.
 72. Ramón-Torregrosa, P. J.; Rodríguez-Valverde, M. A.; Amirfazli, A.; Cabrerizo-Vílchez, M. A. Factors affecting the measurement of roughness factor of surfaces and its implications for wetting studies. *Colloids and Surfaces A: Physicochemical and Engineering Aspects* 2008, 323, 83-93.
 73. Artyushkova, K.; Walker, C.; Patterson, W.; Atanassov, P. Hierarchically Structured Non-PGM Oxygen Reduction Electrocatalyst Based on Microemulsion-Templated Silica and Pyrolyzed Iron and Cyanamide Precursors. *Electrocatalysis-Us* 2014, 5, 241-247.
 74. Ganesan, R.; Das, T. K.; Venkataraman, V. Wavelet-based multiscale statistical process monitoring: A literature review. *IIE Transactions* 2004, 36, 787-806.
 75. Lingadurai, K.; Shunmugam, M. S. Metrological characteristics of wavelet filter used for engineering surfaces. *Measurement* 2006, 39, 575-584.
 76. Sun, W.; Mukherjee, R.; Stroeve, P.; Palazoglu, A.; Romagnoli, J. A. A multi-resolution approach for line-edge roughness detection. *Microelectronic Engineering* 2009, 86, 340-351.
 77. Palazoglu, A.; Stroeve, P.; Romagnoli, J. A. *Wavelet Analysis of Images from Scanning Probe and Electron Microscopy*. Formatex 2010; Vol. 2.
 78. S-5200 Ultra-High Resolution Field Emission SEM. Hitachi High-Technologies Corporation: Tokyo, Japan, 2001; Vol. Sheet 98.
 79. Product Data: Quanta 3D FEG. FEI Company: Hillsboro, OR, 2009; Vol. DS0009 20-2007.
 80. NIST. *Report of Investigation - Reference Material 8013 - Gold Nanoparticles, Nominal 60 nm Diameter*; NIST: Gaithersburg, MD, 2012; p 2.
 81. Daubechies, I. *Ten lectures on wavelets*. Society for Industrial and Applied Mathematics: Philadelphia, PA, 1992.
 82. Misiti, M.; Misiti, Y.; Oppenheim, G.; Poggi, J.-M. Wavelet Toolbox. In *User's Guide For Use with MATLAB* [Online] The MathWorks, Inc.: 1996; p. 626. http://www.mathworks.com/help/pdf_doc/wavelet/wavelet_uq.pdf (accessed February 12, 2013).
 83. Bartolacci, G.; Pelletier, P.; Tessier, J.; Duchesne, C.; Bosse, P. A.; Fournier, J. Application of numerical image analysis to process diagnosis and physical parameter measurement in mineral processes - Part I: Flotation control based on froth textural characteristics. *Miner Eng* 2006, 19, 734-747.
 84. Workman, M. J. *Wavelet Roughness Analysis of Images*, <http://goo.gl/iH4dRc> Mathworks File Exchange, 2014.
 85. Vierrath, S.; Güder, F.; Menzel, A.; Hagner, M.; Zengerle, R.; Zacharias, M.; Thiele, S. Enhancing the quality of the tomography of

nanoporous materials for better understanding of polymer electrolyte fuel cell materials. *J Power Sources* 2015, 285, 413-417.

86. Vierrath, S.; Zielke, L.; Moroni, R.; Mondon, A.; Wheeler, D. R.; Zengerle, R.; Thiele, S. Morphology of nanoporous carbon-binder domains in Li-ion batteries—A FIB-SEM study. *Electrochemistry Communications* 2015, 60, 176-179.

87. Komini Babu, S.; Chung, H. T.; Zelenay, P.; Litster, S. Resolving Electrode Morphology's Impact on Platinum Group Metal-Free Cathode Performance Using Nano-CT of 3D Hierarchical Pore and Ionomer Distribution. *ACS Appl. Mater. Interfaces* 2016, 8, 32764-32777.

88. Manke, I.; Markoetter, H.; Arlt, T.; Toetzke, C.; Klages, M.; Haussmann, J.; Enz, S.; Wieder, F.; Scholta, J.; Kardjilov, N.; Hilger, A.; Banhart, J. Fuel Cell Research with Neutron Imaging at Helmholtz Centre Berlin. *Phys. Procedia* 2015, 69, 619-627.

89. Perfect, E.; Cheng, C. L.; Kang, M.; Bilheux, H. Z.; Lamanna, J. M.; Gragg, M. J.; Wright, D. M. Neutron imaging of hydrogen-rich fluids in geomaterials and engineered porous media: A review. *Earth-Sci. Rev.* 2014, 129, 120-135.

90. Thiele, S.; Zengerle, R.; Ziegler, C. Nano-morphology of a polymer electrolyte fuel cell catalyst layer-imaging, reconstruction and analysis. *Nano Res.* 2011, 4, 849-860.

91. Ziegler, C.; Thiele, S.; Zengerle, R. Direct three-dimensional reconstruction of a nanoporous catalyst layer for a polymer electrolyte fuel cell. *J. Power Sources* 2011, 196, 2094-2097.

92. Satoh, H.; Owari, M.; Nihei, Y. Three-dimensional analysis of a microstructure by submicron secondary ion mass spectrometry. *J. Vac. Sci. Technol., B* 1991, 9, 2638-41.

93. Kubis, A. J.; Shiflet, G. J.; Hull, R.; Dunn, D. N. Focused ion-beam tomography. *Metallurgical and Materials Transactions A* 2004, 35, 1935-1943.

94. Utke, I.; Moshkalev, S.; Russell, P. Review of FIB Tomography. In *Nanofabrication Using Focused Ion and Electron Beams: Principles and Applications*, Holzer, L.; Cantoni, M., Eds. Oxford University Press: 2012.

95. Artyushkova, K.; Serov, A.; Rojas-Carbonell, S.; Atanassov, P. Chemistry of Multitudinous Active Sites for Oxygen Reduction Reaction in Transition Metal-Nitrogen-Carbon Electrocatalysts. *J Phys Chem C* 2015, 119, 25917-25928.

96. Lee, H.; Lim, T. H.; Kim, D. H. Complementary effect of plasma-catalysis hybrid system on methane complete oxidation over non-PGM catalysts. *Catal Commun* 2015, 69, 223-227.

97. Wang, X.; Zhang, H.; Lin, H.; Gupta, S.; Wang, C.; Tao, Z.; Fu, H.; Wang, T.; Zheng, J.; Wu, G.; Li, X. Directly converting Fe-doped metal-organic frameworks into highly active and stable Fe-N-C catalysts for oxygen reduction in acid. *Nano Energy* 2016, 25, 110-119.

98. Zhang, Z. Y.; Xin, L.; Li, W. Z. Electrocatalytic oxidation of glycerol on Pt/C in anion-exchange membrane fuel cell: Cogeneration of electricity and valuable chemicals. *Appl Catal B-Environ* 2012, 119, 40-48.

99. Tylus, U.; Jia, Q.; Hafiz, H.; Allen, R. J.; Barbiellini, B.; Bansil, A.; Mukerjee, S. Engendering anion immunity in oxygen consuming cathodes based on Fe-N-x electrocatalysts: Spectroscopic and electrochemical advanced characterizations. *Appl Catal B-Environ* 2016, 198, 318-324.
100. Barkholtz, H. M.; Chong, L.; Kaiser, Z. B.; Xu, T.; Liu, D.-J. Enhanced performance of non-PGM catalysts in air operated PEM-fuel cells. *Int J Hydrogen Energy* 2016.
101. Barkholtz, H. M.; Chong, L. N.; Kaiser, Z. B.; Xu, T.; Liu, D. J. Highly Active Non-PGM Catalysts Prepared from Metal Organic Frameworks. *Catalysts* 2015, 5, 955-965.
102. Zhao, D.; Shui, J. L.; Chen, C.; Chen, X. Q.; Reprogle, B. M.; Wang, D. P.; Liu, D. J. Iron imidazolate framework as precursor for electrocatalysts in polymer electrolyte membrane fuel cells. *Chem Sci* 2012, 3, 3200-3205.
103. Holby, E. F.; Zelenay, P. Linking structure to function: The search for active sites in non-platinum group metal oxygen reduction reaction catalysts. *Nano Energy* 2016.
104. Serov, A.; Artyushkova, K.; Niangar, E.; Wang, C. M.; Dale, N.; Jaouen, F.; Sougrati, M. T.; Jia, Q. Y.; Mukerjee, S.; Atanassov, P. Nano-structured non-platinum catalysts for automotive fuel cell application. *Nano Energy* 2015, 16, 293-300.
105. Yuan, S.; Goenaga, G.; Grabstanowicz, L.; Shui, J.; Chen, C.; Commet, S.; Reprogle, B.; Liu, D. J. New Approach to High-Efficiency Non-PGM Catalysts Using Rationally Designed Porous Organic Polymers. *Ecs Transactions* 2013, 58, 1671-1680.
106. Goenaga, G.; Ma, S. Q.; Yuan, S. W.; Liu, D. J. New Approaches to Non-Pgm Electrocatalysts Using Porous Framework Materials. *Ecs Transactions* 2010, 33, 579-586.
107. Stariha, S.; Artyushkova, K.; Serov, A.; Atanassov, P. Non-PGM membrane electrode assemblies: Optimization for performance. *Int J Hydrogen Energy* 2015, 40, 14676-14682.
108. Robson, M. H.; Artyushkova, K.; Patterson, W.; Atanassov, P.; Hibbs, M. R. Non-platinum Carbon-Supported Oxygen Reduction Catalyst Ink Evaluation Based on Poly(sulfone) and Poly(phenylene)-Derived Ionomers in Alkaline Media. *Electrocatalysis-Us* 2014, 5, 148-158.
109. Barkholtz, H. M.; Chong, L.; Kaiser, Z. B.; Liu, D. J. Non-Precious Metal Catalysts Prepared By Zeolitic Imidazolate Frameworks: The Ligand Influence to Morphology and Performance. *Fuel Cells* 2016, 16, 428-433.
110. Kramm, U. I.; Herrmann-Geppert, I.; Behrends, J.; Lips, K.; Fiechter, S.; Bogdanoff, P. On an Easy Way To Prepare Metal-Nitrogen Doped Carbon with Exclusive Presence of MeN₄-type Sites Active for the ORR. *Journal of the American Chemical Society* 2016, 138, 635-640.
111. Kramm, U. I.; Zana, A.; Vosch, T.; Fiechter, S.; Arenz, M.; Schmeißer, D. On the structural composition and stability of Fe-N-C catalysts prepared by an intermediate acid leaching. *Journal of Solid State Electrochemistry* 2016, 20, 969-981.
112. Tian, J.; Morozan, A.; Sougrati, M. T.; Lefèvre, M.; Chenitz, R.; Dodelet, J.-P.; Jones, D.; Jaouen, F. Optimized Synthesis of Fe/N/C Cathode

- Catalysts for PEM Fuel Cells: A Matter of Iron–Ligand Coordination Strength. *Angewandte Chemie* 2013, 125, 7005-7008.
113. Zhuang, S. Q.; Shi, X.; Lee, E. S. A Review on Non-Pgm Cathode Catalysts for Polymer Electrolyte Membrane (Pem) Fuel Cell. *Proceedings of the Asme 13th Fuel Cell Science, Engineering, and Technology Conference*, 2015 2016.
 114. Jia, Q.; Ramaswamy, N.; Tylus, U.; Strickland, K.; Li, J.; Serov, A.; Artyushkova, K.; Atanassov, P.; Anibal, J.; Gumeci, C.; Barton, S. C.; Sougrati, M.-T.; Jaouen, F.; Halevi, B.; Mukerjee, S. Spectroscopic insights into the nature of active sites in iron–nitrogen–carbon electrocatalysts for oxygen reduction in acid. *Nano Energy* 2016.
 115. Li, J. K.; Ghoshal, S.; Liang, W. T.; Sougrati, M. T.; Jaouen, F.; Halevi, B.; McKinney, S.; McCool, G.; Ma, C. R.; Yuan, X. X.; Ma, Z. F.; Mukerjee, S.; Jia, Q. Y. Structural and mechanistic basis for the high activity of Fe-N-C catalysts toward oxygen reduction. *Energ Environ Sci* 2016, 9, 2418-2432.
 116. Kothandaraman, R.; Nallathambi, V.; Artyushkova, K.; Barton, S. C. Non-precious oxygen reduction catalysts prepared by high-pressure pyrolysis for low-temperature fuel cells. *Applied Catalysis B: Environmental* 2009, 92, 209-216.
 117. Nabae, Y.; Nagata, S.; Hayakawa, T.; Niwa, H.; Harada, Y.; Oshima, M.; Isoda, A.; Matsunaga, A.; Tanaka, K.; Aoki, T. Pt-free carbon-based fuel cell catalyst prepared from spherical polyimide for enhanced oxygen diffusion. *Scientific Reports* 2016, 6, 23276.
 118. Shao, M. H.; Chang, Q. W.; Dodelet, J. P.; Chenitz, R. Recent Advances in Electrocatalysts for Oxygen Reduction Reaction. *Chem Rev* 2016, 116, 3594-3657.
 119. Kramm, U. I.; Herrmann-Geppert, I.; Fiechter, S.; Zehl, G.; Zizak, I.; Dorbandt, I.; Schmei; Bogdanoff, P. Effect of iron-carbide formation on the number of active sites in Fe-N-C catalysts for the oxygen reduction reaction in acidic media. *Journal of Materials Chemistry A* 2014, 2, 2663-2670.
 120. Wu, Z.-Y.; Xu, X.-X.; Hu, B.-C.; Liang, H.-W.; Lin, Y.; Chen, L.-F.; Yu, S.-H. Iron Carbide Nanoparticles Encapsulated in Mesoporous Fe-N-Doped Carbon Nanofibers for Efficient Electrocatalysis. *Angewandte Chemie International Edition* 2015, 54, 8179-8183.
 121. Zitolo, A.; Goellner, V.; Armel, V.; Sougrati, M.-T.; Mineva, T.; Stievano, L.; Fonda, E.; Jaouen, F. Identification of catalytic sites for oxygen reduction in iron- and nitrogen-doped graphene materials. *Nat Mater* 2015, 14, 937-942.
 122. Holby, E. F.; Wu, G.; Zelenay, P.; Taylor, C. D. Structure of Fe-Nx-C Defects in Oxygen Reduction Reaction Catalysts from First-Principles Modeling. *The Journal of Physical Chemistry C* 2014, 118, 14388-14393.
 123. Kabir, S.; Artyushkova, K.; Kiefer, B.; Atanassov, P. Computational and experimental evidence for a new TM-N-3/C moiety family in non-PGM electrocatalysts. *Phys Chem Chem Phys* 2015, 17, 17785-17789.
 124. Kabir, S.; Artyushkova, K.; Serov, A.; Kiefer, B.; Atanassov, P. Binding energy shifts for nitrogen-containing graphene-based electrocatalysts – experiments and DFT calculations. *Surface and Interface Analysis* 2016, 48, 293-300.

125. Matanovic, I.; Artyushkova, K.; Strand, M. B.; Dzara, M. J.; Pylypenko, S.; Atanassov, P. Core Level Shifts of Hydrogenated Pyridinic and Pyrrolic Nitrogen in the Nitrogen Containing Graphene Based Electrocatalysts: In-Plane vs Edge Defects. *The Journal of Physical Chemistry C* 2016.
126. Artyushkova, K.; Matanovic, I.; Halevi, B.; Atanassov, P. Oxygen binding to active sites of Fe-N-C ORR electrocatalysts observed by Ambient-Pressure XPS. *J Phys Chem C* submitted.
127. Serov, A.; Artyushkova, K.; Andersen, N. I.; Stariha, S.; Atanassov, P. Original mechanochemical synthesis of non-platinum group metals oxygen reduction reaction catalysts assisted by sacrificial support method. *Electrochimica Acta* 2015, 179, 154-160.
128. Higgins, D. C.; Chen, Z. Recent progress in non-precious metal catalysts for PEM fuel cell applications. *The Canadian Journal of Chemical Engineering* 2013, 91, 1881-1895.
129. Anibal, J.; Romero, H. G.; Leonard, N. D.; Gumeci, C.; Halevi, B.; Calabrese Barton, S. Effect of silica morphology on the structure of hard-templated, non-precious metal catalysts for oxygen reduction. *Applied Catalysis B: Environmental* 2016, 198, 32-37.
130. Dombrovskis, J. K.; Palmqvist, A. E. C. Recent Progress in Synthesis, Characterization and Evaluation of Non-Precious Metal Catalysts for the Oxygen Reduction Reaction. *Fuel Cells* 2016, 16, 4-22.
131. Wiggins-Camacho, J. D.; Stevenson, K. J. Mechanistic Discussion of the Oxygen Reduction Reaction at Nitrogen-Doped Carbon Nanotubes. *J Phys Chem C* 2011, 115, 20002-20010.
132. Barrett, E. P.; Joyner, L. G.; Halenda, P. P. The Determination of Pore Volume and Area Distributions in Porous Substances. 1. Computations from Nitrogen Isotherms. *Journal of the American Chemical Society* 1951, 73, 373-380.
133. Ustinov, E. A. Nitrogen adsorption on silica surfaces of nonporous and mesoporous materials. *Langmuir* 2008, 24, 6668-6675.
134. Tsui, L.-k. *CarbonXS GUI - GUI Front-end to CarbonXS*, 1.0.1; github.com/lktsui/carbon_xs_gui Albuquerque, NM, 2016.
135. Artyushkova, K.; Cornejo, J. A.; Ista, L. K.; Babanova, S.; Santoro, C.; Atanassov, P.; Schuler, A. J. Relationship between surface chemistry, biofilm structure, and electron transfer in *Shewanella* anodes. *Biointerphases* 2015, 10, 019013.
136. Gor, G. Y.; Thommes, M.; Cychosz, K. A.; Neimark, A. V. Quenched solid density functional theory method for characterization of mesoporous carbons by nitrogen adsorption. *Carbon* 2012, 50, 1583-1590.
137. Neimark, A. V.; Lin, Y. Z.; Ravikovitch, P. I.; Thommes, M. Quenched solid density functional theory and pore size analysis of micro-mesoporous carbons. *Carbon* 2009, 47, 1617-1628.
138. Shi, H. Disorderd Carbons and Battery Applications. Dissertation, Simon Fraser University, 1993.